

Development and applications of high-performance small-animal SPECT

Ivashchenko, Oleksandra

DOI

[10.4233/uuid:3fb5d84e-39ee-43e8-87c6-21871900dabb](https://doi.org/10.4233/uuid:3fb5d84e-39ee-43e8-87c6-21871900dabb)

Publication date

2017

Document Version

Final published version

Citation (APA)

Ivashchenko, O. (2017). *Development and applications of high-performance small-animal SPECT*. [Dissertation (TU Delft), Delft University of Technology]. <https://doi.org/10.4233/uuid:3fb5d84e-39ee-43e8-87c6-21871900dabb>

Important note

To cite this publication, please use the final published version (if applicable). Please check the document version above.

Copyright

Other than for strictly personal use, it is not permitted to download, forward or distribute the text or part of it, without the consent of the author(s) and/or copyright holder(s), unless the work is under an open content license such as Creative Commons.

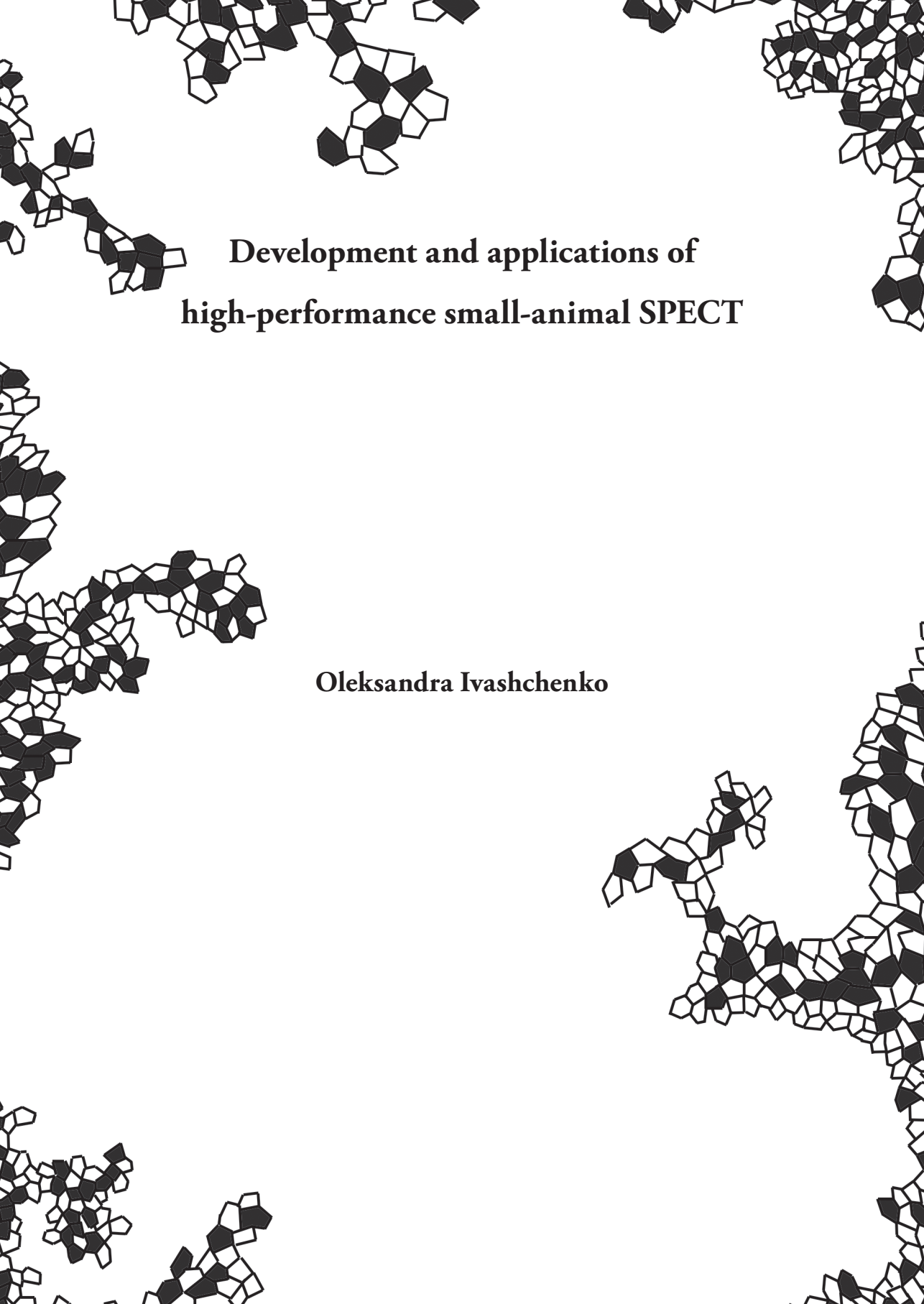
Takedown policy

Please contact us and provide details if you believe this document breaches copyrights. We will remove access to the work immediately and investigate your claim.



Development and
applications of
high-performance
small-animal
SPECT

Oleksandra Ivashchenko

A decorative border composed of irregular, overlapping black and white geometric shapes, primarily pentagons and hexagons, arranged in a complex, non-repeating pattern around the edges of the page.

**Development and applications of
high-performance small-animal SPECT**

Oleksandra Ivashchenko

Dedication

To my biggest supporters in this world: my mother and my sister.

Acknowledgments

This thesis would not have been possible without endless support, patience and understanding of my family, my colleagues and, mostly, my promotor.

My sincerest thanks to all of you.

Development and applications of high-performance small-animal SPECT

Proefschrift

ter verkrijging van de graad van doctor
aan de Technische Universiteit Delft,
op gezag van de Rector Magnificus prof. ir. K. Ch. A. M. Luyben;
voorzitter van het College voor Promoties,
in het openbaar te verdedigen op
dinsdag 24 januari 2017 om 12:30 uur

door

Oleksandra IVASHCHENKO

Master of Science in Radiophysics and Electronics,
Taras Shevchenko National University of Kyiv.

Geboren te Zolotonosha, Oekraïense SSR.

This dissertation has been approved by the promotor: Prof. dr. F. J. Beekman

Composition of the doctoral committee:

Rector Magnificus	chairman
Prof. dr. F. J. Beekman	Technische Universiteit Delft

Independent members:

Prof. dr. M. Defrise	Vrije Universiteit Brussel, België
Prof. dr. ir. M. de Jong	Erasmus Universiteit Rotterdam
Prof. dr. R. Boellaard	Rijksuniversiteit Groningen
Prof. dr. ir. L. J. van Vliet	Technische Universiteit Delft
Prof. dr. H. T. Wolterbeek	Technische Universiteit Delft, reserve member

Other member:

Dr. ir. M. C. Goorden	Technische Universiteit Delft
-----------------------	-------------------------------

Keywords: SPECT, molecular imaging, preclinical imaging



The research leading to this thesis has received funding from the People Programme (Marie Curie Actions) of the European Union's Seventh Framework Programme (FP7/2007-2013) under REA grant agreement no. PITN-GA-2012-317019 'TRACE 'n TREAT.



ISBN 978-94-92516-35-0

Copyright © 2017 by Oleksandra Ivashchenko

Printing: Ridderprint BV

Cover design: Oleksandra Ivashchenko

An electronic version of this dissertation is available at <http://repository.tudelft.nl/>

CONTENTS

Chapter 1	7
General introduction	
Chapter 2	17
Quarter-millimeter-resolution molecular mouse imaging with U-SPECT ⁺	
Chapter 3	31
High-resolution ¹³¹ Iodine SPECT imaging in mice	
Chapter 4	45
Ultra-high-sensitivity sub-mm mouse SPECT	
Chapter 5	59
SPECT/CT imaging of Pluronic nanocarriers with varying PEO block length and aggregation state	
Chapter 6	85
Effect of polymer micelle morphology on <i>in vivo</i> biodistribution probed by high-sensitivity SPECT	
Chapter 7	109
Summary & Discussion	
Chapter 8	117
Samenvatting & Discussie	
References	125
Publications list	135
Curriculum vitae	137

Chapter 1

General introduction



Introduction

In vivo imaging is one of the primary tools used for noninvasive assessment of structure and function in living subjects. In modern medical imaging modalities, electromagnetic radiation, including radiowaves (magnetic resonance imaging (MRI)), visible and near-infrared light (optical imaging (OI)), X-rays (X-ray computed tomography (CT)), γ -rays (single photon emission computed tomography (SPECT)), annihilation photons (positron emission tomography (PET)), and ultrasound are all successfully employed to interrogate the structure and/or function of tissues over time [Weissleder *et al.* 2010].

In some modalities, image contrast is intrinsic to physical properties of the object that is being imaged, like in the case of electron density for CT or spin density for MRI. Other imaging modalities always require use of additional agents that target specific cells (e.g., “tracers”) to enhance the imaging signal. Depending on the modality, those contrast agents can be, e.g., radiolabeled probes (PET, SPECT) or fluorescent molecules (OI). By exploiting different types of radiation and using different tracers [Ziessman *et al.* 2014], an enormous variety of parameters can be imaged *in vivo* [Weissleder *et al.* 2010, Cherry *et al.* 2012].

The main reason why so many different imaging modalities exist is that each of them measures fundamentally different information. Anatomical modalities (e.g., CT and MRI) mainly reveal the structure of the tissues and organs, while functional modalities, like SPECT, PET, and optical imaging, mainly visualize functions of the tissue (Figure 1). Looking beyond these characteristics, it is also true that each imaging modality operates within a different parameter space, characterized by factors such as spatial and temporal resolution, detection sensitivity, tissue penetration of the signal, signal-to-noise ratio, and the ability to visualize and quantify certain tracers or contrast agents. Because none of the existing imaging modalities can provide information on all aspects of structure and function, an obvious approach is to either alter one imaging modality to the task (e.g., special imaging sequences in MRI, adapting SPECT to image PET tracers [Goorden *et al.* 2013]) or to image a subject using multiple imaging modalities that were integrated together (e.g., “multi-modal” systems) [Cherry *et al.* 2006, Cherry *et al.* 2012].

In recent years, combining SPECT and CT, into one completely integrated device (SPECT/CT) became a standard practice in medical imaging for both clinical and preclinical applications (Figure 2). In this way, the structural information of CT complements the functional information from SPECT, for example, by enabling localization specific processes shown by

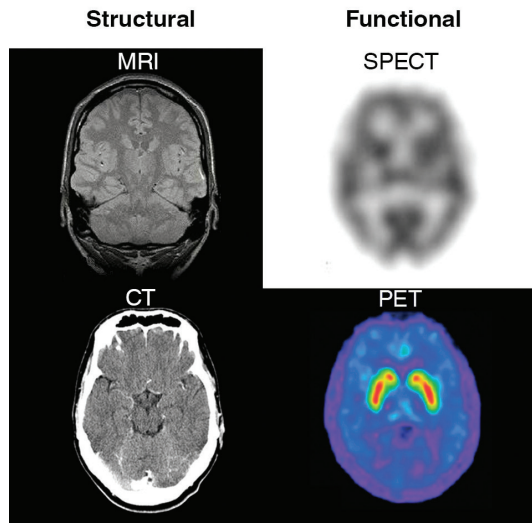


Figure 1. Examples of a brain image obtained with different structural and functional tomographic imaging modalities.

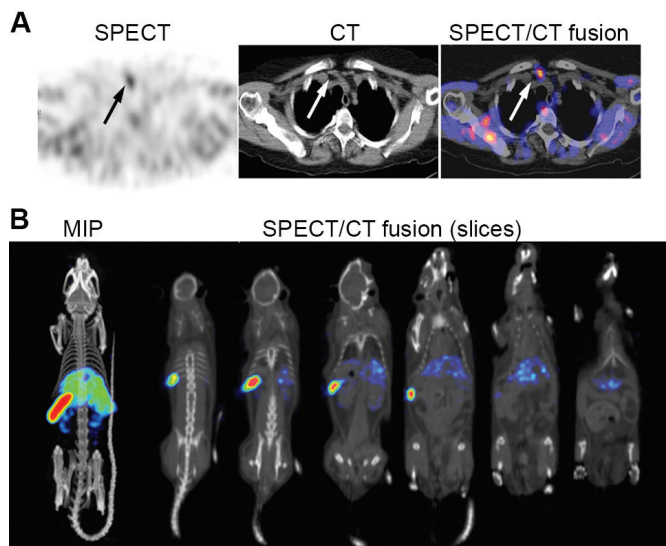


Figure 2. (A) Clinical application of SPECT/CT imaging. From left to right: transverse section through ^{99m}Tc -MIBI SPECT image showing mildly intense focal lesion in right lower neck region (arrow). Corresponding CT section (middle) and fused image (right) indicating parathyroid adenoma below right thyroid gland (arrows) [adapted from Buck *et al.* 2008]. (B) Preclinical application of SPECT/CT imaging. Fused SPECT/CT slices through an entire mouse, showing the detailed biodistribution of ^{111}In -labeled micelles [adapted from Jennings *et al.* 2016].

SPECT in the anatomical framework provided by CT, or by correlating structural change and change of tissue function. In this thesis, we will focus on task-oriented developments and applications of preclinical SPECT on a SPECT/PET/CT platform.

Radioisotope imaging

Imaging principle of emission tomography

Tomography of radioisotope distributions is mainly performed with two emission tomography modalities: SPECT and PET. With both techniques, images of the biodistribution of radionuclide-labelled agents in the body are obtained (Figure 1). These agents, known as radiopharmaceuticals (“tracers”), are designed to determine specific functions and pathologies of tissues and organs in the body [Kowalsky *et al.* 2011]. A major difference between SPECT and PET lies in the nature of the radioactive decay of their tracers: a SPECT tracer decays by emitting single gamma photons, while decay of a PET tracer results in the emission of pairs of annihilation photons. As a result, different detection principles are conventionally used for imaging SPECT and PET tracers, which has led to the use of separate SPECT and PET scanners. From this point, we will focus on the basics of SPECT imaging.

Unlike X-ray imaging, where both the emission and detection position of X-rays is known, in SPECT, only the γ -ray detection position is determined for a radioisotope source within the body. To produce an image it is, hence, necessary to provide some form of collimation, which provides information on the origin of the gamma photon. To achieve this, SPECT scanners employ mechanical collimators (i.e., lead or tungsten) that block or transmit gamma photons based on their travel direction. The majority of collimators employ holes to transmit photons in a certain direction.

The exact geometry of the collimator defines the geometrical field of view (FOV) of the SPECT system, while the hole size mainly influences spatial resolution and sensitivity of the system [Mallard *et al.* 1963, Cherry *et al.* 2012]. A wide range of collimator designs have been proposed, of which a few are shown in Figure 3. The most common type in clinical SPECT is parallel-hole collimation. In this collimator design, the size of the parallel-hole projection and the sensitivity are almost independent of object-to-collimator distance. Other types of collimators can have diverging holes (Figure 3, C), converging holes (Figure 3, D) or pinholes (Figure 3, A).

The type of collimator as well as its exact design that is used for SPECT can be optimized for the imaging task at hand, since each collimator type and parameterization has advantages and disadvantages with respect to, for example, resolution, sensitivity, size of field-of-view and required orbit of the gamma-camera.

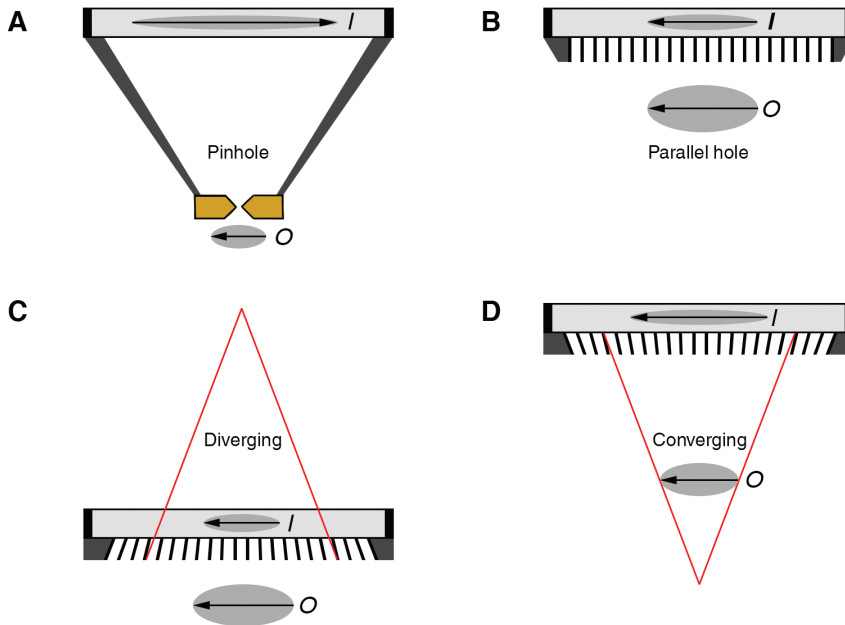


Figure 3. A-D Four main types of collimators used to project “ γ -ray images” onto the detector of a gamma camera. O – radioactive object; I- projection of the object on detector surface.

Preclinical SPECT: stepping from human to mouse scale

SPECT was originally developed for clinical use, and the subsequent preclinical adaptation of the imaging modality allowed for longitudinal molecular imaging of small laboratory animals [Kupinski *et al.* 2005]. Due to the small size of the imaged animals (a mouse is ~ 3000 times smaller in weight than a human) and high speed of their metabolism (the energy expenditure per gram of body weight of a mouse is ~ 10 times higher than in a human) [Kummitha *et al.* 2014], it is essential to have a high spatial resolution and imaging speed (enabled by, e.g., high detection efficiency/sensitivity).

Looking at spatial resolution first, if we want to see the same level of details relative to, e.g., the size of the organs in a mouse as we can see in a human, the spatial resolution, compared to clinical SPECT (~ 1 cm), needs to be improved by at least a factor of $(3000)^{1/3} \approx 15$. Such an obstacle forced scientists to look for a new imaging approach for preclinical SPECT. The solution was found in full exploration of pinhole imaging with a high magnification principle (Figure 4).

A pinhole collimator consists of a piece of dense material containing only a small hole, which typically has the shape of a double cone. By placing the object close to the aperture of the pinhole, one can reach a high magnification of its projection on the detector surface (Figure 3A, Figure 4) and effectively minimize the influence of limited intrinsic resolution of the detector. As a result, the spatial resolution and detection efficiency of a pinhole collimator [Anger *et al.* 1958, Mallard *et al.* 1963, Copeland *et al.* 1949, Cherry *et al.* 2012] are mainly determined by the pinhole diameter, object-to-collimator, and collimator-to-detector distance. This improves resolution/sensitivity trade-off of SPECT systems and makes it very well suited for imaging of small objects/animals.

First attempts to obtain SPECT images of rodents with a high resolution were based on the use of pinhole collimators attached to rotating standard clinical gamma cameras [Strand *et al.* 1993, Weber *et al.* 1994, Jaszczak *et al.* 1994]. In this way, use of a single pinhole aperture and optimal detector-aperture geometry (e.g., high magnification) can provide high spatial resolution (up to 200 μm resolution [Beekman *et al.* 2002]) and good image quality for long acquisition. However, this approach suffers from low detection efficiency and, therefore, requires a long imaging time or use of high tracer activities. This introduces a second important requirement for the performance of a small-animal SPECT scanner: the need for a high detection efficiency/sensitivity.

Probably the most obvious way to improve the sensitivity of pinhole SPECT is based on minimization of animal-to-pinhole distance. However, placing the animal close to the pinhole aperture comes at the cost of reducing the size of the area that can be imaged at a given time (the “field-of-view” (FOV)) compared to imaging at a lower magnification. Nevertheless, when combined with moving the animal (the so-called “scanning-focus method” [Vastenhouw *et al.* 2007]) through the FOV over an optimized trajectory [Vaissier *et al.* 2012], a larger area of interest can be imaged with a good time resolution and sensitivity.

To increase the sensitivity even more, multiple pinholes that simultaneously capture projections from multiple angles can be used. In such a design, separate projections can be either captured by different gamma cameras or be simultaneously projected on one detector surface. When multiple pinhole projections are projected on a single detector surface, they can either overlap each other (multiplexing projections) [Schramm *et al.* 2003] or be fully separated (non-overlapping projections) [Jaszczak *et al.* 1994, Beekman *et al.* 2005]. Although pinhole collimators with multiplexing projections allow reaching a higher sensitivity (when compared to non-overlap-

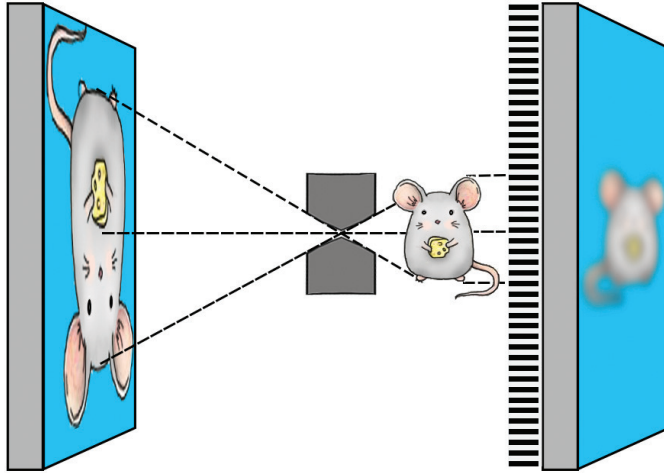


Figure 4. Illustration of pinhole (left) and parallel-hole collimation (right) imaging principles.

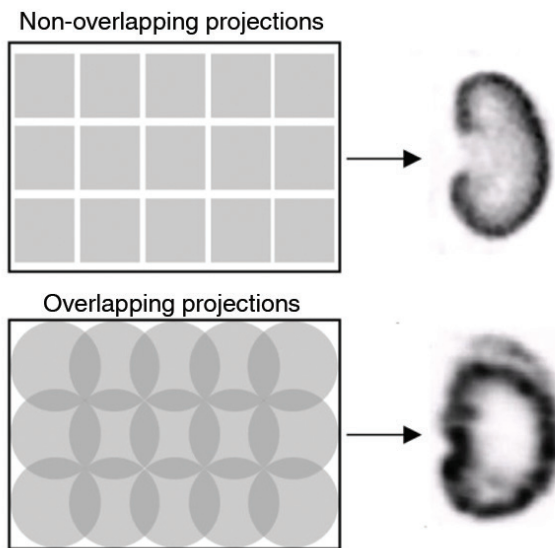


Figure 5. Schematic illustration of non-overlapping (top left) and overlapping (bottom left) pinhole projections on the detector surface and corresponding influence on image quality of SPECT scans (right).

-ping designs), they can also suffer from multiple artifacts in reconstructed SPECT images (Figure 5). The artifacts are caused by ambiguity about the origin of γ -photons detected in the areas of the overlap [van Audenhaege *et al.* 2015, Vunckx *et al.* 2008, Mok *et al.* 2009, Mok *et al.* 2011].

Taking these considerations into an account, many pinhole SPECT system designs can be suggested, including a rotating gamma camera, a stationary detector but a rotating collimator, or a completely stationary camera in which a large number of pinholes surround the animal [Madsen *et al.* 2007, Furenlid *et al.* 2004, Beekman *et al.* 2005]. However, stationary systems have several advantages over non-stationary systems [Rowe *et al.* 1993]. First, due to the stable position of the detector(s) and the collimator they do not require the repetitive system geometry recalibration that is needed for rotating designs. Second, because all required angular information is acquired simultaneously by multiple pinholes, they are very well suited for dynamic SPECT imaging.

Based on a stationary detector setup with three clinical gamma Anger-type cameras, dedicated preclinical SPECT scanners, U-SPECT-I [Beekman *et al.* 2005] and U-SPECT-II [van der Have *et al.* 2009], were developed at the University Medical Center Utrecht, and later on dramatically improved in a collaboration between Molecular Imaging Laboratories (MILabs B.V.) and Delft University of Technology. Using a set of exchangeable focusing multi-pinhole collimators, today U-SPECT systems can perform high-resolution (down to 0.25 mm) or fast dynamic (up to 8 s time-frames) [Vaissier *et al.* 2012] SPECT imaging of rodents. In one of the latest developments of the system, a novel collimation technique were developed [Goorden *et al.* 2013] that allows for simultaneous pinhole-collimated imaging of 511 keV annihilation (PET) and single gamma photons (SPECT). The resulting dual-modality SPECT/PET system is known as a Versatile Emission Computed Tomography (VECTor) scanner and is often equipped with a fully integrated CT scanner.

Image reconstruction in emission tomography

A SPECT measurement consists of 2-dimensional projections of the radioactive source distribution that are obtained with collimator(s) and gamma-detector(s). It is the goal of an image reconstruction algorithm to accurately reconstruct the unknown 3-dimensional distribution of the radioactivity from the 2-dimensional projections [Qi *et al.* 2006].

Because SPECT projections are usually noisy and collimator resolution and sensitivity strongly vary with source-to-pinhole distance, the preferred tomographic reconstruction methods are iterative algorithms and not analytic methods. The Maximum Likelihood Expectation

Maximization algorithm (MLEM) [Lange *et al.* 1984, Shepp *et al.* 1982] is an important “gold standard” in iterative image reconstruction of SPECT images, but it is also a computationally costly method. A popular solution of this obstacle is based on the use of so-called block-iterative reconstruction methods.

With block-iterative methods, every iteration of the algorithm is subdivided into many subsequent sub-iterations, each using a different subset of the projection data. An example of a widely used block-iterative version of MLEM is the Ordered Subsets Expectation Maximization algorithm (OSEM) [Hudson *et al.* 1994]. The reconstruction speedup of a full iteration OSEM over a single iteration MLEM is approximately equal to the number of subsets.

Quantification

SPECT is a quantitative imaging modality. The uptake of SPECT tracers in organs of interest can be calculated from reconstructed images. The small size of laboratory animals diminishes the photon’s attenuation in the body of the animal (compared to that in human-sized objects). Nevertheless, depending on the energy of γ -photons and the size of the animal that is used for imaging, correction for photon attenuation and scattering might be required to provide good quantification accuracy [Wu *et al.* 2010, Finucane *et al.* 2011]. A detailed discussion about effects affecting quantification of SPECT images can be found in Hwang *et al.* 2008.

Thesis outline

This thesis focuses on improvement of spatial resolution and system sensitivity of preclinical SPECT systems, in particular that of U-SPECT. In the first two chapters (chapter 2 & 3) we will primarily focus on different developments that can improve spatial resolution of the scanner for imaging of different SPECT isotopes. In the second part of the book (chapter 4-6), we will mainly focus on improvement of system sensitivity, covering collimator design and its technical evaluation, as well as two examples of low-dose imaging applications of SPECT in nanomedicine research. The final chapter provides a short summary of the thesis.

In chapter 2 we validate improvement in the performance of the scanner (U-SPECT⁺) and introduce a new 0.25 mm pinhole SPECT collimator, specifically designed for *in vivo* imaging applications that require high level of details. The collimator was evaluated with phantoms and *in vivo* mouse bone scans.

Chapter 3 is an extension of the work of Goorden *et al.* 2013 on the development of a combined SPECT/PET/CT imager, VECTor. Since VECTor already illustrated its ability to image high-energy annihilation photons, in chapter 3 we optimize and characterize VECTor for performing *in vivo* mouse imaging of the combined γ - and β -emitter ^{131}I . To this end, we optimized the image reconstruction for imaging 364 keV photons of ^{131}I and evaluated the quantification accuracy and image quality of ^{131}I SPECT using multiple phantoms and *in vivo* scans of healthy mice.

The trade-off between resolution and sensitivity is a constant challenge in preclinical SPECT and the size of laboratory animals usually puts the main focus of SPECT development on resolution improvement. However, high-sensitivity submillimeter SPECT can enable a wide range of new imaging protocols, including screening of tracers with low labeling efficiency and imaging of low receptor densities. To this end, we developed a dedicated high-sensitivity SPECT collimator that enables sub-MBq SPECT imaging with sub-millimeter resolution. In chapter 4 we introduce and validate the performance of this collimator, and also show several examples of animal imaging applications.

The use of nanocarriers is particularly promising in oncology, where they can reach high tumor accumulation and low drug toxicity via the Enhanced Permeability and Retention effect. At the same time, due to the fast renal clearance and long blood circulation of the carriers, longitudinal imaging of their biodistribution possesses challenges to the sensitivity of a SPECT system. In chapters 5 and 6 we show two low-dose applications of SPECT in nanomedicine that were enabled by the collimator development in Chapter 4. Chapter 5 introduces a new strategy to compare the biodistribution of Pluronic nanocarriers with different poly(ethylene oxide) (PEO) length and aggregation state. In chapter 6, the influence of morphology on the *in vivo* biodistribution of polystyrene-b-poly(ethylene oxide) micelles of spherical and elongated morphologies was investigated.

Chapter 2

Quarter-millimeter-resolution molecular
mouse imaging with U-SPECT⁺

This chapter is based on the publication:

Ivashchenko O, van der Have F, Villena JL, *et al.* Quarter–millimeter-resolution molecular mouse imaging with U-SPECT⁺. *Mol Imaging*. November 2014.

Abstract

Limited spatial resolution of preclinical positron emission tomography (PET) and single-photon emission computed tomography (SPECT) has slowed down applications of molecular imaging in small animals. Here we present the latest-generation U-SPECT system (U-SPECT⁺, MILabs, Utrecht, The Netherlands) enabling radionuclide imaging of mice with quarter-millimeter resolution.

The system was equipped with the newest high-resolution collimator with 0.25 mm diameter circular pinholes. It was calibrated with ^{99m}Tc point source measurements from which the system matrix was calculated. Images were reconstructed using pixel-based ordered subset expectation maximization (OSEM). Various phantoms and mouse SPECT scans were acquired. The reconstructed spatial resolution (the smallest visible capillary diameter in a hot-rod resolution phantom) was 0.25 mm.

Knee joint images show small structures such as the femur epicondyle sulcus, as well as a clear separation between cortical and trabecular bone structures. In addition, time-activity curves of the lumbar spine illustrated that tracer dynamics in tiny tissue amounts could be measured. U-SPECT⁺ allows discrimination between molecular concentrations in adjacent volumes of as small as 0.015 mL, which is significantly better than can be imaged by any existing SPECT or PET system. This increase in the level of detail makes it more and more attractive to replace *ex vivo* methods and allows monitoring biological processes in tiny parts of organs *in vivo*.

Background

The use of animal models of human disease is essential for development of new therapies and diagnostic methods. Modern small-animal SPECT/CT systems allow to (i) visualize, quantify and localize dynamic processes down to parts of organs and tumors [Beekman *et al.* 2007, Vastenhouw *et al.* 2007, Penheiter *et al.* 2012, Branderhorst *et al.* 2014, Befera *et al.* 2014], (ii) perform those studies longitudinally, (iii) reduce labor and the number of animals that need to be sacrificed compared to post-mortem tissue distribution studies, and (iv) perform simultaneous multi-probe imaging [Melis *et al.* 2010, Goorden *et al.* 2013]. However, the small size of the animals used for the imaging with these systems (if compared with humans) poses enormous challenges to image resolution characteristics, in particular when uptake needs to be distinguished in small adjacent structures *in vivo* or at sub-organ or sub-tumor structural

level. Multi-pinhole collimators, by exploiting a high magnification factor, have already shown that they enable imaging at approx. 0.35 mm resolution [Schramm *et al.* 2003, Beekman *et al.* 2005, Nuyts *et al.* 2009, van der Have *et al.* 2009]. At the same time, many applications of molecular imaging (e.g., cancer, brain and orthopedic research) still can significantly benefit from the higher level of detailization in preclinical SPECT.

Continued research in molecular imaging, including the need to quantify processes in small parts of organs and tumors, requires development of innovative scanners. Recently, MILabs launched the U-SPECT⁺/CT system as the successor of U-SPECT-II/CT [van der Have *et al.* 2009]. It is equipped with a set of multi-pinhole mouse collimators with sensitivities ranging from approximately 350 cps/MBq (aimed at reaching sub-half-mm resolution level) up to >12500 cps/MBq (for low dose but still allowing sub-mm resolution imaging). The system is advanced over its predecessor with regard to the mechanical accuracy of the robotic stage and the collimators. In addition, new spiral bed trajectories [Vaissier *et al.* 2012] for data collection have optimized sampling and enable faster scanning when compared to step-wise multi-planar bed movement of U-SPECT-II. The system matrix for image reconstruction was improved via the use of a more robust fitting procedure of the geometry of the system, that was implemented in VECTor⁺ software (MILabs, The Netherlands) based on methods described in Goorden *et al.* 2013 and Wu *et al.* 2010. In addition, detailed attenuation correction was added based on either optical or X-ray CT images to provide absolute quantification [Wu *et al.* 2010, Wu *et al.* 2011].

The aim of the present paper is to characterize high-resolution capabilities of the U-SPECT⁺/CT system with its ultra-high-resolution pinhole collimators using phantoms and various scans of the mouse skeleton.

Materials and Methods

System design and collimator geometry

U-SPECT⁺/CT (Figure 1, A) contains three stationary large gamma-ray detectors (595x472 mm) with 3/8 inch (9.5 mm) thick NaI(Tl) crystals. The Full Width at Half Maximum (FWHM) energy resolution at the 140 keV ^{99m}Tc photopeak is 9.5%. The exchangeable cylindrical pinhole collimators are placed in the center of the system. The mouse SPECT collimators used in the present study have five rings with either 0.25 mm (ultra-high-resolution, type XUHR-M, MILabs, The Netherlands), 0.35 mm (high-resolution, type UHR-M) or 0.6 mm (general-purpose, type GP-M) diameter pinholes. There are 15 pinholes per ring and

8 degrees rotation in the pinholes' position between consecutive rings (Figure 1, B). The inner diameter of the collimator (bore size) is 44 mm and the distance from the center of the pinholes to the central axis is 24 mm. The 99% tungsten tube containing the pinholes is surrounded by an outer shielding tube that prevents projections through different pinholes from overlapping. The pinholes in the 1st, 2nd, 4th, and 5th ring are tilted such that all pinholes are focused on a common region that can be reconstructed without any bed movement. The only moving part needed for SPECT acquisition is an automated robot arm with the animal bed connected to it that shifts the animal through the scanner during data acquisition in either a spiral trajectory or in multi-planar stepwise mode. Shifting the bed during acquisition is needed only if the selected scan area is bigger than the focus region that is seen by all pinholes, in order to ensure sufficient sampling conditions according to Tuy *et al.* 1983, throughout the scan volume. The way the scan area of interest (Figure 1, C) is selected using a proprietary Graphical User Interface and three optical cameras is described in [Branderhorst *et al.* 2011]. These optical or X-ray preview images can also be used for performing post-reconstruction attenuation correction [Wu *et al.* 2010, Wu *et al.* 2011].

Image reconstruction and processing

Reconstruction of the images from list-mode projection data was performed with Pixel-based Ordered Subset Expectation Maximization [Branderhorst *et al.* 2010]. It included resolution recovery and compensation for distance-dependent pinhole sensitivity. The system matrix was generated via a hybrid method based on both ^{99m}Tc point source measurements and analytical modeling [van der Have *et al.* 2008]. All images were reconstructed on an isotropic 0.125 mm voxel grid. Scatter correction was performed with the Triple Energy Window (TEW) methods [Ogawa *et al.* 1991]. A 20% wide photopeak window and two 5% wide scatter windows on each side of the photo-peak window were applied. In the focused [Branderhorst *et al.* 2011] knee joint and lumbar spine studies (acquired within a small number of animal bed positions) 16 subsets and 32 iterations were used. Compared to focused scans, acquisition of a total body (TB) mouse scan requires a higher number of animal bed positions. When the same levels of tracer activity and acquisition times are used, TB imaging results in lower number of emissions per voxel. Thus, in order to prevent erasure of low-activity image regions during Pixel-based OSEM reconstruction as we described in [Vaissier *et al.* 2013], the number of subsets was decreased to 4 while 20 iterations were performed. Reconstructed images were filtered with a 0.15 mm FWHM Gaussian kernel followed by cross-shaped 3x3x3 median filtering.

Phantom studies

The sensitivity of the system with the 0.25 mm pinhole collimator was measured with a ^{99m}Tc point source produced in the way described in [van der Have *et al.* 2009]. The uniformity of reconstructed images was assessed with a syringe (diameter 15.9 mm, length 18 mm) filled with 18.65 MBq/mL ^{99m}Tc -pertechnetate and scanned for 90 minutes. The activity in the syringe was measured in a dose calibrator (VDC-304, Veenstra Instruments, The Netherlands). Reconstructed images were corrected for attenuation and scatter [Wu *et al.* 2010, Wu *et al.* 2011].

The reconstructed spatial resolution was determined as the minimal diameter of rods that can be visualized in a hot-rod resolution phantom with six pie-shaped sectors containing rods with equal rod sizes within each sector (0.22, 0.25, 0.3, 0.35, 0.4 and 0.5 mm). In each section the distance between the capillaries equals the capillary diameter in that section. The phantom was filled with 60 MBq ^{99m}Tc -pertechnetate (about 0.05 mL) and consequently scanned for 90, 108 and 126 minutes (in order to compensate for the decay) with collimators with 0.25, 0.35 and 0.6 mm pinholes, respectively.

Animal scans

The animal experiments were performed with three C57Bl/6 mice according to protocols approved by the Animal Ethical Committee of the UMC Utrecht and in accordance with Dutch Law on Animal experimentation. All animals were anesthetized with isoflurane. For all scans radioactive tracers were administered via injection in the tail vein, except for the lumbar spine scan, for which radiotracer was administered via a catheter in the tail vein.

Total body scan

The mouse was injected with 330 MBq of ^{99m}Tc -methylene diphosphonate (MDP). Half an hour after the injection 90 minutes SPECT scan started.

Images were reconstructed and filtered as described in the image reconstruction and processing section and the bladder of the animal was manually cropped from the volume. Maximal intensity projections (MIPs) were generated using PMOD 3.4 software (Pmod Technologies Ltd, Zurich, Switzerland).

Focused scans

The first mouse used for focused scanning [Branderhorst *et al.* 2011] was injected with 340

MBq of ^{99m}Tc -MDP. Half an hour after the injection a 90 minutes SPECT scan with pinholes focusing on the knee joint started.

The second mouse was injected with 330 MBq ^{99m}Tc -hydroxydiphosphonate (HDP). A dynamic, one-minute frames SPECT scan, with the pinholes focused on the lumbar spine area started just after the injection. Acquisition continued for 90 minutes.

After the acquisition the mice were euthanized and the knee joint and lumbar spine areas were scanned postmortem in a separate ultra-high resolution CT scanner (Quantum FX, Perkin Elmer, Waltham, USA) using a 20 μm resolution setting. After image reconstruction and filtering, MIPs were generated.

Results

Phantom studies

The sensitivity at the center of the collimator was determined to be 380 cps/MBq with a ^{99m}Tc point source. Figure 2, A shows a 6-mm thick slice from the hot-rod resolution phantom scans with ^{99m}Tc for the collimators with 0.25 mm, 0.35 mm and 0.6 mm pinholes. In terms of minimal visible rod diameters, the 0.25 mm pinhole collimator reaches 0.25 mm resolution, the highest among the collimators compared. At the same time, both the collimators with 0.35 and 0.6 mm pinholes show improvement in image resolution for U-SPECT* from 0.35 to 0.3 mm and from 0.4 to 0.4-0.35 mm, respectively, compared to U-SPECT-II.

Figure 2, B shows 3 mm thick slices of the reconstructed syringe image from which 3 mm wide line profiles were extracted. The activity concentration of ^{99m}Tc measured in the dose calibrator (“gold standard”) is indicated with an orange line on the profile plots. The difference between the average activity concentration in the syringe calculated from the reconstructed image volume [Wu *et al.* 2010] and the “gold standard” was 0.32 MBq/mL or 1.7%. Figure 2, C shows a 6 mm thick slice of the resolution phantom scan with the 0.25 mm pinhole collimator from which the line profile (Figure 2, C bottom) was extracted for the 0.25 mm rods segment (as indicated with an orange line). The average center-to-center distance for two neighboring rods was 0.52 ± 0.03 mm.

Bone imaging

Figure 3 shows side and top view MIPs of the TB mouse SPECT scan. Bone turnover takes

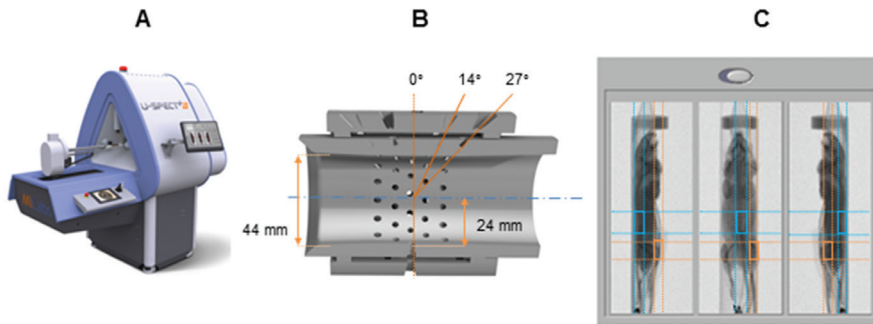


Figure 1. A- U-SPECT/CT system, B- cross-section of 75 pinhole mouse collimator with indicated inner diameter, distance from pinhole centers to the central axis and tilt angle for different pinhole rings, C - examples of X-ray based scan area selection for a knee joint (orange) and lumbar spine (blue) scans.

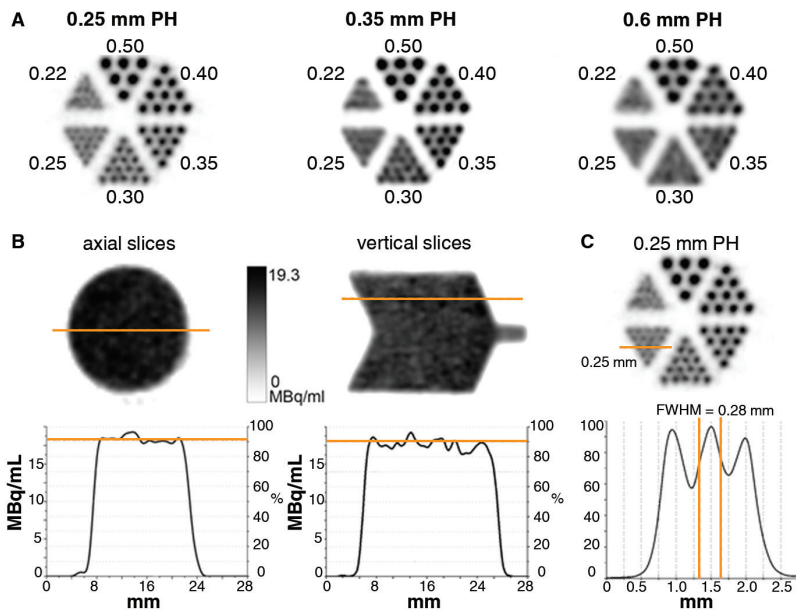


Figure 2. A - reconstructed SPECT image of hot-rod phantom for 0.25, 0.35 and 0.6 mm pinhole collimators. Minimal visible rod diameters are 0.25, 0.3 and 0.4 mm respectively. B- results of uniformly filled cylinder ^{99m}Tc phantom scan for 0.25 mm pinhole collimator. B, top - 3 mm thick axial and vertical slices. B, bottom – line profiles through the phantom, drawn as indicated on slice's images. The activity concentration measured in the dose-calibrator is indicated with orange lines on the line profile plots. C - line profile plot through the 0.25 mm rods segment (bottom) of the resolution phantom, drawn as indicated on the resolution phantom image (top).

place in the skeleton at a low (physiological) level, which leads to free calcium surface that can bind the ^{99m}Tc -MDP tracer. The images provide a great level of detail that allows to distinguish small anatomical skeletal structures. Ribs of the mouse that are usually just partially visualized in TB scans can now be fully seen, even in the false and floating ribs region. The animal's

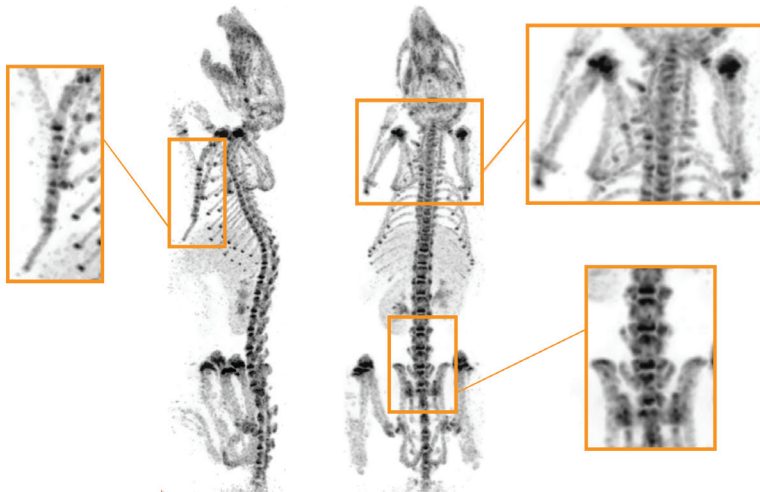


Figure 3. Side and top views on maximum intensity projections of a mouse ^{99m}Tc -MDP TB SPECT scan. Zoomed image of the pelvis show detailed structure of the ilium, pubis, and sacrum. The thoracic cage area shows tiny details such as floating ribs, clavicles and scapula blades that are usually blurry but now can be seen very clearly. Even in the sternum (zoomed left) all separate sternebrae and the manubrium and xiphisternum bones can be distinguished.

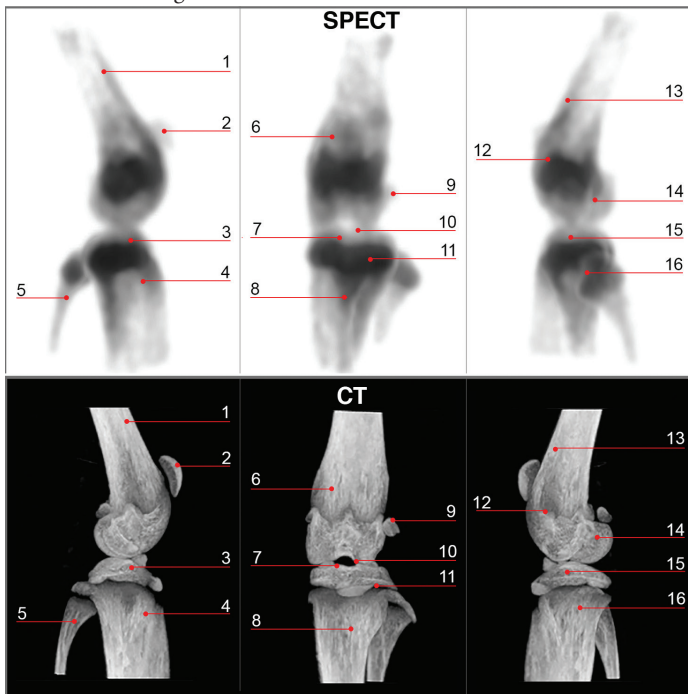


Figure 4. Maximum intensity projections of focused mouse knee joint SPECT and corresponding micro-CT scan. The images provide a high level of anatomical details, such as: 1- corpus femoris, 2- patella, 3- tibia, condylus medialis, 4- corpus tibiae, 5- corpus fibulae, 6- basis patellae, 7- linea epiphysialis, 8- tuberositas tibiae, 9- sesamoid bone, 10- tuberculum intercondylare laterale, 11- growth plate, 12- epicondylus lateralis, 13- facies poplitea, 14- fossa intercondylaris, 15- tibia, condylus lateralis, and 16- apex capituli fibulae.

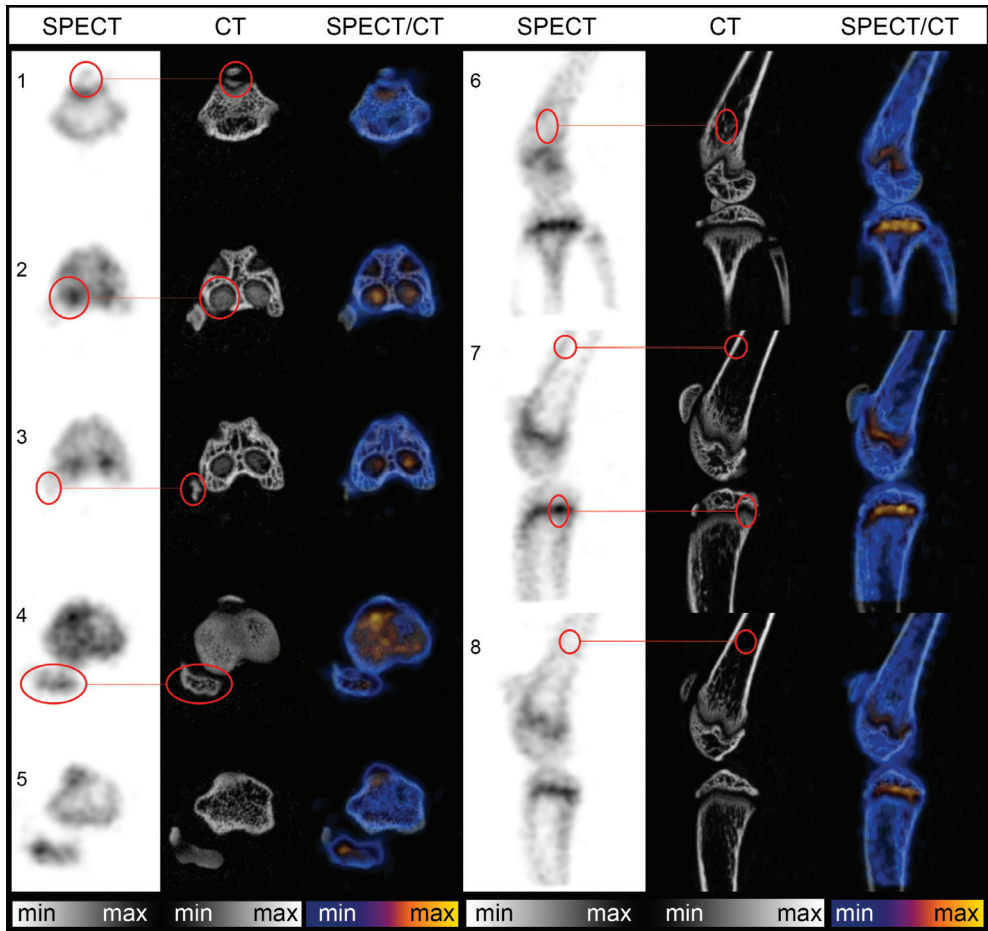


Figure 5. Axial (left) and coronal (right) slices (slice thickness 0.3 mm) of a focused mouse knee joint ^{99m}Tc -MDP SPECT, corresponding micro-CT and fused SPECT/CT scans. Arrows illustrate correlation in small anatomical details that are visible in both modalities, e.g., patella (1), distal femur condyles cuts (2), sesamoid bone (3), fibula apex (4-5), and trabecular (6), cortical (7, top) bone, growth plate (7, bottom) and medulla cavity (8) inner bone structures.

sternum (zoomed left) is fully visible with clear separation of the individual sternebra bones up to the xiphisternum ending. Scapulae and clavicles (zoomed top right) are completely shown and the blades on both scapulae can also be distinguished. In the pelvis area (zoomed in the bottom right) the ilium, pubis and sacrum show many anatomical structures. Figure 4 represents sagittal-medial (left), coronal-anterior (middle) and sagittal-lateral (right) view MIPs of SPECT (top) and micro-CT (bottom) scans. It is shown here that it is possible with SPECT to clearly visualize bone turnover in not only all the structural bones in the joint but also their substructures, such as the linea epiphysialis (7) and intercondilar tuberculum of the tibia (10), the epicondylars in the femur (12), the apex capitis fibulae (16) and the corpus fibulae (5).

Figure 5 shows axial and sagittal slices of SPECT, CT and fused SPECT/CT images through the mouse knee joint. These image modalities can be compared in terms of the visible level of details in the joint anatomy and in terms of correlations between the bone density from CT and the intensity of the signal in the SPECT images. Sagittal slices (6-8) demonstrate that a SPECT scan allows a clear anatomical distinction between the cortical bone, the trabecular bone, the growth plate and the medullary cavity. Axial slices (1-5) confirm the correspondence in shape between SPECT and CT for the patellar surface contours (1) and higher uptake regions on the condyle surface cuts just under the growth plate (2-3) of the femur, the tuberosity of the tibia and fibula apex (4-5).

A lumbar spine SPECT scan was performed focusing on the L1-L4 segments of the backbone using two bed positions. Time-activity curves (TACs) were generated for a manually-drawn volumes of interest (Figure 6, A), using decay-corrected but otherwise unprocessed images, reconstructed as a one-minute frame sequence. Quantification of the curve was done using a scaling factor obtained from the ^{99m}Tc uniformly filled cylinder scan [Wu *et al.* 2010]. Figure 6 A, B shows 0.375 mm thick slices of anatomical cross-sections for the HDP (top) and CT (bottom) scans. The axial view (Figure 6, B) at the level of the L4 vertebra shows that it is possible to visualize the uptake of a tracer in all the basic structural parts of the lumbar vertebrae, such as the spinous processes, the superior articular processes, the transverse process, and the vertebral body. The sagittal cross-sections demonstrate full separation between the vertebra bodies on SPECT images, regions with higher uptake correlate with corresponding positions of the growth plates on CT. As one can see from the TAC (Figure 6, C), there is a time shift in the position of the HDP uptake peaks for different vertebrae. Because the peak itself refers to the first passing of activity through veins, arteries and capillaries that are lying close to or inside the vertebrae, such a difference in time due to slight difference in distance from the place of injection in the tail vein to the particular lumbar spine region was expected. Also, the absolute uptake in the L1-L4 vertebrae is supposed to rise with increase of vertebra size and this can be seen on the TACs.

Discussion

In preclinical SPECT, the performance characteristics of the system strongly depend on the collimator design. In cases when an ultra-high resolution needs to be achieved, the use of focusing collimators with small pinholes gives an appropriate resolution-sensitivity trade-off,

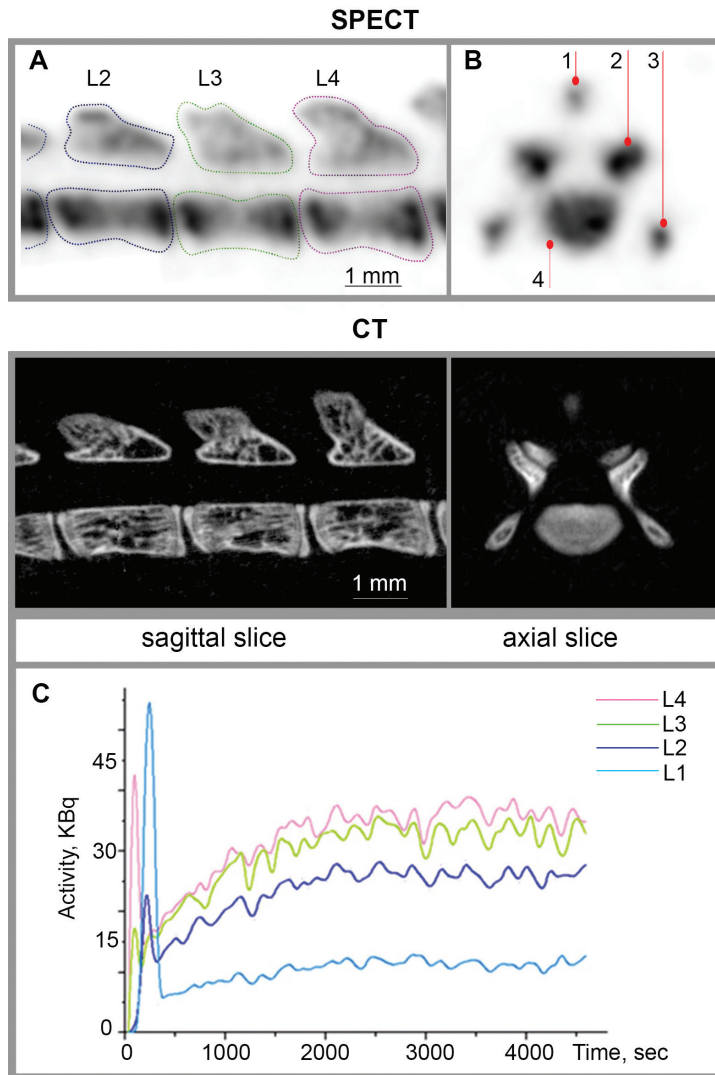


Figure 6. Images of focused L1-L4 vertebrae ^{99m}Tc -HDP SPECT (top) and micro-CT (bottom) lumbar spine scans. A, B - corresponding sagittal and axial slices (slice thickness 0.375 mm, level of L4 segment). C - time-activity curves of HDP uptake by individual vertebrae. On axial cross-sections it is possible to distinguish all the anatomical components of lumbar vertebrae, such as: 1- spinous process, 2- superior process articular, 3- transverse process, and 4- body.

particularly when large enough detectors can be used to provide high pinhole magnification. The current study evaluated the high resolution capabilities of the U-SPECT⁺ system and initial applications of its new 0.25 mm ultra-high-resolution collimator.

The resolution phantom scans that were performed demonstrated that the system provides an

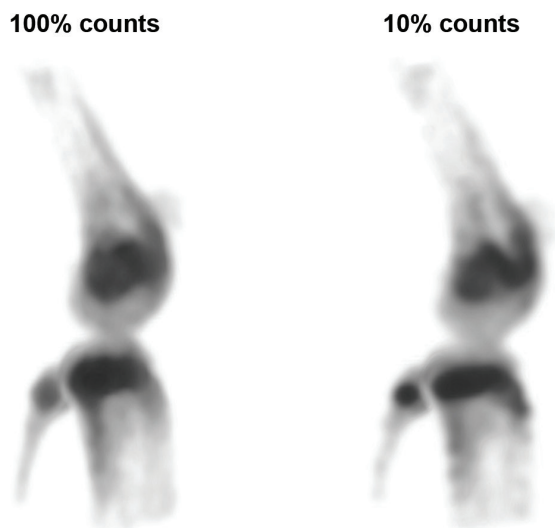


Figure 7. Maximum intensity projections of focused mouse knee joint SPECT scan. Images were reconstructed using 100% and 10% of available counts from the list-mode data and emulating the difference in image quality for 340 and 34 MBq ^{99m}Tc -MDP 90 minutes focused mouse knee joint scans, respectively.

improvement in image resolution (in terms of minimal visible rod diameter) for the already previously launched 0.35 mm high-resolution (from 0.35 to 0.3 mm) and 0.6 mm general purpose (from 0.4 to ~0.35 mm) collimators [van der Have *et al.* 2009]. With the ultra-high-resolution collimator with 0.25 mm diameter pinholes down to 0.25 mm reconstructed spatial resolution can be achieved. In combination with the scanning focus principle and a dedicated Graphical User Interface [Branderhorst *et al.* 2011] this resolution can in principle be reached in any part of the body (centrally and peripherally). Due to the relatively low sensitivity of the collimator, the average activity amount that was used for SPECT scans in this paper was 333 MBq (9 mCi). For the ^{99m}Tc -HDP tracer this results in 44 cGy total body dose [Funk *et al.* 2004, Powsner *et al.* 2006] for a 30 g mouse. This is still 20 times below the LD50/30 (approximately 9 Gy for C57BL/6) [Williams *et al.* 2010], yet already cannot be neglected.

Considering the fact that the dose-rate of SPECT scans performed is lower than 0.28 cGy/min, the influence of the exposure on the cell survival rate is still expected to be small [Amundson *et al.* 2003]. Whereas the activation of some cell cycle regulating genes will take place already from as low as 2 cGy [Amundson *et al.* 2003] in a dose-rate independent manner, gradually increasing with increase of accumulated dose. Thus, depending on the type of study, this collimator may often be more suitable for single animal scans or a final high-resolution scan in a follow-up imaging sequence, rather than for repetitive injection and scanning in longitudinal

studies. A dose that would be 10 times lower would eliminate this problem.

To emulate this and to be able to compare images one to one with exact spatiotemporal registration, we performed a reconstruction using 10% of the counts extracted from the list-mode data (Figure 7). This scan represents an equivalent of a 34 MBq scan or 4.4 cGy dose. The reconstruction presented in Figure 7 was post filtered with a slightly wider 3D Gaussian kernel of 0.35 mm and compared to the corresponding 100% count images. It can be appreciated that tenfold reduced dose results in more noise, mainly visible in the distal part of the bones with low tracer uptake (e.g., femur and tibia corpus, patella), yet still provides a very high level of detail in high specific uptake areas of the joint (e.g., femur and tibia condyles, growth plate, fibula apex). Hence, in cases where either the acquisition time can be sufficiently long or the uptake of the tracer is well localized and specific, like in the case of bone imaging with ^{99m}Tc MDP or HDP tracers, we have shown that it is possible to take advantage of very high resolution pinhole collimation.

The level of details that our results have shown in bone SPECT indicates that in some cases the need for additional anatomical imaging may be less important. Other examples where we see accurate anatomical information from SPECT only are reported in Befera *et al.* 2014 (about cardiac imaging) and in [Zhou *et al.* 2012, Branderhorst *et al.* 2014] for tumor imaging. The total body scans performed in the present paper showed that U-SPECT⁺ equipped with the new ultra-high-resolution collimator detects bone turnover in the entire skeleton in great details. When finer analysis is needed, focused imaging can be performed (Figure 4-6). The level of details visible with focused knee-joint and lumbar spine scans provides both functional information in tiny structures and a high level of anatomical detail. However, we should also take into account that resolution of *in vivo* SPECT images can be hampered by animal motion (e.g., respiration or heart beating). In case of scans of, for example, the lower limb or pelvis area, the influence of motion-related resolution degradation is expected to be small. At the same time, images of the animal skeleton and inner organs that are closer to the rib cage and cardiac scans will certainly require motion correction with, for example, the aid of respiratory and/or ECG gating to obtain optimal sub-mm image resolution [Jaszczak *et al.* 1994]. Thus, although the TB scan in this paper resulted in a high level of details in the thorax, we assume that it would have been possible to image finer anatomical structures, if respiration gating would have been performed. The extent of image improvements is subject of future investigations.

Conclusion

This paper has introduced the latest version of U-SPECT preclinical scanners. Phantom studies show that this system (U-SPECT⁺) when equipped with an ultra-high-resolution collimator with 0.25 mm diameter circular pinholes enables quantitative imaging of molecular uptake down to a quarter of a millimeter resolution (approximately 0.015 μL volumetric resolution) in mice. The possibility of performing *in vivo* molecular imaging with the level of details as illustrated in several bone scans, opens new possibilities for ultra-high-resolution SPECT studies.

Chapter 3

High-resolution ^{131}I iodine SPECT imaging in mice

This chapter is based on the publication:

van der Have F, **Ivashchenko O**, Goorden MC, *et al.* High-resolution clustered-pinhole ^{131}I iodine SPECT imaging in mice. *Nucl Med Biol.* 2016; 43(8):506-11.

Abstract

High-resolution preclinical ^{131}I SPECT can facilitate development of new radioiodine therapies for cancer. To this end, it is important to limit resolution-degrading effects of pinhole edge penetration by the high-energy γ -photons of iodine. Here we introduce, optimize and validate ^{131}I SPECT performed with a dedicated high-energy clustered multi-pinhole collimator.

A SPECT-CT system (VECTor/CT) with stationary gamma-detectors was equipped with a tungsten collimator with clustered pinholes. Images were reconstructed with pixel-based OSEM, using a dedicated ^{131}I system matrix that models the distance- and energy-dependent resolution and sensitivity of each pinhole, as well as the intrinsic detector blurring and variable depth-of-interaction in the detector. The system performance was characterized with phantoms and *in vivo* static and dynamic ^{131}I -NaI scans of mice.

Reconstructed image resolution reached 0.6 mm, while quantitative accuracy measured with a ^{131}I filled syringe reaches an accuracy of $+3.6\pm 3.5\%$ of the “gold standard” value. *In vivo* mice scans illustrated a clear shape of the thyroid and biodistribution of ^{131}I within the animal. Pharmacokinetics of ^{131}I was assessed with 15-s time-frames from the sequence of dynamic images and time-activity curves of ^{131}I -NaI.

High-resolution quantitative and fast dynamic ^{131}I SPECT in mice is possible by means of a high-energy collimator and optimized system modeling. This enables analysis of ^{131}I uptake even within small organs in mice, which can be highly valuable for development and optimization of targeted cancer therapies.

Background

Although the combined γ - and β -emitter ^{131}I is best known for its use in thyroid cancer therapy, it is also an important nuclide for other existing and new therapeutic approaches. As an example, ^{131}I has been used in treating non-Hodgkin's [Kaminski *et al.* 2000, Kaminski *et al.* 2001, Kaminski *et al.* 2005, Gopal *et al.* 2007] and Hodgkin's lymphoma [Sauer *et al.* 2009], also liver cancer [Chen *et al.* 2006, Ychou *et al.* 1993]. Alkylphosphocholine analogs labeled with ^{131}I were reported to be very promising for therapy of a broad spectrum of solid tumors [Weichert *et al.* 2014]. Furthermore, the use of sodium-iodine symporter (NIS) mediated uptake of ^{131}I , following transfection of NIS-containing vectors into non-NIS-bearing tissues, recently

showed successful results in antibody-based treatment of non-Hodgkin's Lymphoma [Cheson *et al.* 2008], gene transfer [Marsee *et al.* 2004, Mitrofanova *et al.* 2005], viral and cell-based [Penheiter *et al.* 2012, Miest *et al.* 2013] therapeutic approaches for cancer. Nevertheless, despite the standard use of direct ^{131}I SPECT imaging in the clinic (i.e. for monitoring the response to therapy and patient-specific dose calculations), low resolution and poor quantification accuracy of *in vivo* ^{131}I imaging in the preclinical field [Fan *et al.* 2014] requires *ex vivo* analyses [Weichert *et al.* 2014, Miest *et al.* 2013] or the use of imaging substitutes ($^{99\text{m}}\text{Tc}$ -pertechnetate or $^{123}\text{I}/^{124}\text{I}$ - based compounds) [Schipper *et al.* 2007] for the assessment of therapy progression. If it were available, quantitative and high-resolution SPECT imaging of ^{131}I in small-animals would benefit the development of translational radioisotope therapies.

Imaging ^{131}I in mice is rather challenging due to the relatively high energy of its gamma photons (364 keV), that consequently penetrate the collimator wall and pinhole edges. Although extensive investigations on optimal collimator design [Tenney *et al.* 1999, Smith *et al.* 1997] and system modeling [Dewaraja *et al.* 2000, Rault *et al.* 2007, van Holen *et al.* 2009] for medium- to high-energy clinical SPECT were performed, preclinical ^{131}I imaging with sub-mm resolution was not possible up to now. Recently, SPECT and PET imaging have been combined in a novel versatile emission computed tomography system (VECTor, MILabs, The Netherlands) [Goorden *et al.* 2013] that showed simultaneous sub-mm imaging of $^{99\text{m}}\text{Tc}$ and ^{18}F by means of a dedicated clustered multi-pinhole (CMP) collimator. Compared to pinholes used in conventional SPECT collimators, the pinholes in the CMP collimator have narrower opening angles (Figure 1, A), which significantly decreases the penetration of the photons through the pinhole edges. Due to VECTor's ability to deal with annihilation photons, it is interesting to investigate its ability to image the 364 keV photons from ^{131}I .

The aim of this study is to optimize and characterize VECTor for performing *in vivo* ^{131}I mouse SPECT imaging. To this end, we first optimized image reconstruction for imaging 364 keV photons of ^{131}I and evaluated the quantification accuracy and image quality of ^{131}I SPECT using multiple phantoms. Additionally, we show several examples of *in vivo* imaging performance with multiple static and dynamic ^{131}I -sodium iodide (NaI) SPECT/CT scans of mice.

Materials and Methods

Imaging system

The detector geometry and scanner design of VECTor are based on the U-SPECT system

(MILabs B.V., The Netherlands) [van der Have *et al.* 2009]. The VECTor system uses a CMP collimator (Figure 1, B) mounted in the center of three large NaI(Tl) gamma cameras in a triangular set up. The CMP collimator used for this study consists of a tungsten cylinder with a 43 mm thick wall and it enables collimating gamma photons up to approximately 600 keV. The collimator contains 162 pinholes, organized in clusters of 4 pinholes, each aperture having a diameter of 0.75 mm (Figure 1, A). The geometry of the collimator is described in detail in Goorden *et al.* 2013. All the pinhole clusters together observe a field-of-view that extends over the entire collimator tube diameter [Branderhorst *et al.* 2011]. The part of the field of view (CFOV) that is seen by all clusters simultaneously, the so called “central field-of-view” (an ellipsoid of 12x12x7mm), provides complete data sampling (sufficient angular data to reconstruct an image) without any translations of the animal bed. Note that such an area does not exist in traditional systems, since they require rotation of heavy gamma ray detectors to get sufficient angular data. Complete data of larger parts than the central field of view (up to total body mouse imaging) are obtained by moving the animal through the scanner in a spiral trajectory [Vaissier *et al.* 2012]. Data are collected in list-mode.

Image reconstruction

The activity distributions were reconstructed from the list-mode data using pixel-based OSEM [Branderhorst *et al.* 2010] with resolution recovery and compensation for distance-dependent pinhole sensitivity. The system matrix was calculated in three different ways in order to be able to compare the reconstructed images based on the same acquired data. The first model was based on ^{99m}Tc point source measurements [van der Have *et al.* 2008], resulting in a system matrix suitable for reconstructing ^{99m}Tc (140 keV) and other low-energy isotopes. The second model was the model that is normally used in VECTor for reconstructing positron emitters such as ^{18}F (511 keV). The position and orientation of the collimators and detectors were determined by means of a geometrical fit from the ^{99m}Tc point source measurements [van der Have *et al.* 2008]. Given the energy-specific values of the linear attenuation coefficients of the collimator (modeling edge penetration) and detector (modeling depth of interaction) materials, the system matrix was calculated by an analytical ray-tracing code as described in Goorden *et al.* 2016. The third model used the same ray-tracing code as the second, where the linear attenuation coefficients for the collimator and detector were set for 364 keV, resulting in a dedicated system matrix for reconstructing ^{131}I .

For the SPECT images shown, we reconstructed images for 50 iterations and 32 subsets [Branderhorst *et al.* 2010] with an isotropic 0.25 mm voxel grid. A 20% ^{131}I photo peak window

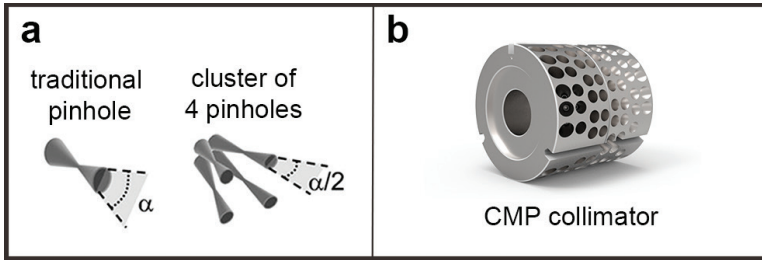


Figure 1. A - Traditional pinhole with opening angle α and cluster of 4 pinholes with approximately the same field-of-view and opening angle $\alpha/2$. B - CMP collimator optimized for imaging high energy gamma rays.

centered at 364 keV was used. Two background windows were placed on both sides of the photo peak window with a width of 4% of the photo peak energy, i.e. 14.2 keV each. Compton scatter correction was applied via the triple energy-window method [King *et al.* 2004]. All images were attenuation corrected and quantified as described in Wu *et al.* 2010.

Image volumes used for time-activity curve (TAC) generation were reconstructed as a dynamic frame sequence, decay-corrected, but otherwise unprocessed. TACs were generated for two ROIs that were manually drawn around the left lobe of the thyroid and salivary gland. The uptake in the ROI was calculated as the percentage injected dose per mL of tissue volume (%ID/mL).

For visual representation in the manuscript, reconstructed volumes of SPECT scans were post-filtered with a 0.35 mm FWHM 3D Gaussian filter.

Phantom experiments

The peak sensitivity of the collimator was measured in counts per second per MBq of activity (cps/MBq). This was done by scanning a small source of known activity, an eppendorf cup with 1.9 MBq ^{131}I -NaI, placed in the center of the “central field-of-view”. The same phantom scan was used to obtain a calibration factor required for absolute quantification of SPECT data [Wu *et al.* 2010, Wu *et al.* 2011].

Spatial resolution was determined with micro-hot-rod capillary resolution phantom scans. The phantom consists of 6 sectors with rods of 1.0, 0.8, 0.7, 0.6, 0.5 and 0.4 mm diameter. The minimal distance between the capillaries in each sector equals the capillary diameter in that sector. The phantom was filled with 76 MBq of ^{131}I - NaI solution. A two-hour SPECT scan with 30 minutes time frames was performed.

The quantification accuracy of reconstructed images was evaluated by means of scanning a 20 mL syringe (19 mm diameter) that was filled up to 6.5 mL with 12.69 MBq/mL ^{131}I -NaI and scanned for 2 hours. The activity in the syringe was measured in a dose calibrator (VDC-304, Veenstra Instruments, The Netherlands) with an accuracy of $\pm 3\%$ or ± 0.38 MBq/mL.

In vivo animal experiments

Animal experiments were performed with healthy C57Bl/6 mice according to protocols approved by the Animal Ethical Committee of the UMC Utrecht and in accordance with Dutch Law on Animal experimentation.

Two mice were anesthetized with isoflurane and injected with respectively 60 (mouse 1) and 5 MBq (mouse 2) ^{131}I -NaI via the tail vein. Fifteen minutes after the injection, 15-minute total body SPECT scans followed by 15-minute focused thyroid scans were performed on each animal. After the end of the SPECT acquisition total body X-ray CT scans were acquired.

One mouse was anesthetized with isoflurane and a tail vein catheter prefilled with saline was placed. Just after the start of a dynamic 30-minute focused thyroid SPECT scan the animal was injected with 26 MBq of ^{131}I -NaI. The first 15 minutes of the scan were acquired using 15-second time frames, for the remainder the frame duration was increased to one minute.

Results

Phantom scans

In this section we evaluate the ^{131}I imaging performance of VECTor based on resolution and uniformity phantom scans reconstructed with three types of system matrixes: one containing a dedicated system model for ^{131}I (364 keV) and two standard models used in VECTor, one for $^{99\text{m}}\text{Tc}$ (140 keV) and one for ^{18}F (511 keV) photons. This was done to assess the level of improvement in VECTor's performance for quantitative ^{131}I imaging.

Figure 2 shows 4 mm thick slice from the resolution phantom scan with ^{131}I . The reconstructed image resolution was evaluated for 120 and 30 minutes image acquisition. With the dedicated 364 keV modeling the best resolution was obtained for 120 minutes acquisition reconstruction: the minimal visible rods have 0.5 mm diameter. A decrease in acquisition time to 30 minutes, results in some resolution loss, yet all rods from the 0.6 mm segment can still be clearly distinguished. With the $^{99\text{m}}\text{Tc}$ model 0.7 mm resolution is reached for both acquisition times,

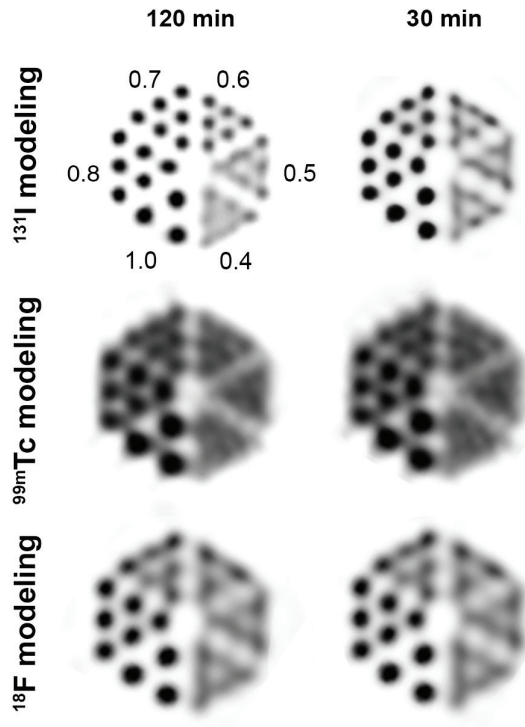


Figure 2. Slices from the reconstructed image of the hot-rod resolution phantom with 76 MBq ^{131}I .

but there is a much stronger background and the shape of the largest round rods appears triangulated. This is probably caused by the mismatch of the depth-of-interaction in the crystal between 140 and 364 keV. The ^{18}F model for image reconstruction results in the lowest resolution out of three models (>0.7 mm), yet shows only minor shape-distortions of the rods. In this case, the dominant inaccuracy in the modeling is probably the higher pinhole edge penetration at 511 keV that is assumed in the model. Even though the use of ^{18}F modeling for reconstructions of *in vivo* animal scans will not cause strong shape distortion of anatomical structures, essentially important spatial resolution will be noticeably degraded compared to dedicated ^{131}I modeling.

Figure 3 shows the results for a uniformly filled syringe scan, reconstructed by the same three system models as used in Figure 2. The syringe scan was used to assess the quantification accuracy of ^{131}I SPECT. From the volumes, 2 mm wide line profiles were extracted. The activity concentration of ^{131}I based on the measurement in the dose calibrator (“gold standard”) is indicated with an orange line on the profile plots. The average activity concentrations in the syringe calculated from the reconstructed image volumes were 13.15 ± 0.43 MBq/mL (^{131}I

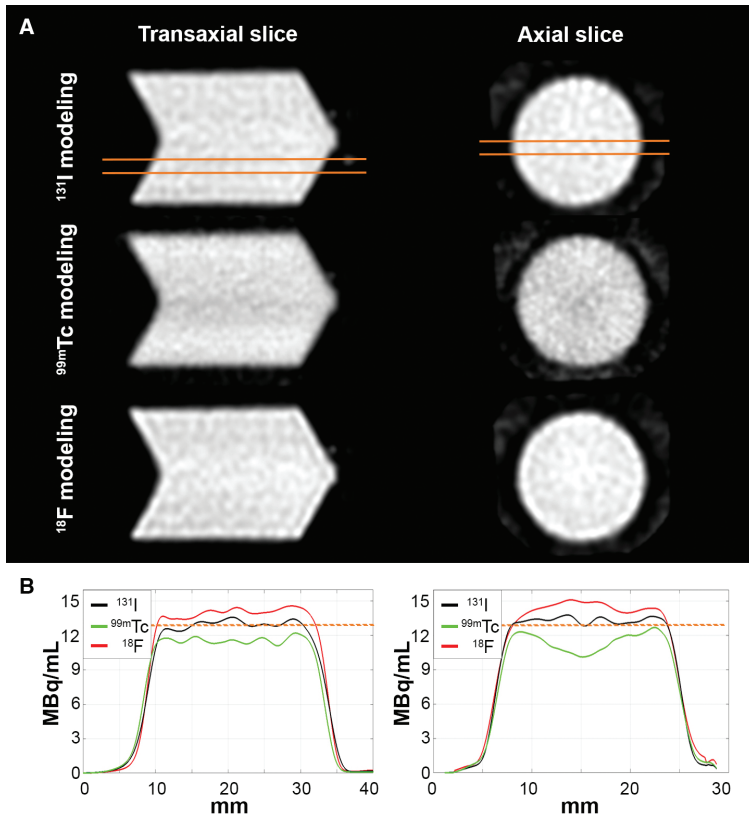


Figure 3. A - Axial and transaxial slices through the ^{131}I uniformly filled syringe, reconstructed with three different system models and compared at equal resolution. B - Line profiles through the phantom, drawn as indicated on the slices' images. The activity concentration measured in the dose-calibrator is indicated with orange lines on the line profile plots.

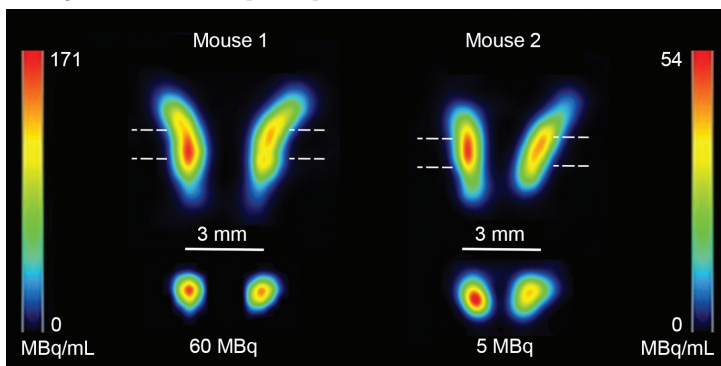


Figure 4. *In vivo* imaging performance of ^{131}I SPECT with VECTOR. Images show coronal and axial slices from focused 60 MBq (mouse 1) and 5 MBq (mouse 2) ^{131}I -NaI thyroid scans of two animals. Dashed white lines on the coronal view indicate position of axial view slices.

modeling, black), 11.59 ± 0.88 MBq/mL ($^{99\text{m}}\text{Tc}$ modeling, green) and 13.32 ± 0.40 MBq/mL

(^{18}F modeling, red). Relative to the “gold standard” value, this is respectively $+3.6 \pm 3.5\%$, $-8.5 \pm 7\%$ and $+5 \pm 3.2\%$. The peak-sensitivity for ^{131}I at the center of the collimator, measured with a small ^{131}I source, was determined to be 1578 cps/MBq or 0.16 %.

Based on quantification accuracy and image resolution achieved with the three system models compared in this work, the dedicated ^{131}I model showed to be the most suitable for applications in quantitative and high-resolution small-animal SPECT imaging.

In vivo animal scans

In this section we illustrate the *in vivo* imaging performance of VECTor with the dedicated system modeling for ^{131}I SPECT based on static and dynamic ^{131}I -NaI SPECT/CT scans of mice.

Figure 4 shows axial and coronal slices (1 mm thick) through the mouse thyroids from the focused scans with 60 MBq and 5 MBq of ^{131}I -NaI. For both levels of activity the two lobes of the glands are well separated on the images and the anatomical shape of the glands is as expected [Treuting *et al.* 2012]. Although the level of injected activity was decreased by a factor of 12 (from 60 to 5 MBq), the maximal activity concentration on the slices of the thyroid decreased by only a factor of 3.2 (from 171 MBq/mL to 54 MBq/mL). Considering i.v. administration of the tracer [Dou *et al.* 2013] and the fact that there is at least 222 GBq/mg iodine in the ^{131}I -NaI solution at the time of radiolabeling (information provided by GE Healthcare), the amount of iodide that was administered to mouse 1 (60 MBq) could have approached the recommended thyroid-blocking concentration of iodide for mice [Zuckier *et al.* 1998]. Thus, such a difference in ^{131}I -NaI concentrations in thyroids of the two animals (Figure 4, 5) might be related to saturation of possible binding sites in the glands at the higher level of activity concentration (60 MBq) [Zuicker *et al.* 1998, Zuickier *et al.* 2004, Brandt *et al.* 2012]. Complete understanding of this effect requires further investigations that lie outside the scope of this paper.

Maximum intensity projections (MIPs) of the total-body scans (Figure 5) illustrate the ^{131}I -NaI bio-distribution for the corresponding focused acquisitions. As expected, the tracer is seen to primarily accumulate in the stomach, thyroid and salivary glands.

Figure 6, A shows a set images of individual 15-second time frames (slice thickness 1 mm) that illustrates the ability to assess kinetics of the ^{131}I -NaI uptake in the thyroid. At the same time, quantitative dynamics of the uptake can be further investigated on the TACs (Figure 6, B). Due

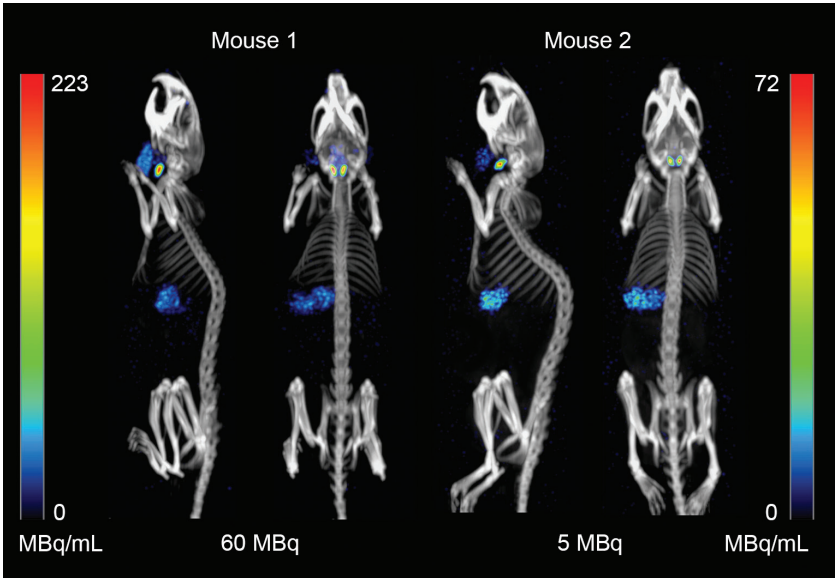


Figure 5. MIPs of total body mouse SPECT/CT scans with 60 MBq (mouse 1) and 5 MBq (mouse 2) of ^{131}I -NaI show accumulation of the compound in the stomach, thyroid and in the salivary glands.

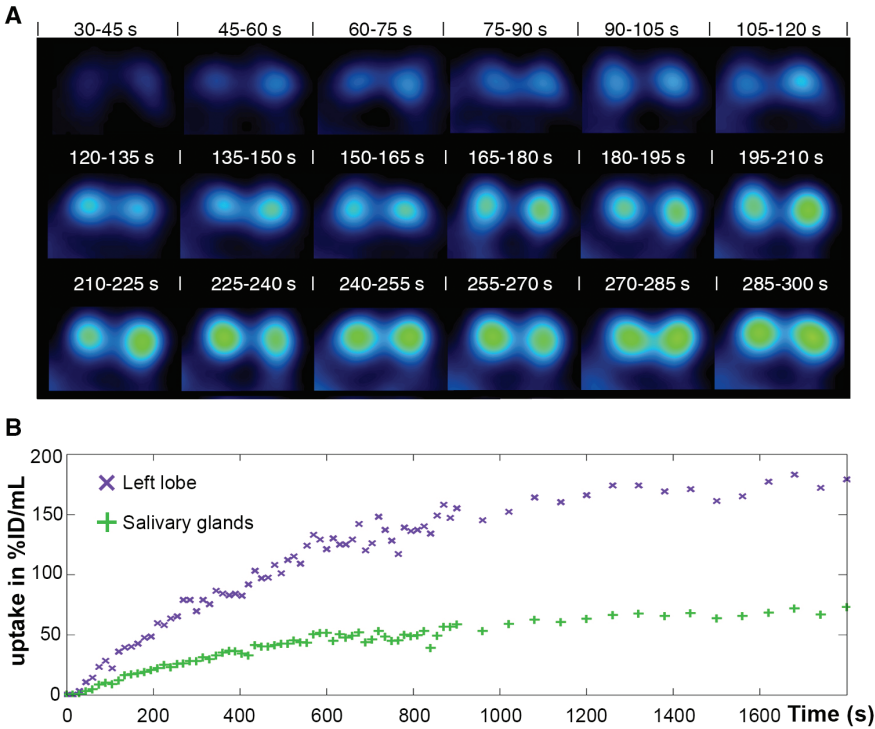


Figure 6. Axial slices through mouse thyroid (A) illustrate early stage dynamics of ^{131}I -NaI uptake in the mouse, obtained from focused dynamic 26 MBq Na^{131}I thyroid SPECT scan with 15-second time frames and ^{131}I modeling in the system matrix. (B) Time-activity curves of ^{131}I -NaI uptake by left lobe of the thyroid and salivary glands.

to high correlation between the uptake dynamics in the lobes of the thyroid, it was decided not to include the right lobe in the TACs graph to simplify the visual representation of the data, but the graph containing TACs from both lobes of the thyroid is available in the supporting information (Figure S1). It is clear from the set of dynamic images (Figure 6, A) that the accumulation of ^{131}I -NaI in the thyroid is rapid and starts from 30 seconds post injection onwards. Such results agree with both the expected biodynamics of NaI [Zuickier *et al.* 2004] and the dynamics of the tracer in the left lobe of the glands on the TACs (Figure 6, B), indicating that the ^{131}I -NaI concentration rapidly increases in the first 10 minutes post injection and retains a slow rate of increase for the remaining time of the scan.

Discussion

The use of ^{131}I for targeted radiotherapies of cancer is already widely applied in treatment of iodine-specific tumors [Chen *et al.* 2006] and novel approaches that are being developed today seem to have a high potential to treat a broad spectrum of tumor types [Weichert *et al.* 2014, Marsee *et al.* 2004, Mitrofanova *et al.* 2005]. At the same time, preclinical *in vivo* research using ^{131}I is rather difficult, due to poor image quality and limited resolution of ^{131}I SPECT [Miest *et al.* 2013]. Therefore, the majority of preclinical ^{131}I therapies require extensive *ex vivo* analyzing [Weichert *et al.* 2014]. The phantom experiments in this work showed that with optimized system modeling and a dedicated high-energy collimator high-resolution quantitative imaging of the γ -rays from ^{131}I becomes possible with a preclinical SPECT-PET system, despite the relatively high energy of the emitted photons.

In small-animal imaging, reconstructed image resolution plays an important role as it allows to distinguish between different organs that can accumulate iodine and might lie in relative proximity to each other (e.g., the thyroid and salivary gland). At the same time, a high resolution allows to minimize partial-volume-effect-related errors in quantification of SPECT images [Hwang *et al.* 2008]. The resolution phantom scan in the paper illustrates that sub-mm resolution ^{131}I SPECT can be performed by means of dedicated ^{131}I system modeling and use of a high-energy clustered pinhole collimator. Furthermore, a high quantification accuracy ($+3.6 \pm 3.5\%$ from the “gold standard”, Figure 3, B) of SPECT scans was found. Such performance of VECTor not only improves current ^{131}I SPECT image quality [Fan *et al.* 2014] for the assessment of compounds’ bio-distributions, but also provides an opportunity to perform quantitative analysis of the uptake, and based on that to calculate animal-specific *in vivo* 3D dose distribution [Sgouros *et al.* 2004].

The results of the *in vivo* animal evaluation using ^{131}I -NaI imaging illustrated that a high level of detail (e.g., a clear shape and separation between the lobes of the thyroid) can be achieved already in total body scans with only 5 MBq of activity (Figure 5), and further improvement in the visible level of details is possible with an increase in injected activity (Figure 5).

Tracer pharmacokinetics provides the link between the distribution of radioactivity in the tissue over time and relevant physiological parameters or disease state, particularly during development of new therapeutic approaches. Thus, dynamic imaging capabilities were further assessed with a dynamic ^{131}I -NaI scan of the mouse thyroid using 15-second time frames. We showed that it is possible to assess tracer dynamics in the thyroid and salivary glands not just from the time-activity curves (Figure 6, B), but also from the dynamic sequence of SPECT images (Figure 6, A), illustrating the bio-distribution of the radiolabelled compound within the organ or system of organs. We expect that this capability can be translated to other applications of ^{131}I imaging for, e.g., dynamic analysis of intra-tumoral accumulation of ^{131}I -labelled compounds. At the same time, because most organs are larger than the thyroid, the visible level of detail relative to the organ size can be effectively higher.

Radioactive iodine, unlike other NIS substrates, can be oxidized and bound to proteins and lipids [McFarlane *et al.* 1956]. Therefore, the uptake of other iodine- or NIS-based imaging substitutes that might be used for imaging of response to ^{131}I therapy will be partially inhibited by already present iodine in the animal body [Franken *et al.* 2010]. As a result, their bio-distribution may not be directly proportional to that of the therapeutic ^{131}I compound (or the other way around). With the currently obtained imaging performance for ^{131}I , we expect that it is possible to directly monitor response to therapy in mice with ^{131}I SPECT, instead of having to rely on $^{99\text{m}}\text{Tc}$ -pertechnetate, ^{124}I or ^{123}I as a substitute [Weichert *et al.* 2014, Marsee *et al.* 2004, Miest *et al.* 2013]. Additionally, not requiring an additional imaging agent during monitoring of ^{131}I therapy will decrease the total cost and complexity of the study.

Conclusion

We have shown that it is possible to quantitatively image ^{131}I and reach resolution below 0.6 mm. This was performed with a SPECT-PET-CT system equipped with a dedicated high-energy collimator. Employing dedicated energy-specific system modeling is very advantageous for obtaining optimal image quality. Dynamic *in vivo* ^{131}I -NaI SPECT imaging capabilities were illustrated in a mouse as well.

Supporting Figures

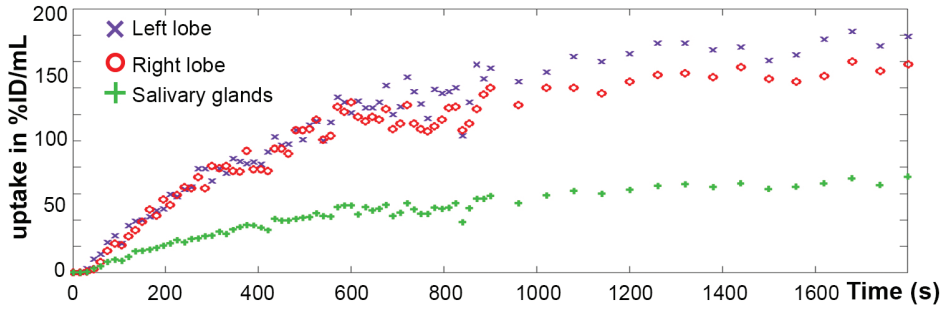


Figure S1. Time-activity curves (TACs) of ^{131}I -NaI uptake by left and right lobes of the thyroid and salivary glands. TACs were obtained from focused dynamic 26 MBq ^{131}I -NaI thyroid SPECT scan with 15-second time frames and ^{131}I modeling in the system matrix.

Chapter 4

Ultra-high-sensitivity sub-mm mouse SPECT

This chapter is based on the publication:

Ivashchenko O, van der Have F, Goorden MC, *et al.* Ultra-high-sensitivity sub-mm mouse SPECT. *J Nucl Med.* 2015; 56(3):470-475.

-This publication has been selected as a recipient of Alavi-Mandell publication award 2016.

Abstract

SPECT with sub-MBq amounts of tracer or sub-second time resolution would enable a wide range of new imaging protocols such as screening tracers with initially low yield or labeling efficiency, imaging low receptor densities or even performing SPECT outside regular radiation laboratories. To this end we developed dedicated ultra-high-sensitivity pinhole SPECT.

A cylindrical collimator with 54 focused 2.0 mm diameter conical pinholes was manufactured and mounted in a U-SPECT⁺ stationary SPECT system (MILabs, The Netherlands). The system matrix for image reconstruction was calculated via a hybrid method based on both ^{99m}Tc point source measurements and ray-tracing analytical modeling. SPECT image reconstruction was performed using Pixel-based OSEM. Performance was evaluated with phantoms, and low-dose bone, dynamic kidney and cardiac mouse scans.

The peak sensitivity reaches 1,3% (13080 cps/MBq). Reconstructed spatial resolution (rod visibility in a micro-Jaszczak phantom) was 0.85 mm. Even with only a quarter MBq of activity, 30-min bone SPECT scans provided surprisingly high levels of details. Dynamic dual-isotope kidney and ^{99m}Tc-sestamibi cardiac scans were acquired with a time-frame resolution down to 1 s.

The high sensitivity achieved increases the range of mouse SPECT applications by enabling *in vivo* imaging with less than a MBq of tracer activity or down to one second frame dynamics.

Background

The trade-off between resolution and sensitivity is a constant challenge in preclinical SPECT imaging. The small size of the animals that are imaged with preclinical scanners has tended to put the main focus of SPECT development in the last decade on resolution improvements [Schramn *et al.* 2003, Beekman *et al.* 2005, Nuyts *et al.* 2009, van der Have *et al.* 2009, Deleye *et al.* 2013]. As a result, the sensitivity (fraction of emitted photons detected) of modern dedicated high-sensitivity multi-pinhole collimator systems rarely exceeds 0.2%. Improvement of the sensitivity characteristics would offer several significant advantages. Imaging could, for instance, be performed more rapidly, thereby allowing a higher throughput for tracer screening applications or observation of dynamic processes with very good time resolution. In addition, with necessity of less radioactive tracer to be used, it would be possible to, for example,

perform *in vivo* imaging of low-capacity receptor systems, thus aiding research into new tracer compounds, or reducing the costs and easing the license requirements of an experiment (Table S1).

Non-collimated high-sensitivity SPECT was developed by Mitchell *et al.* 2009 using two closely spaced scintillator detectors. This approach allows a high (40%) detection efficiency to be reached but currently restricts applications to resolutions at a level of ~1 cm.

The aim of the present work is to develop an ultra-high-sensitivity SPECT using a collimator that aims to have a high sensitivity and still allow sub-mm resolution 3D and 4D SPECT imaging. We shall evaluate the performance of the new collimator using phantoms as well as static and rapid dynamic ultra-low-dose imaging in live mice.

Materials and methods

SPECT system

The new collimator was mounted in the U-SPECT⁺ (MILabs, Utrecht, The Netherlands) series of scanners [Ivashchenko *et al.* 2014]. This system employs three 595x472 mm NaI(Tl) stationary detectors, a set of replaceable focusing multi-pinhole collimators and a user interface that aids both total body SPECT or 3D focused imaging [Branderhorst *et al.* 2011]. Other details on the original system design can be found in [Beekman *et al.* 2005].

Collimator design

The ultra-high-sensitivity collimator developed in here was designed to fit mouse-sized animals. It consists of a lead cylinder with an inner bore diameter of 46 mm and wall thickness of 30 mm (Figure 1) with 54 2.0-mm diameter conical pinholes positioned in four rings. These results in gamma detector-to-pinhole aperture distance of 247 mm and pinhole-to-center of the CFOV distance of 23 mm. As one can see from Figure 1, the centre of each pinhole is located on the inner wall surface of the collimator tube. By not having a conical part of the pinhole on the inside we intended to minimize the object-to-pinhole and maximize pinhole-to-detector distance, in order to additionally improve sensitivity and resolution (by increasing magnification factor) characteristics. The two most central rings (2-3; Figure 1) contain 15 pinholes with 25.1 degrees opening angles, while the outer rings (1,4; Figure 1) contain a combination of 12 pinholes with 21.2 or 24.2 degrees opening angle. All pinholes together form an hourglass-shaped field of view (FOV, Figure 1) that is used for data acquisition via scanning focus method [Branderhorst

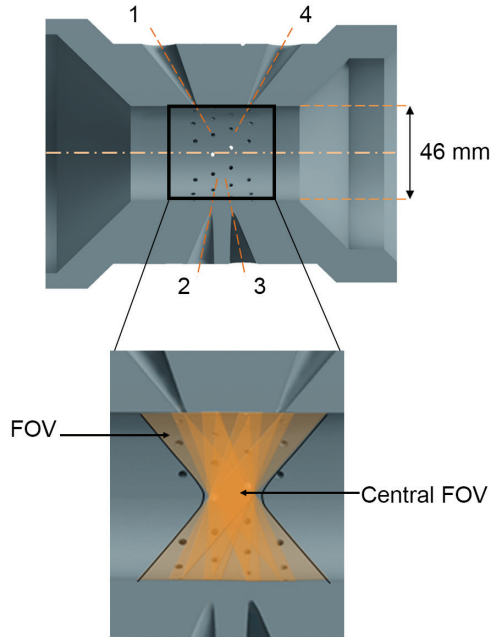


Figure 1. Cross-section of the ultra-high-sensitivity collimator with illustration of pinholes positioned in the two outer (1,4) and two inner (2,3) pinhole rings. Zoomed view (bottom) on central part of the collimator illustrates shape and position of the field of view (orange area).

et al. 2011]. The central part of the FOV (an ellipsoid of 12x12x7mm), the so-called central FOV (Figure 1), is seen by all pinholes simultaneously and provides complete data without any bed movement (i.e. within one bed position). Images from each pinhole are directly projected on the detector's surface and create slightly overlapping projections.

System calibration and image reconstruction

The system's exact geometry was determined by ^{99m}Tc point source measurements [van der Have *et al.* 2008] and the system matrix was subsequently calculated by an analytical model based on ray-tracing [Goorden *et al.* 2011].

Images were reconstructed from the list-mode data using pixel- based OSEM [Branderhorst *et al.* 2010] with resolution recovery and compensation for distance dependent pinhole sensitivity. For all SPECT images shown, we used 32 subsets and 15 iterations image reconstruction parameters as well as an isotropic 0.4 mm voxel grid. Compton scatter correction was applied via triple energy-window method [King *et al.* 2004] with use of either one 20% (centered at 140 keV) or two 15% (centered at 171 keV and 245 keV, respectively) photopeak windows for

^{99m}Tc and ^{111}In isotopes, respectively. The background windows were placed on each side of the photopeak with a width of 3% (^{99m}Tc) and 2.5% (^{111}In) of the corresponding photopeak. All images were attenuation corrected as described in Wu *et al.* 2010 and Wu *et al.* 2011. The reconstructed volumes of all SPECT scans were post-filtered with a 1.0 mm FWHM 3D Gaussian filter. Time-activity curves (TACs) were generated for manually drawn volumes of interest (VOI), using decay-corrected but otherwise unprocessed images, reconstructed as a dynamic frame sequence.

Phantom scans

The sensitivity of the collimator along the axial and transaxial directions was measured in counts per second per MBq of activity (cps/MBq) by scanning a ^{99m}Tc point source of known activity [van der Have *et al.* 2008] through the center of the FOV. The resolution was determined with micro-Jaszczak hot-rod capillary resolution phantom scans. The phantom used consists of 6 sections with rods of 1.7, 1.5, 1.3, 1.0, 0.95 and 0.85 mm diameter, that all together provide 0.21 mL volume for filling with activity. The minimum distance between the capillaries in each section equals the capillary diameter in that section. It was filled with 0.25 or 5 MBq of ^{99m}Tc -pertechnetate (concentrations of 1.19 and 23.8 MBq/mL respectively). Dynamic 30-min acquisitions using 5-min frames were performed.

Animal studies

The animal experiments were performed with C57Bl/6 mice according to protocols approved by the Animal Ethics Committee of the UMC Utrecht and in accordance with Dutch Law on Animal experimentation. All SPECT scans were acquired for 30 min with the ultra-high-sensitivity collimator. Every animal used for imaging was anesthetized with isoflurane and intravenously injected with tracer activity via the tail vein. For dynamic image acquisitions a tail vein catheter was used for the tracer injections.

Low-dose bone SPECT scans

Two mice were anesthetized and injected with 0.25 and 3.5 MBq of ^{99m}Tc -methylene diphosphonate (MDP), respectively. Half an hour after the injection subsequent total body, focused pelvis, and focused skull scans were performed for each animal. The total number of animal bed positions used during data acquisition in those scans varied from 7 (focused skull) to 45 (total body), dependent on the animal and corresponding scan area sizes.

Low-dose renal function SPECT

A mouse was anesthetized and the kidneys of the animal were selected as scan area of interest, which required 2 animal bed positions. Just after the start of the 15 seconds frame dynamic SPECT acquisition the mouse was subsequently injected with 1.5 MBq of ^{99m}Tc -mercaptoacetyltriglycine (MAG3) and 1.5 MBq of ^{111}In - diethylene triamine pentaacetic acid (DTPA). The time between two activity injections was around 45 seconds. TACs were generated for two volumes of interest (VOI), that were manually drawn around each kidney. The curves were smoothed via use of nearest-neighbor averaging over three points.

Fast dynamic cardiac scan

Two mice were anesthetized and the heart of the animals was selected as scan area of interest which required only a single bed position. Just after starting the dynamic SPECT acquisitions with 1 second frames the mice were injected with either 9 MBq (mouse 1) or 15 MBq (mouse 2) of ^{99m}Tc - sestamibi. TACs were generated for equal sized spherical VOIs, placed in the aorta and myocardium tissue regions. The required size and position of the VOIs was determined from the reconstructed volume for the total duration of the scan. The TACs were subsequently generated from the dynamic image sequence (for min 0-10 of the acquisition) and smoothed via nearest-neighbor averaging over three points.

Results

Phantom studies

Figure 2, A shows 4 mm thick slices (sum of 10 subsequent 0.4 mm thick slices) from the dynamic micro-Jaszczak resolution phantom scans with ^{99m}Tc . Even for the shortest acquisition of 5 min rods with diameters down to 1.1 mm using 0.25 MBq and down to 0.85 mm using 5 MBq can be distinguished. Within 30 min of acquisition the minimal visible rod diameter for the 0.25 MBq activity scan improves to 0.95 mm. Figure 2, B illustrates sensitivity profiles along the axial (Z) and transaxial (X) directions through the center the collimator's FOV. The peak-sensitivity for ^{99m}Tc at the center of the collimator was determined to be 1.3% (13080 cps/MBq) and decreases to the lowest values of 1.0% (along Z) and 0.81% (along X) on the edges of the central FOV.

Low-dose bone scans

Figure 3 shows maximal intensity projections (MIPs) of the ^{99m}Tc -MDP mouse total body, focused pelvis and focused skull scans. The top and side view MIPs of the total body scan

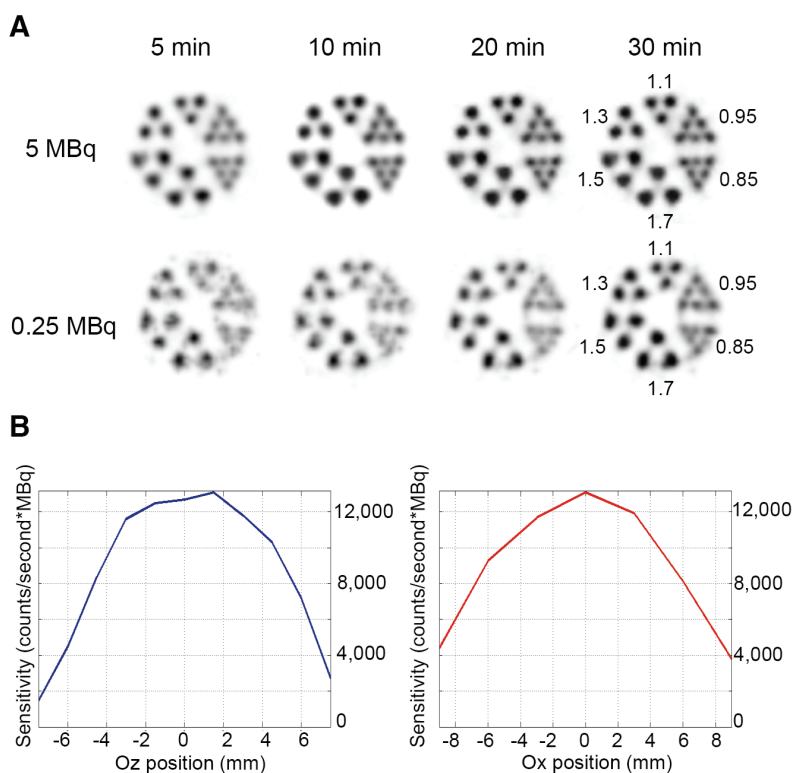


Figure 2. A - 5 MBq and 0.25 MBq ^{99m}Tc resolution phantom scans for different acquisition times (5, 10, 20 and 30 min). The smallest visible rod diameter for the 30-min acquisition was 0.85 mm. In the 5-min acquisition images, the 1.1 mm rods can be seen for all activities used. B - sensitivity profiles for a single bed position along axial (Z) and transaxial (X) directions through the center of the collimator's FOV for ^{99m}Tc .

illustrate that a 3.5 MBq scan provides details of the anatomical structures in the mouse skeleton, such as in the pelvis, in the skull and in both upper and lower limbs. A decrease of the injected tracer activity by a factor of 14 to 0.25 MBq partially degrades the visible level of details, but the resulting image still reveals the 3D anatomical structure of the skeleton. Reconstructions of separate focused pelvis and skull scans show improvement of images in terms of visible details compared to the total body images obtained with the same tracer activity.

Dual-isotope kidney scan

Figure 4 presents the ^{99m}Tc -MAG3/ ^{111}In -DTPA dynamic kidney scan. Both tracers are primarily used for evaluation of tubular filtration and result in rapid renal clearance of the compound [Melis *et al.* 2010, Sfakianakis *et al.* 1997]. Fast clearance of the tracers in combination with

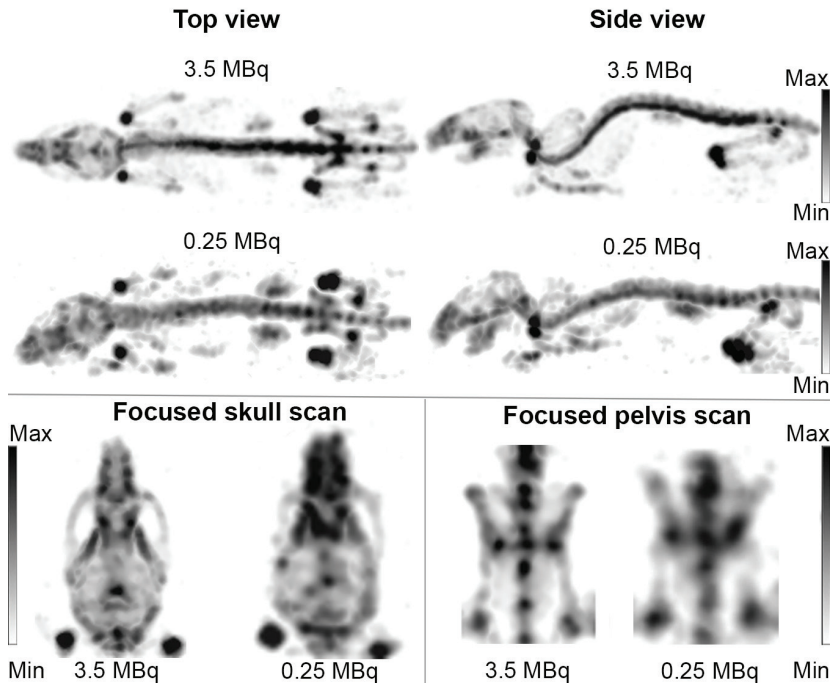


Figure 3. Top and side MIP of 30-min mouse total body ^{99m}Tc -MDP mouse scan. In 3.5 MBq scan, high level of anatomical detail is provided in upper and lower limbs, pelvis and skull. In 0.25 MBq scan, uptake in entire skeleton can be detected, and skull and pelvis still show high level of details. When focused scans were performed, image quality was obviously improved for both scan areas (skull and pelvis) and levels of tracer activity.

animal-size-related limitations for maximally allowed volumes of injections (0.2 mL / animal for the i.v. administration routes) [van Zutphen *et al.* 2001] and low labeling efficiency of ^{111}In -DTPA [Brom *et al.* 2012] hampers application of those tracers for SPECT imaging with mice, particularly when dynamic imaging needs to be performed. Figure 4, A shows a set of individual 15 seconds frames (slice thickness 2 mm) that illustrates the difference in the tracers' dynamics. It is clearly visible that renal filtration of ^{111}In -DTPA (hot) takes place mainly in the medulla cavity region, while filtration of ^{99m}Tc -MAG3 (green) involves both the renal cortex and the medulla cavity. Also, ^{99m}Tc -MAG3 follows three defined stages of filtration: uptake (0-75 s), plateau (75-180 s) and clearance (180-1800 s).

In case of ^{111}In -DTPA the uptake of the compound (0-120 s) is rapidly followed by the clearance stage (120-1800 s) with no noticeable period of a plateau. Such results agree with both individual bio dynamics of the tracers [Jouret *et al.* 2010, Tantawy *et al.* 2012] and simultaneous tracers'

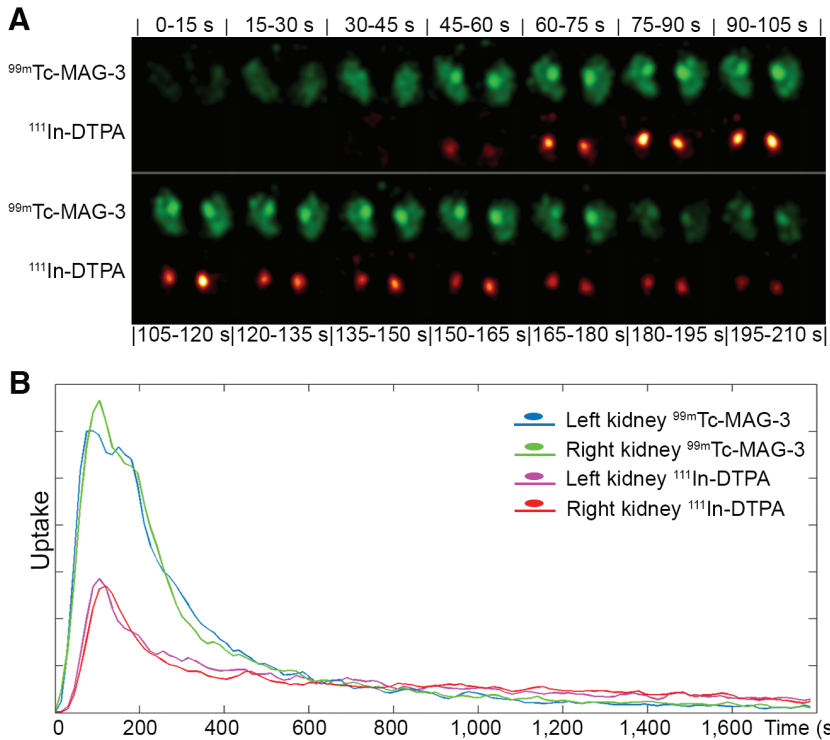


Figure 4. 2 mm thick slices (A) of dynamic 15-s frames for dual- isotope $^{99m}\text{Tc-MAG3}$ (green) and $^{111}\text{In-DTPA}$ (hot) kidney scan (time delay between injections was 45 s). Images illustrate the difference in tracer dynamics, with slower uptake/clearance and longer plateau period for $^{99m}\text{Tc-MAG3}$, when compared to $^{111}\text{In-DTPA}$. B - time-activity curves of $^{111}\text{In-DTPA}/^{99m}\text{Tc-MAG3}$ uptake by left and right kidneys.

dynamics shown on the TACs (Figure 4, B), which indicates that the tracers reach their maximal uptake around 130 s after the injection and are washed out within 600 s. The relatively small time delay in the beginning of $^{111}\text{In-DTPA}$ uptake on the TACs can be explained by the 45 s difference between the two tracers' injection times that wasn't taken into account neither during TACs generation, nor during division onto tracers' uptake stages.

Fast dynamic cardiac scan

Figure 5 shows 0.4 mm thick slices from the short (Figure 5, A) and long (Figure 5, B) cardiac axes, obtained from reconstructions of 10-min acquisition segment (minute 4-14) of the dynamic 30-min $^{99m}\text{Tc-sestamibi}$ scan (mouse #1). The images illustrate a clear separation between the left and right ventricular walls, as well as details of the myocardium. The TAC of tracer dynamic in the aorta (green lines, mouse 1 & 2, Figure 5, C) contains two defined peaks

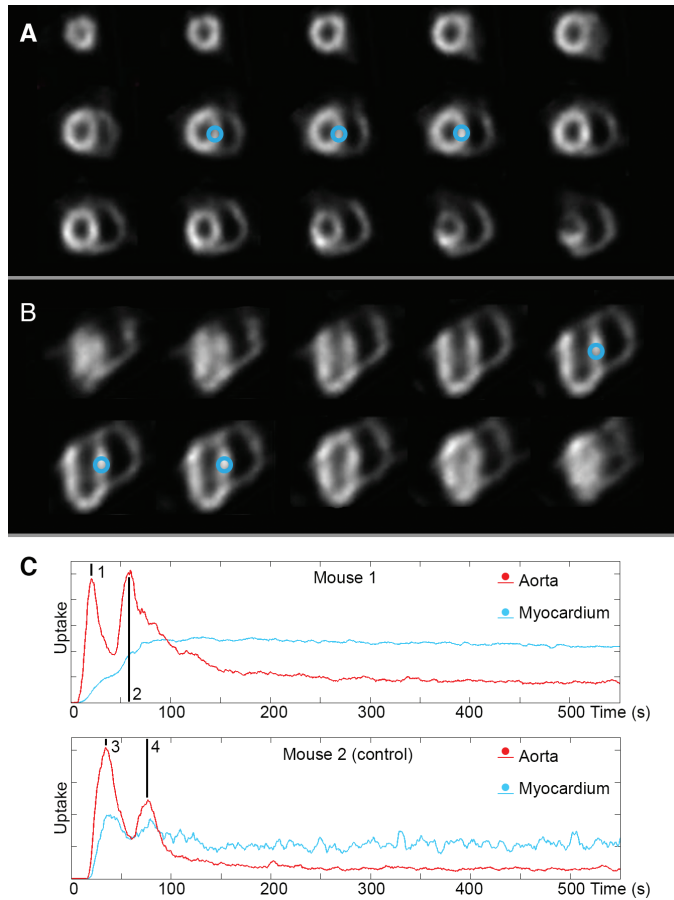


Figure 5. A, B- 0.4 mm thick slices of short and long axes through the mouse heart (mouse 1), obtained from reconstructions of 10-min acquisition segment of the half an hour focused ^{99m}Tc -sestamibi scan. These images clearly show the separation between the left and right ventricular wall, as well as details of the structure of the myocardium. C - time-activity curves visualizes 1-s time resolution tracer dynamics in the aorta and myocardium tissue. Arrows 1, 2 (mouse 1) and 3, 4 (mouse 2) indicate the first pass of activity in aorta after the initial activity injection and secondary activity infusion of ^{99m}Tc -sestamibi, respectively. VOI used for the generation of myocardium tissue TACs is indicated with blue circles on A, B.

in tracer concentration around the 30- and 70-s time points (1-2 & 3-4, Figure 5, C). Most probably, the first peak corresponds to the initial pass of the activity through the heart. The presence of the second peak (2, 4) at the 70-s time point can be explained by the secondary activity infusion in the animal during the post-injection flushing of the tail vein catheter with saline. We assume that the difference in amplitude and peak position on TACs shown in Figure 5, C is caused by differences in activity injection speeds between those two experiments. The tracer concentration in the myocardium tissue (blue Figure 5, C) rapidly increases after each activity infusion and retains a constant level for the remaining time of the

scan.

Discussion

The size of animals that are used in preclinical molecular imaging sets two main requirements to performance characteristics of preclinical SPECT scanners. They need to have high-enough resolution in order to be able to visualize the animal with a sufficient level of details, and their sensitivity needs to remain high enough in order to have a sufficient count rate for obtaining images with small amounts of injected tracer activity. The current work showed the results of the evaluation of a new ultra-high-sensitivity collimator, that allows 3D sub-mm mouse SPECT and ultra-low-dose or fast-dynamic imaging applications in the U-SPECT⁺ system.

The resolution phantom scans illustrated that the collimator can reach its peak 0.85 mm reconstructed image resolution within 5-min acquisition with 5 MBq in a Jaszczak phantom and even maintain sub-millimeter resolution (0.95 mm) for a 0.25 MBq activity level when a longer acquisition time (30 min) is used. The peak sensitivity of the collimator reaches 1.3% for ^{99m}Tc, what slightly exceeds an estimated value of 1.2% for double-cone pinhole geometry model [Rentmeester *et al.* 2007]. Such performance makes the collimator most suitable for either sub-MBq static or several MBq fast-dynamic scans.

The results of the animal evaluation on low-dose bone imaging illustrated that a quite high level of details can be achieved with just several MBq (3.5 MBq) or even a 0.25 MBq tracer activity when static images are acquired. It was shown that in cases when finer details need to be achieved for the same activity level, local focusing on the area of interest (Figure 3 skull, pelvis) can be used for resolution and general image quality improvement. This application of focused scanning [Branderhorst *et al.* 2011] can be beneficial for imaging with tracers that cannot reach high labeling efficiency or for imaging of organs and tissues with relatively low specific uptake (e.g., different tumors, brain).

Often, in order to obtain good time resolution, dynamic SPECT imaging requires injections of high tracer activities. Because of size-related limitations on maximally allowed volumes of injections [van Zutphen *et al.* 2001], dynamic imaging in mice necessitates the use of tracers with high activity concentrations or results in long time frames [Vaissier *et al.* 2012]. The kidney scan shown in this work demonstrates that with the ultra-high-sensitivity collimator, a time frame of as low as 15 s can be reached with a sub-MBq level of activity. This ability

allows analyzing of tracer dynamics not just from the TACs, but also from the dynamic sequence of SPECT images, illustrating the bio distribution of the radiolabelled compound within the organ or system of organs. At the same, if repetitive scans need to be performed, the low level of required activity would prevent the animal from accumulating a high radiation dose that can harm the animal or influence the reliability of the results. The frame rate of SPECT can be further increased by the use of higher tracer activities or more focused scanning, using a small number of bed positions. Scanning of the area that occupies several bed positions will require overhead time for animal bed movement that ultimately will present the main limitation on the shortest possible frame length for SPECT acquisitions. In cases when the organ or scan area of interest fits within the central FOV (like in the case of cardiac scan presented in Figure 5), time frames can be shortened down to 1 s. However, due to the high sensitivity of this collimator, focused scanning with more than ~30 MBq in the central FOV (using the U-SPECT⁺ system) will result in more than 20% count loss, partly due to limitations of currently used read-out electronics.

Conclusions

Current work represents and evaluates an ultra-high-sensitivity mouse SPECT collimator that has 1.3% peak sensitivity and still reaches 0.85 mm reconstructed spatial resolution for ^{99m}Tc. The animal scans presented in this paper illustrate the possibility of performing dynamic SPECT with 1s time frames or performing static SPECT with small amounts of activity (fractions of MBq). Based on its performance, the collimator can be used (i) as one of the ways of reducing the animal dose during follow-up molecular imaging studies, (ii) to improve the frame rate for dynamic bio-kinetics screening during the development of new tracers or imaging of biological processes with fast dynamics. Additionally, it can increase the possible number of applications for either (iii) imaging of organs that have low specific uptake, (iv) imaging with tracers and nanocarriers that have low labelling efficiency, (v) reduce the cost of a study or (vi) even simplify the radiation safety license application procedure via reduction of required activities (in some cases below the radiation safety license exemption level, Table S1.).

Supporting Tables

Table S1. Example values of the exemption limits for several radioactive isotopes that are usable in SPECT. If the amount of activity that is used in total is kept below these limits, a license to perform the experiment is not required.

Radionuclide	Activity in MBq ^a (the Netherlands)	Activity in MBq ^b (USA)
^{99m} Tc	10	37
¹¹¹ In	1	3.7
¹²³ I	10	3.7
⁶⁷ Ga	1	37

^aNational Radiological Protection Board (NRPB) of the Kingdom of the Netherlands (NRPB-R306), directive 96/29.

^bUS Nuclear Regulation Commission, 10 CFR, App. C, Part 20.

Chapter 5

SPECT/CT imaging of Pluronic nanocarriers with
varying PEO block length and aggregation state

This chapter is based on the publication:

Arranja A*, **Ivashchenko O***, Denkova AG, *et al.* SPECT/CT imaging of Pluronic nanocarriers with varying PEO block length and aggregation state. *Mol Pharm.* 2016; 13(3):1158-65.

**equal contribution*

Abstract

Optimal biodistribution and prolonged circulation of nanocarriers improves diagnostic and therapeutic effects of EPR-based nanomedicines. Despite extensive use of Pluronics in polymer-based pharmaceuticals, the influence of different PEO block length and aggregation state on the biodistribution of the carriers is rather unexplored. In this work, we studied these effects by evaluating the biodistribution of Pluronic unimers and cross-linked micelles with different PEO block size. *In vivo* biodistribution of ^{111}In -radiolabeled Pluronic nanocarriers was performed in healthy mice using SPECT/CT.

All carriers show fast uptake in the organs from the reticuloendothelial system followed by a steady elimination through the hepatobiliary tract and renal filtration. The PEO block length affects the initial renal clearance of the compounds and the overall liver uptake. The aggregation state influences the long-term accumulation of the nanocarriers in the liver.

We showed that the circulation time and elimination pathways can be tuned by varying the physicochemical properties of Pluronic copolymers. Our results can be beneficial for the design of future Pluronic-based nanomedicines.

Background

Nanocarriers including polymers, micelles and nanoparticles, have a number of advantages over low molecular weight agents [Duncan *et al.* 2011]. Application of these carriers is particularly interesting in oncology, where the leaky vasculature of tumors and the impaired lymphatic drainage allows to reach high drug accumulation and retention via the well-known Enhanced Permeability and Retention (EPR) effect [Lammers *et al.* 2008]. This effect strongly depends on the blood circulation time and biodistribution of the nanocarriers, parameters that are mostly determined by their physicochemical properties such as size, shape and surface charge [Duan *et al.* 2013].

The development of polymer-based nanocarriers is particularly powerful since they can be easily tailored with appropriate functionalization and/or size to meet the set requirements and more efficiently deliver their cargo to diseased sites. The polymer selection criteria for clinical applications includes controlled stability, biocompatibility, aqueous solubility and availability to attach chemical groups that can be used for targeting, imaging or therapy. Among the several

polymers used for the development of polymer-based nanocarriers, Pluronics are probably the most broadly investigated. Pluronics are amphiphilic triblock copolymers composed of PEO-PPO-PEO, where PEO stands for poly(ethylene oxide) and PPO denotes poly(propylene oxide). Due to their amphiphilic properties, Pluronic unimers can aggregate and self-assemble into micelles composed by a hydrophilic hydrated PEO corona and hydrophobic PPO core, which can be used to incorporate hydrophobic drugs. This self-assembling mechanism depends mainly on the solution temperature and composition (e.g., salts and proteins) as well as on the polymer concentration, resulting in micelle formation above a critical micelle temperature (cmT) and/or polymer concentration (cmc). Therefore, Pluronic micelles have a dynamic nature which may result in their rapid disintegration upon dilution in the bloodstream [Arranja *et al.* 2014, Talelli *et al.* 2012], ultimately affecting their biodistribution.

Despite the broad use of Pluronics in pharmaceutical formulations, very few groups studied the effects influencing the *in vivo* biodistribution of Pluronic copolymers [Grindel *et al.* 2002, Willcox *et al.* 1978, Batrakova *et al.* 2004, Wang *et al.* 1995]. To our knowledge, only one group studied the effect of the aggregation state using different polymer doses [Batrakova *et al.* 2004], whereas the influence of the PEO block length and aggregation state using similar concentrations is rather unexplored.

In this work, we show a strategy to compare the biodistribution of molecular and core-stabilized supramolecular nanocarriers based on Pluronic copolymers. This approach eliminates the limitation associated with the dynamic nature of copolymer micelles and allows using similar concentrations of both nanocarriers, resulting in more meaningful comparison of their biodistribution. We used Single Photon Emission Computed Tomography (SPECT) and performed longitudinal biodistribution studies of ¹¹¹In-labeled Pluronic nanocarriers (unimers and stabilized micelles). This SPECT isotope (¹¹¹In) was selected as a molecular imaging agent due to its prolonged physical half-life (67.3 hours) making it suitable for imaging of compounds with prolonged blood circulation. Two Pluronics (P94 and F127) with similar PPO block lengths and different PEO block masses (≈ 1100 and 4250 g/mol) were used. In addition, the early biokinetics of the most frequently applied Pluronic (F127) was investigated.

Materials and methods

Functionalization of Pluronic copolymers with DTPA

Pluronic block copolymers (P94 and F127, BASF) were purified from low molecular weight contaminants. They were modified with 1,1-carbodiimidazole (CDI-Pluronic) followed by primary amines (Pluronic-NH₂) using a procedure similar to the one in Lu *et al.* 2003 for Pluronic F68. The modified chelator p-SCN-Bn-DTPA was conjugated to the amine terminated copolymers using a procedure previously reported for the diblock PEG-PCL [Hoang *et al.* 2009]. Briefly, p-SCN-Bn-DTPA dissolved in DMSO (50 mg/mL) was added in a 1:1 molar ratio of reacting groups to a 25 mg/mL solution of the copolymers F127-NH₂ or P94-NH₂ in sodium bicarbonate buffer (0.1 M, pH 8.5). The solutions were stirred at room temperature for at least 4 h. Characterization of the raw, CDI-activated and amine modified copolymers was performed by ¹H-NMR (Bruker WH 300 MHz instrument) after reaction with trichloroacetyl isocyanate at room temperature in deuterated chloroform, and analyzed in their powder form by FT-IR in a PerkinElmer Frontier FT-IR (midIR) combined with a MKII Golden Gate set-up equipped with a diamond crystal from Specac.

Preparation of cross-linked Pluronic F127 and P94 micelles with DTPA

Stabilized polymeric micelles (SPM) were prepared from a mixture of 10% F127-DTPA or 3.65% P94-DTPA functionalized copolymers with regular copolymers in aqueous solution at a total copolymer concentration 2.5% w/w. The self-assembled Pluronic micelles were then cross-linked as previously described in Arranja *et al.* 2014. Free remaining unimers and free p-SCN-Bn-DTPA were removed, respectively, by diafiltration at 5°C (Amicon Ultra-4 30K) and by SEC (Sephadex G25 columns).

Physicochemical characterization

The average size of Pluronic unimers and cross-linked micelles was determined by dynamic light scattering (DLS). DLS was performed with an ALV/DLS/SLS-5020F experimental setup (ALV Laser Vertriebsgesellschaft mbH) with a He-Ne laser (22mW, $\lambda_0=632.8$ nm), a compact ALV/CGS-8 Goniometer system, and an ALV-7002 autocorrelator. The samples were analyzed in cylindrical quartz cuvettes at 90 degree angle in a controlled temperature bath at 15, 25 or 37°C and a concentration of 2.5% w/w. The normalized autocorrelation functions of the scattered intensity were analyzed using the CONTIN algorithm.

The superficial charge of the stabilized micelles was measured through zeta potential (mV) determination (Zetasizer Nano ZS, Malvern Instruments, UK).

Polymer conjugation efficiency and radiolabeling of Pluronic nanocarriers with ¹¹¹In

The conjugation efficiency of p-SCN-Bn-DTPA was determined by thin layer chromatography (TLC) of radiolabeled copolymers. The nanocarriers F127-DTPA and P94-DTPA diluted in PBS were labelled with 1 MBq of ¹¹¹InCl₃ and incubated for 30 min at room temperature. TLC was performed in Aluminum sheets of silica gel 60 using a sodium acetate buffer (0.1 M, pH 5.8) as the eluent (Rf Pluronic-DTPA-¹¹¹In=0, Rf free ¹¹¹In=0, Rf p-SCN-Bn-DTPA-¹¹¹In=0.5-1 and Rf DTPA-¹¹¹In=1). Purification from unreacted p-SCN-Bn-DTPA was performed by size exclusion chromatography (SEC) using prepacked Sephadex G25 columns and MilliQ water as the eluent.

F127-DTPA, SPM-F127-DTPA, P94-DTPA and SPM-P94-DTPA were prepared in 1X PBS buffer and 75 MBq of ¹¹¹InCl₃ were added to each sample at room temperature and incubated for 30 minutes. Radiochemical purity was evaluated by TLC using EDTA:NH₄Ac (1:1) (v:v) (0.1 M, pH 5.5) (Rf Pluronic-DTPA-¹¹¹In=0, Rf free ¹¹¹In=1, Rf p-SCN-Bn-DTPA-¹¹¹In=0.5-1 and Rf DTPA-¹¹¹In=1).

Samples with labelling efficiency higher than 95% were used without further purification. Samples with a lower coupling efficiency were further purified by addition of free DTPA to the labelling mixtures and by subsequent elution through a prepacked Sephadex G25 column using 1X PBS as the eluent. The purification efficiency for the eluted fractions was then evaluated by TLC.

In vitro radiostability in mouse serum and PBS

Radiostability of F127-DTPA-¹¹¹In, P94-DTPA-¹¹¹In, SPM-F127-DTPA-¹¹¹In and SPM-P94-DTPA-¹¹¹In was measured *in vitro* by incubation of 50 μL of radiolabeled samples with 350 μL of PBS or mouse serum at 37°C for 72 h. At various time points, 5 μL aliquots of the solutions were spotted in the bottom of TLC strips and developed in the EDTA:NH₄Ac (1:1) (v:v) (0.1 M, pH 5.5) eluent to evaluate the dissociation of ¹¹¹In from the samples. In this system, it is possible to assess transchelation to serum proteins as Rf Pluronic-DTPA-¹¹¹In=0.0, Rf Proteins-¹¹¹In=0.5 and Rf free ¹¹¹In=1.0. Free ¹¹¹In and p-SCN-Bn-DTPA-¹¹¹In were used as controls.

Animal handling

Animal experiments were performed with A/J mice according to protocols approved by the Animal Ethical Committee of the UMC Utrecht and in accordance with Dutch Law on Animal experimentation.

Eight mice were divided into four study groups and assigned for imaging with F127-DTPA-¹¹¹In, SPM-F127-DTPA-¹¹¹In, P94-DTPA-¹¹¹In and SPM-P94-DTPA-¹¹¹In. All animals were anesthetized with isoflurane and injected with the radioactive compounds in the tail vein. Average injected activities were 3.6 MBq and 0.014 g/kg of compound.

SPECT/CT imaging and data analyzing

Animals were imaged in U-SPECT⁺/CT scanner (MILabs, The Netherlands). This system is equipped with a three stationary scintillator detectors that are arranged in triangular setup and an integrated X-ray micro-CT scanner.

Total body SPECT/CT scans of 30 min were acquired at 0 (immediately after injection), 24 and 48 hours post-injection (p.i.). After the end of the 48 hours p.i. total body scans, an additional 30 min scan was performed focusing on the abdominal area to acquire information on late-stage biodistribution in the spleen and liver.

The SPECT scans were acquired in list-mode data format with use of 2.0 mm mouse pinhole collimator [Ivashchenko *et al.* 2015]. After this, SPECT image reconstructions were carried out with a pixel-based order-subset expectation maximization (POSEM) [Branderhorst *et al.* 2010] algorithm that included resolution recovery and compensation for distance-dependent pinhole sensitivity [van der Have *et al.* 2008]. All reconstructions were performed with use of 4 subsets, 12 iterations and an isotropic 0.4-mm-voxel grid. Triple-energy-window based Compton scatter correction according to King *et al.* 2004. with 4% background windows and a 20% photopeak energy window centered at 171 keV was performed. Effects of gamma-attenuation in the animal and bed were corrected for using CT data, after which absolute quantification of SPECT images was enabled using a scaling factor obtained from scanning a small ¹¹¹In source with known activity [Wu *et al.* 2010].

For visual representation in the manuscript, reconstructed volumes were filtered with 1.2 mm full width at half maximum (FWHM) 3D Gaussian filter. Time-activity curves (TACs) derived from dynamic SPECT scan were generated from manually drawn region-of-interests (ROI),

using decay-corrected but otherwise unprocessed images, reconstructed as a dynamic frame sequence.

To calculate the uptake of radiolabeled compound in the organs of interest, the registered to CT and quantitative 3D SPECT images were analyzed using PMOD 3.6 biomedical image analyzing software (PMOD, Zurich, Switzerland). A 3D ROI was manually drawn to encompass the radioactivity uptake in the organ. Separate ROI's were drawn for the radioactivity uptakes in the heart, liver, spleen, kidneys, brain and lungs. The uptake was expressed as % injected dose (%ID) per mL of tissue volume (%ID/mL).

All quantification data was reported as mean \pm standard deviation within one study group. Correlations between the biodistribution of nanocarriers with different PEO block length and aggregation state were calculated using Pearson's correlation coefficient. All other statistic comparisons were made using the Student's t test. MATLAB R2013b software was used for all statistic evaluations.

Results

Synthesis of DTPA-functionalized Pluronic nanocarriers

Table 1 summarizes the characteristics of the employed Pluronics as determined by ¹H-NMR and TLC. While the PPO block has practically the same length in both copolymers, the PEO length is four times larger for the Pluronic F127. Pluronic unimers were first end-functionalized with the hydrophilic chelator DTPA according to scheme available in the supplementary information (Scheme S1). In the ¹H-NMR spectrum of Pluronic-CDI (Figure 1), peaks from the imidazole moiety protons ($\delta=8.15$ ppm, $\delta=7.44$ ppm and $\delta=7.06$ ppm) and from the ethylene oxide group adjacent to the imidazole carbonate group ($\delta=4.55$ ppm) can be visualized. The protons of the -CH₂NH₂ methylene groups of the amine modified Pluronics were detected by the appearance of a triplet at $\delta=2.82$ ppm for both Pluronics. FT-IR analysis of the copolymers and of the intermediate CDI-activated or amine-modified Pluronics are available in the supplementary information (Figure S1).

The modified chelator p-SCN-Bn-DTPA was conjugated to the amine terminated block copolymers (P94-NH₂ and F127-NH₂) by reaction of the primary amine with the reactive chelator isothiocyanate group to form a stable thiourea bond according to Figure S1. The corresponding functionalization degrees are presented in Table 1.

Table 1. Characteristics of PEO-PPO-PEO copolymers employed and functionalization degrees of modified copolymers.

Chemical Formula ^a	Pluronic F127 PEO ₉₆ -PPO ₅₆ -PEO ₉₆	Pluronic P94 PEO ₂₆ -PPO ₄₈ -PEO ₂₆
Mn (Da) ^a	11700	5000
Mn PEO blocks (Da) ^a	8500	2200
Mn PPO block (Da) ^a	3200	2800
CDI activation efficiency ^a	90%	64%
NH ₂ modification efficiency ^a	93%	79%
p-SCN-Bn-DTPA conjugation efficiency ^b	82%	81%

^a Determined by ¹H-NMR

^b Determined by TLC and gamma-counter

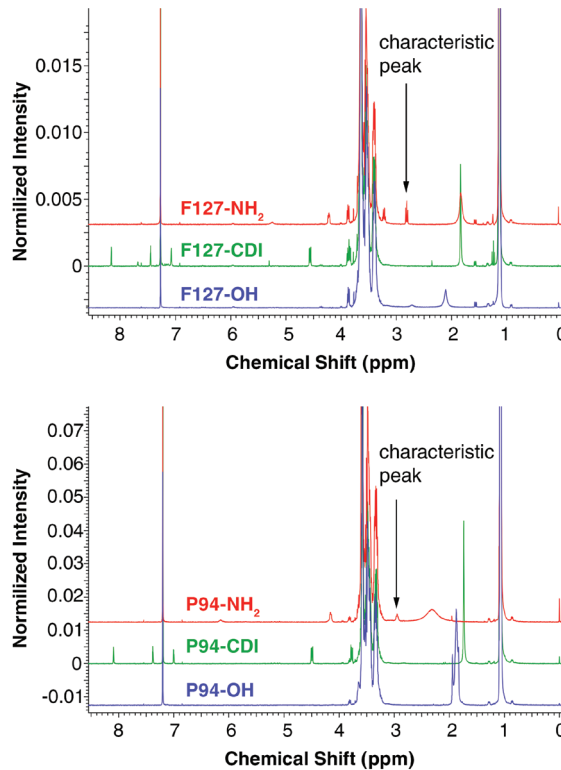


Figure 1. ¹H-NMR spectrums of Pluronic copolymers and intermediate synthesis products.

Physicochemical characterization of Pluronic nanocarriers

Pluronic triblock copolymers in their molecular form (unimers) and supramolecular assemblies (cross-linked micelles) with different molecular weight and PEO length were used (Figure 2). The hydrodynamic size of the nanocarriers was determined below their cmT (15°C) (Table 2). The unimers are expected to be highly compact possibly with the PEO block forming a tight shell around the non-hydrated PPO core. Due to the larger length of the PEO block, Pluronic F127 exhibits a slightly larger hydrodynamic diameter than Pluronic P94.

To avoid the disassembly of Pluronic micelles *in vivo* [Talelli *et al.* 2012], their spherical structure was stabilized by UV-polymerization of pentaerythrol tetraacrylate (PETA) in the micellar core at 60°C (5). Stabilized Polymeric Micelles (SPM) of Pluronic P94 and F127 (SPM-P94 and SPM-F127 respectively) were then obtained. Light scattering characterization confirmed they were monodisperse systems that do not disassemble below the cmT (15°C), and present an average hydrodynamic diameter of 30-35 nm and a slightly negative zeta potential in relation to the neutral unimers (Table 2). This small decrease of the absolute value of the zeta potential (below -15 mV) should have a minor or even negligible influence on the biodistribution of the nanomaterials [Xiao *et al.* 2011, He *et al.* 2010]. Moreover, the size of the cross-linked carriers did not vary significantly at higher temperatures (Table S1). Detailed physicochemical characterization of the stabilized micelles, including cryo-TEM analysis, is available in Arranja *et al.* 2014.

Radiolabelling efficiency and purity

Radiolabeling of nanocarriers was performed under standard labelling conditions for DTPA and ¹¹¹In (PBS and room temperature). The radiolabeling efficiencies were determined by TLC coupled to gamma-scintillation and are presented in Table 3. The DTPA modified copolymers (P94-DTPA and F127-DTPA) presented high labelling efficiencies (>95%), while radiolabeling of the stabilized micelles (SPM-F127-DTPA and SPM-P94-DTPA) was less efficient (~50%). Purification by size exclusion chromatography of the supramolecular carriers allowed us to obtain efficiencies of nearly 100%, which was suitable to perform *in vivo* SPECT studies.

Radiolabeling stability of ¹¹¹In in mouse serum and PBS

The stability of the DTPA-¹¹¹In complex in all the nanocarriers was evaluated at 37°C in both mouse serum (Figure 3, A) and PBS (Figure 3, B). The comparison between the two solvents allowed to assess the role of chelating proteins present in the serum (e.g., transferrin) on the complex stability. The latter was quantified by using TLC and gamma-scintillation.

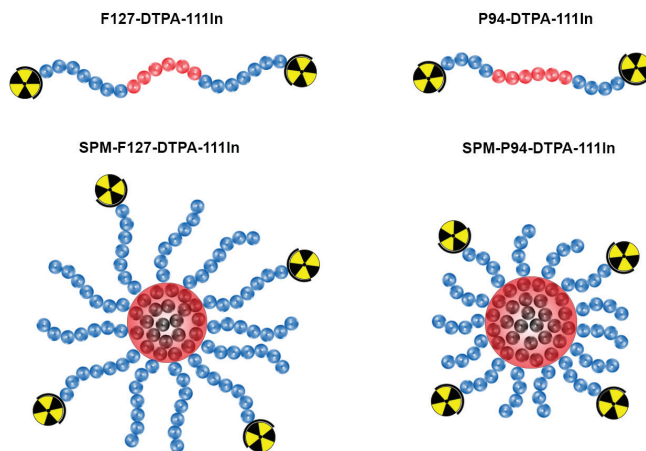


Figure 2. Molecular (F127-DTPA-¹¹¹In and P94-DTPA-¹¹¹In) and supramolecular (SPM-F127-DTPA-¹¹¹In and SPM-P94-DTPA-¹¹¹In) Pluronic nanocarriers investigated *in vivo*.

Table 2. Hydrodynamic diameter and zeta potential of Pluronic unimers (F127 and P94) and Stabilized Polymeric Micelles (SPM-F127 and SPM-P94).

Compound	D _{H, 15 °C} (nm)	ζ (mV)
F127	5.8 ± 0.4	Neutral ^a
SPM-F127	32.4 ± 2.4	- 13.3 ± 1.3
P94	4.2 ± 0.4	Neutral ^a
SPM-P94	29.2 ± 1.0	- 9.9 ± 0.3

^a Not measurable by equipment

After 72h, the loss of ¹¹¹In remained low, about 5-7% for F127-DTPA-¹¹¹In, SPM-F127-DTPA-¹¹¹In and P94-DTPA-¹¹¹In. However, the cross-linked micelles with the shorter PEO corona (SPM-P94-DTPA) were less stable revealing a 24% ¹¹¹In loss after 2h in the presence of mouse serum. Complex instability was also observed in PBS but at a slower rate.

It is known that complexes of DTPA-¹¹¹In present some *in vivo* instability and can dissociate at a rate of 5-9% loss per day for low molecular weight compounds [Lub-de Hoge *et al.* 2004, Hnatowich *et al.* 1986, Patil *et al.* 2011], and up to 20% loss in 24h for, e.g., polymersomes with the DTPA-¹¹¹In complexes on their surface [Brinkhuis *et al.* 2012]. In comparison, the present nanocarriers displayed a better overall labelling stability, without significant ¹¹¹In loss in the presence. Only SPM-P94-DTPA-¹¹¹In showed both higher ¹¹¹In loss and sensitivity to the medium. The fact that we observed loss of ¹¹¹In with SPM-P94-DTPA in PBS indicates that a fraction of the ¹¹¹In ions is most likely loosely bound to the DTPA complexes on the surface of

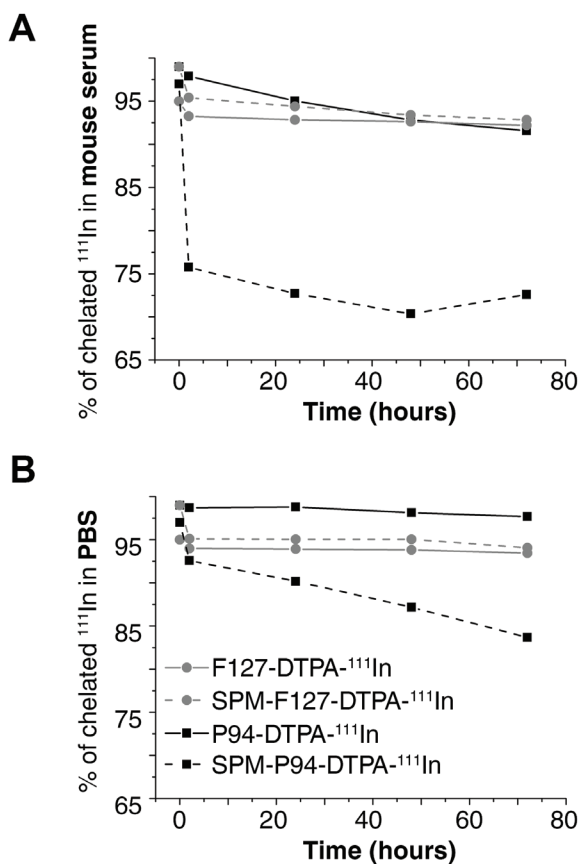


Figure 3. *In vitro* stability of ¹¹¹In radiolabelled Pluronic nanocarriers at 37°C after dilution in (A) mouse serum and in (B) PBS for 72h.

the cross-linked micelles. The dissociation kinetics of ¹¹¹In to the buffer occurs in a slow rate. However, in the presence of competitive chelating proteins (mouse serum), the ¹¹¹In loss occurs at a much higher rate and seems to stabilize after a few hours, which also suggests that only a finite fraction of the complexes formed at the surface are weakly bound.

SPECT/CT imaging of ¹¹¹In radiolabeled Pluronic nanocarriers

Figure 4 shows top view maximum intensity projections (MIPs) on total body SPECT/CT scans at various time points after administration of ¹¹¹In-labeled Pluronic nanocarriers, illustrating dynamic changes in compounds' distribution over imaging days. For better visualization, the activity in the bladder in 0h p.i. scans was manually cropped from the SPECT images. Dynamic SPECT images and animated images of rotating MIPs can be visualized in the supplementary

Table 4. Total body activity retention of Pluronic nanocarriers in the body of the animal 30 min, 24 and 48h post-injection (p.i.) time points, measured from the total body SPECT scans and expressed as % of the initially injected dose (ID).

Total body retention in % ID			
Compound	30 min p.i.	24 hours p.i.	48 hours p.i.
F127	81.2 ^a ±3.6 ^b	69.3±3.5	63.8±3.0
SPM-F127	80.7±0.4	70.4±1.9	61.4±1.2
P94	67.5±3.21	44.9±1.3	40.2±0.6
SPM-P94	61.9±3.3	31.6±3.1	31.1±3.0

^a Value do not includes ¹¹¹In activity in the bladder of the animal

^b Standard deviation within one study group of the animals

information (Figure S2, Videos S1-S4). The total activity remaining in the animal body (%ID), dynamic changes in activity accumulation in the liver (%ID) and the specific uptake in the main organs (liver, spleen, heart, kidney, lungs and brain) (%ID/mL) for all imaging time-points are summarized in Figure 4, Table 4 and Table S2-S3.

Our results show that all compounds have an initial renal clearance, which is higher for the P94-based carriers (~35% for P94 and ~19% for F127 compounds) (Table 4). At the same time, negligible activity was accumulated in the skeleton (Figure 4, A), what indicates minimal dissociation of ¹¹¹In in its ionic form the carriers after i.v. administration [Hosain *et al.* 1969, Adatepe *et al.* 1971]. However, a combination of relatively high and prolonged activity retention in the body of the animals with significant initial renal clearance rates (Table 4, Figure S2, Video S1-S4) indicates that we cannot totally exclude dissociation of ¹¹¹In-DTPA from the carriers.

Analyses of the late stage biodistribution (24 and 48h p.i.) indicate that clearance of the nanocarriers occurs mainly through the liver. High uptake in this organ was associated with a higher PEO block length (F127-DTPA-¹¹¹In and SPM-F127-DTPA-¹¹¹In) (Figure 4, Table S2-S3). Statistical analysis of the organs uptake showed that only the uptake in the liver and spleen was influenced by the PEO block length and aggregation state of the carriers. Tissue accumulation in the liver strongly correlated between unimers P94 and F127 ($R > 0.98$) and remained independent for other compounds. The retention in the liver at 48h was also influenced by the aggregation state of the copolymers. In particular, SPM-P94-DTPA-¹¹¹In were more retained (10.5±3.5 %ID/mL, 16.9±6.8 %ID) than the respective P94 unimers (6.2±1.9 %ID/mL, 10.3±0.7 %ID), while SPM-F127-DTPA-¹¹¹In were more efficiently excreted (12.2±3.6

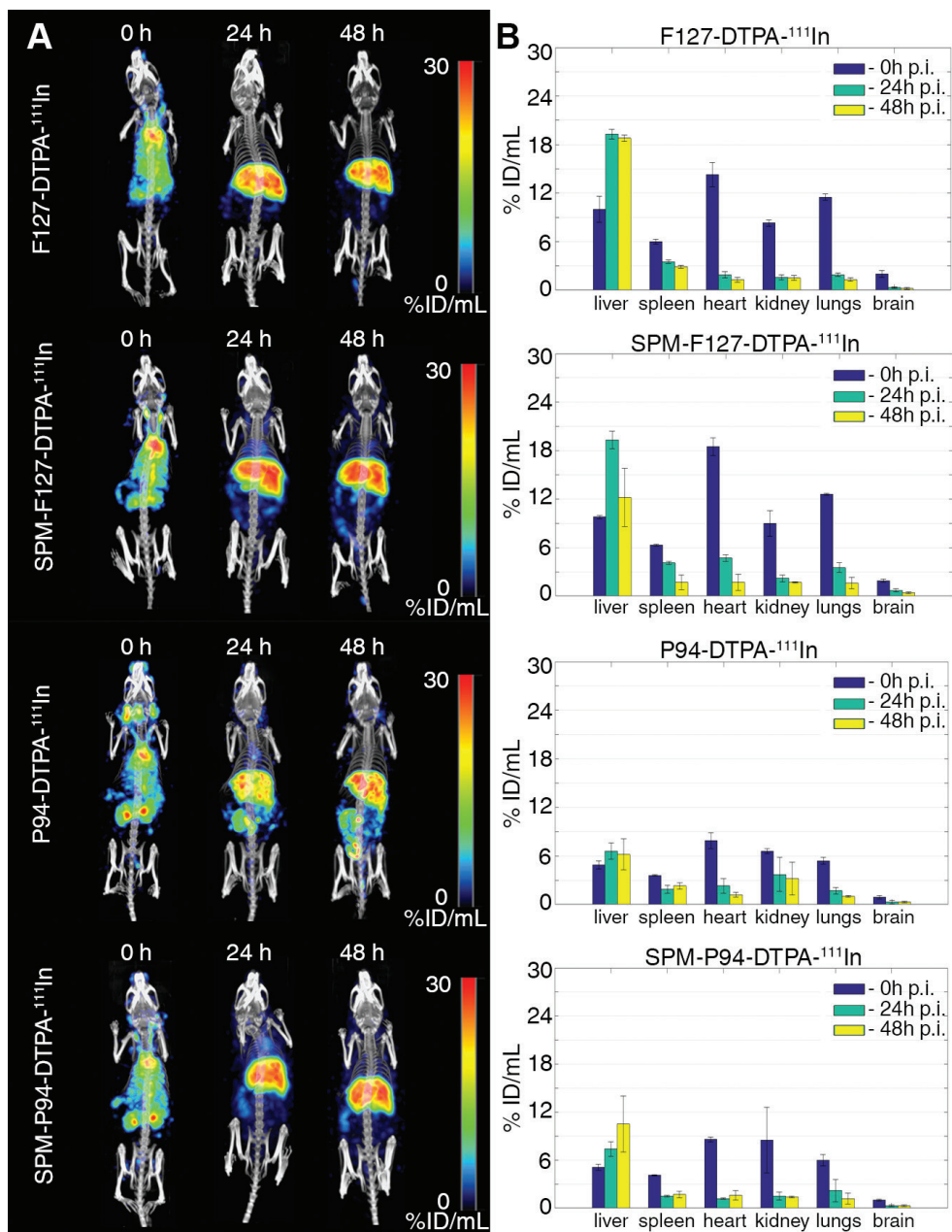


Figure 4. Maximal intensity projections of follow-up total body SPECT/CT scans, acquired at 0, 24 and 48 hours post injection of ¹¹¹In radiolabeled Pluronic nanocarriers.

%ID/mL, 22.1 ± 6.9 %ID) than the corresponding F127 unimers (18.8 ± 0.4 %ID/mL, 30.2 ± 2.4 %ID) (Figure 4, Table S2-S3).

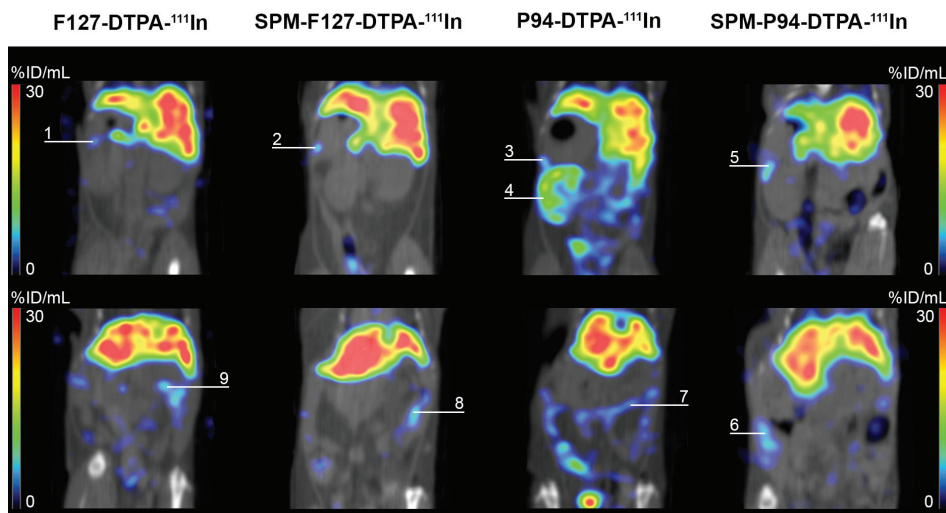


Figure 5. Abdominal area slices from the 48 hours post-injection total body SPECT/CT scans of mice injected with F127-DTPA-¹¹¹In, SPM-F127-DTPA-¹¹¹In, P94-DTPA-¹¹¹In and SPM-P94-DTPA-¹¹¹In, respectively. Images illustrate uptake in the spleen (1-3,5) and the intestines (6-9) for all compounds tested. At the same time, only P94-DTPA-¹¹¹In showed minor trapping of the compound in the renal cortex of the animal (4).

In the case of spleen uptake, statistical analysis revealed that only the stabilized micelles of the different Pluronic had uncorrelated tissue decomposition of ¹¹¹In-labeled compound.

Aspects of liver and hepatobiliary uptake of the compounds were further investigated through the abdominal area of the animals (Figure 5 and Figures S2-S5). Images show remaining spleen and intestinal uptake and generally high uniform liver uptake for all compounds. In the case of P94 unimers, the liver distribution is less uniform and we observed spreading of the radioactivity into the surrounding intestinal tissues (Figure 5).

Although Pluronic F127 is approved by the FDA for i.v. use in humans, its initial biodistribution has never been evaluated *in vivo*. To get insight on the early stage uptake dynamics, we performed a dynamic scan with F127-DTPA-¹¹¹In. The video of the dynamic SPECT scan is available in the Supplementary Video 5, and the corresponding TACs are presented in Figure 6. The uptake in main organs (heart, kidneys, liver, lungs and spleen) was almost immediate and distribution is achieved about 1 min after injection. The renal clearance started 1 min p.i., after which activity in the bladder gradually increased during the scan. The circulation of the compound in the systemic circulation was also clear throughout the scan due to high activity in the heart and arteries (see Video S5). Particularly in the lungs, the %ID/mL decreased from 25% to 11.5%

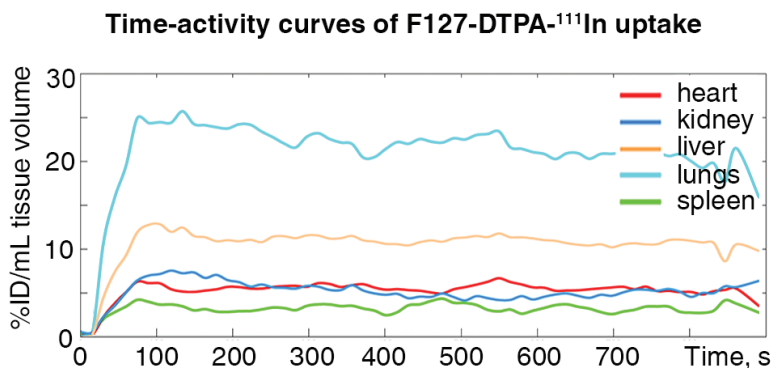


Figure 6. Time-activity curves of F127-DTPA-¹¹¹In show of the uptake during first 15 min after the activity injection. The graph shows %ID/mL uptake values for selected organs of interest in the mouse.

in 30 min (Figure 6, Table S2). Steady and effective washout of radioactivity from the organ in the first 24h p.i. (Figure 4, Figure 6, Table S2) indicates that there is no or minor trapping of the carriers in the lung tissue [Kutscher *et al.* 2010]. This high activity observed immediately after injection is associated with the high perfusion of this organ (8 mL/min) over the lower blood flow in other organs such as liver (1.8 mL/min), spleen (0.09 mL/min) and kidneys (1.3 mL/min) [Bertrand *et al.* 2012].

Discussion

After functionalization of the nanocarriers with the chelator DTPA and evaluation of the radiolabeling efficiency and stability, we studied their biodistribution as a function of PEO block length and aggregation state (unimers versus stabilized micelles). Samples were administered below the cmc, i.e. the final concentration in the blood pool was $\leq 0.025\%$ to assure comparison of molecular and supramolecular nanocarriers.

For the nanocarriers investigated in this work, a fraction of the radiolabeled compounds was rapidly excreted into the bladder after i.v. administration (Table 4). It is known that polymeric micelles and small nanoparticles with DTPA-¹¹¹In chelators can follow rapid loss of ¹¹¹In and/or DTPA-¹¹¹In complexes after i.v. administration [Lub-de Hoge *et al.* 2004, Hnatowich *et al.* 1986, Patil *et al.* 2011, Brinhuis *et al.* 2012]. In the first case, ¹¹¹In in the form of free ions will rapidly bind to blood protein transferrin [Hosain *et al.* 1969, Adatepe *et al.* 1971] which will result in rapid accumulation and long retention of indium in the bone marrow and the liver

[Kreyling *et al.* 2015, Ohtake *et al.* 2008], accompanied by relatively low clearance via renal filtration. Therefore, the observed initial renal clearance in our work is not related to dissociation of ^{111}In ions from the carriers. In the second case, the dissociation of DTPA- ^{111}In complexes will result in rapid excretion of the activity into the urine (biological half-life \sim 1 hour, 95 %ID excretion within 48h) [Harrington *et al.* 2000, Matsushima *et al.* 1977]. Relatively high and prolonged activity retention in the body of the animals (Table 4) indicates that dissociation of ^{111}In -DTPA complexes from the carriers should play only a minor role in the initial renal clearance of carriers studied in this work.

Although both Pluronic unimers are below the renal clearance threshold (30 kDa for linear PEG) [Yamaoka *et al.* 1994], their renal filtration rates indicate molecular weight dependency, with nearly 20 %ID of Pluronic F127 (12 kDa) and 30 %ID of Pluronic P94 (5 kDa) eliminated 30 min p.i.. The stabilized micelles (SPM-F127-DTPA- ^{111}In and SPM-P94-DTPA- ^{111}In) also presented initial renal clearance, which was faster for the SPM-P94-DTPA- ^{111}In . Considering the low bone uptake for all compounds studied, the fast clearance of SPM-P94-DTPA- ^{111}In (Table 4) should be predominantly attributed to the lower stability of the DTPA- ^{111}In complexes in the presence of serum proteins (Figure 3, A).

Overall, the organ with the highest uptake of the radioactive compounds was the liver (Figure 4, Table S2). This accumulation mainly occurs through internalization by the hepatocytes and the Kupffer cells [Bertrand *et al.* 2012]. The passage of the nanocarriers through the liver endothelial fenestrations leads to their metabolism by the hepatocytes and elimination into the bile and intestinal tract. We have observed at late time points (24 and 48h) activity in the intestines for all compounds (Figure 5), showing that the nanocarriers were excreted via the hepatobiliary system. Late time-points SPECT of P94 unimers showed spreading of the compound into the surrounding tissues of the gastrointestinal tract (Figure 5), which can be explained by their small size (Table 2) and diffusion through endothelial junctions. The uptake by Kupffer cells occurs as a result from opsonization by serum proteins in the systemic circulation. To avoid opsonization, the surface of the nanomaterials can be modulated using PEO, which also depends on the chain length and PEO surface density [Klibanov *et al.* 1990]. Corona chains in Pluronic micelles have a “mushroom” conformation [Bhattacharjee *et al.* 2013] associated with a lower density of PEO chains and larger fluctuations of the local PEO concentration, which can facilitate the adsorption of plasma proteins onto the hydrophobic core. Pluronic micelles can then be recognized by the Kupffer cells. The two-fold increase in the liver uptake at 24h for the F127, SPM-F127 and SPM-P94 (Table S2) shows that clearance by

the liver was delayed. In the case of P94 unimers, the uptake in the liver did not increase significantly during the 48 hours suggesting that the elimination of P94 unimers occurs mainly through renal filtration. In fact, the accumulation of P94-DTPA-¹¹¹In in the kidney was consistently higher (Figure 4, Table S2). In conclusion, we observed that the PEO block length affects the renal clearance and initial liver uptake of the compounds, whereas the aggregation state influences the retention in the liver at late-stages (48h).

The spleen uptake of all nanocarriers studied was low and decreased overtime indicating circulation without retention in the spleen sinusoidal sieve (Figure 4, Table S2). Nanocarriers with high rigidity, elongated or irregular shapes and/or large size (>70-90 nm) present generally high retention in the spleen [Brinkhuis *et al.* 2012, Bertrand *et al.* 2012]. The ability of our nanocarriers to surpass the spleen clearance mechanisms suggests that they should achieve good biocompatibility and should not trigger immunogenic reactions.

None of the carriers studied were retained in the lungs (Table S2) due to their small size and flexibility [Bertrand *et al.* 2012]. Since Pluronics are not biodegradable [Grindel *et al.* 2002], the observed elimination pathways (renal and hepatic clearance) contribute to the biocompatibility of these systems.

Conclusions

We developed a new strategy to compare the biodistribution of Pluronic-based nanocarriers with different PEO block length and aggregation state. This approach eliminates the recurrent limitation associated with the dynamic nature of copolymer micelles and allows us to use similar concentrations of both types of nanocarriers.

Our results show that varying the PEO block length and aggregation state of the copolymers (unimers versus micelles), different renal and liver clearances are obtained. Outcomes of this work can be beneficial for a more rational development of Pluronic-based nanocarriers and for the future of EPR-based cancer therapies.

Supplemented Materials and Methods

Materials

Pluronic P94 and F127 were supplied by BASF Ltd. Dimethyl sulfoxide (DMSO), sodium bicarbonate, pentaerythrol tetraacrylate (PETA), 1,1-carbodiimidazole (CDI), ethylenediamine, trichloroacetyl isocyanate, mouse serum, toluene and acetone were purchased from Sigma-Aldrich. Amicon Ultra-4 30K centrifugal filter units and TLC Aluminum sheets of silica gel 60 were obtained from Millipore. Phosphate buffered solution (1X PBS, without CaCl_2 and MgCl_2 , pH 7.4) was obtained from Life Technologies. Tri-sodium citrate dihydrate and ethylenediaminetetraacetic acid dipotassium salt dihydrate (EDTA) were obtained from Fluka. Diethylenetriaminepentaacetic acid (DTPA) was purchased from Merck, and citric acid monohydrate and ammonium acetate from J. T. Baker. Tetrahydrofuran (THF) was obtained from Acros and diethyl ether from Chem-Lab. Dialysis membranes with MWCO of 1 kDa and 3.5 kDa were obtained from Spectrum Laboratories and Roth respectively. The modified chelator S-2-(4-Isothiocyanatobenzyl)-diethylenetriamine pentaacetic acid (p-SCN-Bn-DTPA) was purchased from Macrocyclics. Prepacked Sephadex G25 columns were supplied by GE Healthcare Life Sciences. The radioactive isotope ^{111}In -chloride was provided by IDB Holland. All the reagents were used as received unless stated otherwise.

Purification of commercial Pluronic P94 and F127

Pluronic P94 was purified by dialysis using regenerated cellulose membranes (MWCO 3.5 kDa). A concentrated aqueous solution of the P94 copolymer (10 wt%) was prepared and dialyzed against distilled water for 7 days. After purification, the water in the polymer solution was removed by vacuum drying. Prior to reactions, Pluronic P94 and F127 were purified using Dean Stark distillation in toluene.

Preparation of CDI-activated and amine-terminated Pluronic

The purified Pluronic (P94 or F127) was dissolved in dry THF (8 mM) and added dropwise during one hour in a 1:10 molar ratio to a solution of CDI in dry THF (0.08 mM) at room temperature under argon atmosphere. The reaction mixture was stirred overnight. The solution was concentrated to 2 mL under vacuum and added to 30 mL of diethyl ether. The precipitate was isolated via filtration and redissolved in THF, followed by precipitation in an excess amount of diethyl ether. This process was repeated three times to remove unreacted CDI. The CDI-activated Pluronic (Pluronic-CDI) were obtained as white powders after drying under vacuum at room temperature.

For the amine modification, the Pluronic-CDI was dissolved in dry THF (4 mM), and added dropwise to ethylenediamine (1:394 ratio) at room temperature during one hour. The mixture was left to react overnight. The unreacted ethylenediamine was removed by vacuum distillation and the residue was dissolved in water and dialyzed against water using a membrane with a 1 kDa molecular weight cut-off to yield the amine-terminated triblock copolymers (Pluronic-NH₂) as white powders after freeze-drying.

DTPA conjugation efficiency to Pluronic unimers

TLC was done using a stationary phase of silica gel 60 and a mobile phase of sodium acetate buffer (0.1 M, pH 5.8). A spot (5 μ L) with the radiolabeled samples was placed in the bottom of a TLC strip (1 \times 10 cm) and developed in the same buffer. After elution, the TLC strips were imaged with a Storage Phosphor system (Cyclone, Packard), which enabled an appropriate sectioning of the TLC strip for the quantitative analysis through gamma-scintillation counting (2480 Wizard2 Automatic Gamma Counter, Perkin Elmer). The DTPA conjugation efficiency was calculated based upon the relative amount of ¹¹¹In attached to F127-DTPA or P94-DTPA, and the amount of ¹¹¹In bound to free unconjugated p-SCN-Bn-DTPA, which are well resolved in a sodium acetate buffer (Rf Pluronic-DTPA-¹¹¹In=0.0; Rf p-SCN-Bn-DTPA-¹¹¹In=0.5).

Physicochemical characterization

DLS was performed with an ALV/DLS/SLS-5020F experimental setup (ALV Laser Vertriebsgesellschaft mbH) with a He-Ne laser (22mW, λ_0 =632.8 nm), a compact ALV/CGS-8 Goniometer system, and an ALV-7002 autocorrelator. The samples were analyzed in cylindrical quartz cuvettes at 90 degree angle in a controlled temperature bath at 15°C and a concentration of 2.5% w/w. The normalized autocorrelation functions of the scattered intensity were analyzed using the CONTIN algorithm.

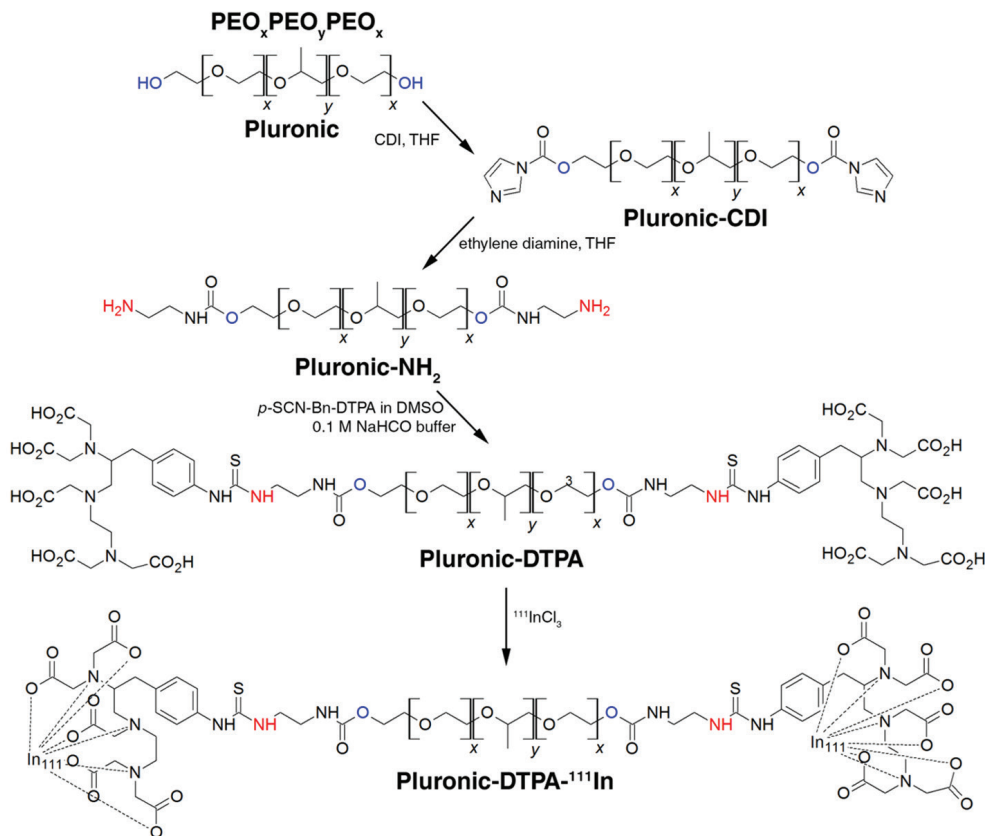
Radiolabeling of Pluronic nanocarriers with ¹¹¹In and purification

The EDTA:NH₄Ac (1:1) (v:v) (0.1 M, pH 5.5) TLC system allows the resolution of ¹¹¹In attached to Pluronic unimers or cross-linked micelles, to free p-SCN-Bn-DTPA-¹¹¹In, and free uncomplexed ¹¹¹In (Rf Pluronic-DTPA-¹¹¹In=0.0; Rf p-SCN-Bn-DTPA-¹¹¹In=0.5; Rf free ¹¹¹In=1.0). This stems from the presence of EDTA in the eluent which complexes to free Indium (log K(EDTA-¹¹¹In) \approx 25, log K(DTPA-¹¹¹In) \approx 30).

Supporting Videos

<http://pubs.acs.org/doi/suppl/10.1021/acs.molpharmaceut.5b00958>

Supplemented Materials and Methods



Scheme S1. Synthesis of DTPA-modified Pluronic unimers and radiolabelling with ¹¹¹In.

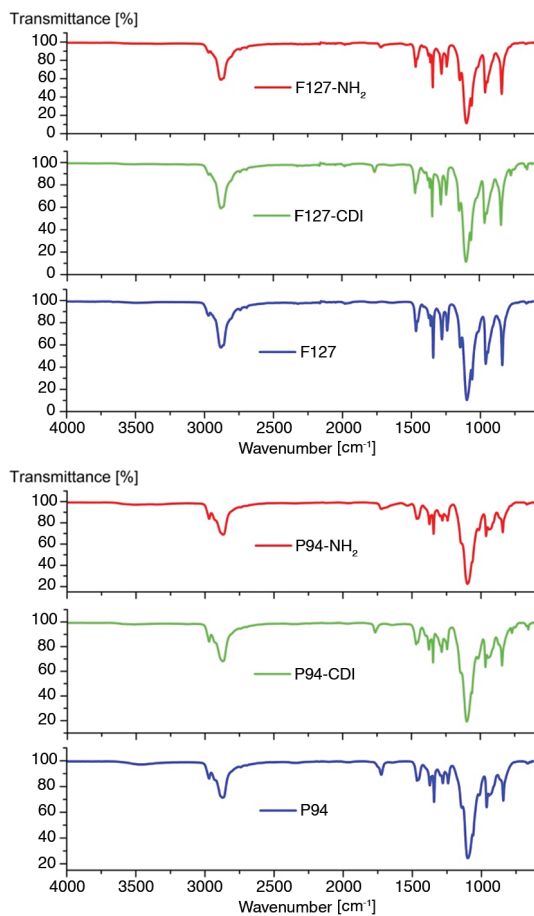


Figure S1. FT-IR spectrums of copolymers (top) F127 and (bottom) P94 and intermediate synthesis products. The band at 1762 cm^{-1} on the CDI activated Pluronic qualitatively confirmed the presence of carbonyl groups in the polymer chain. The amine modification was confirmed by the presence of carbonyl groups (band at 1718 cm^{-1}).

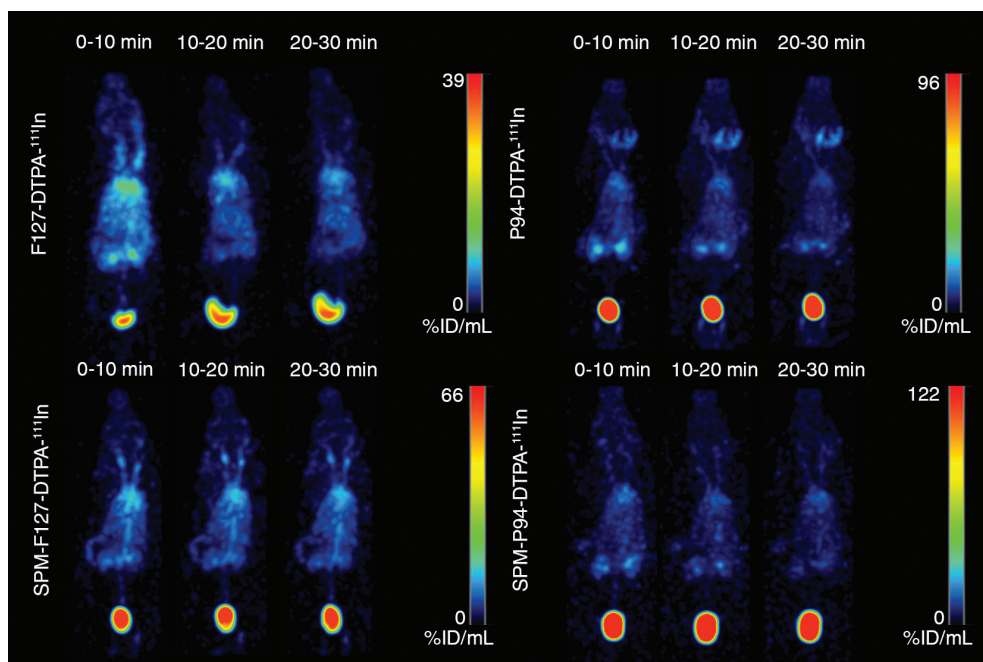


Figure S2. The top view MIPs of dynamic total body SPECT/CT scan, acquired at 0 hours post injection of ^{111}In -radiolabeled nanocarriers. Images illustrate the early stage dynamics of the carriers.

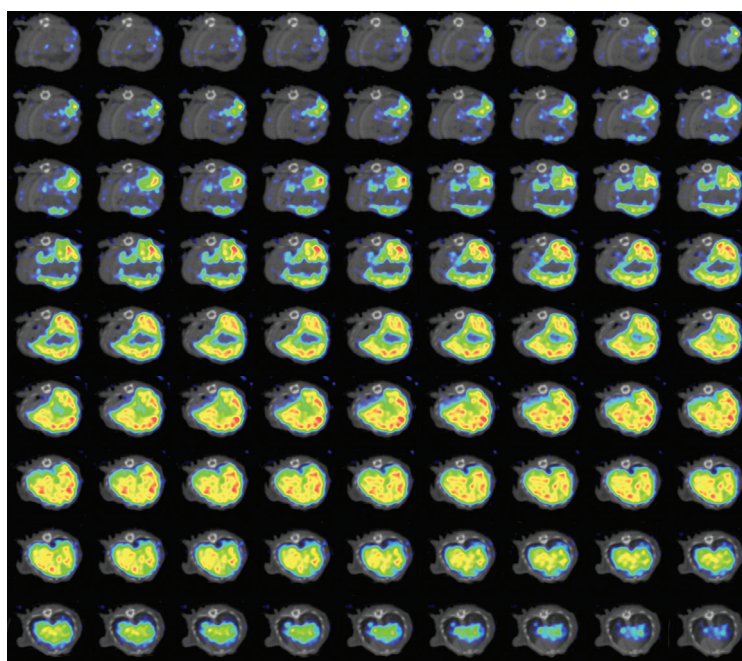


Figure S3 depicts axial slices (thickness 0.4 mm) of late-stage mouse F127-DTPA- ^{111}In SPECT/CT scan with focusing on abdominal area of the animal.

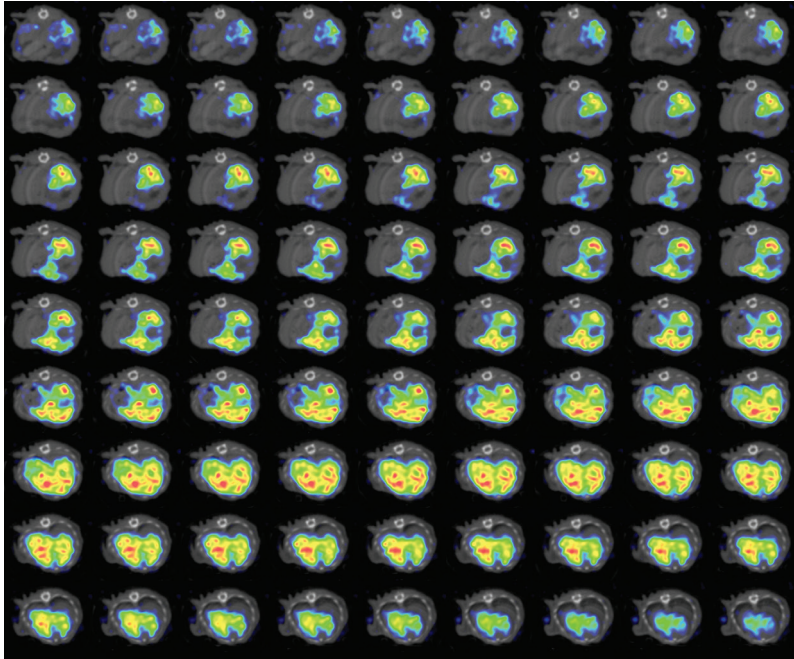


Figure S4 depicts axial slices (thickness 0.4 mm) of late-stage mouse SPM-F127-DTPA-¹¹¹In SPECT/CT scan with focusing on abdominal area of the animal.

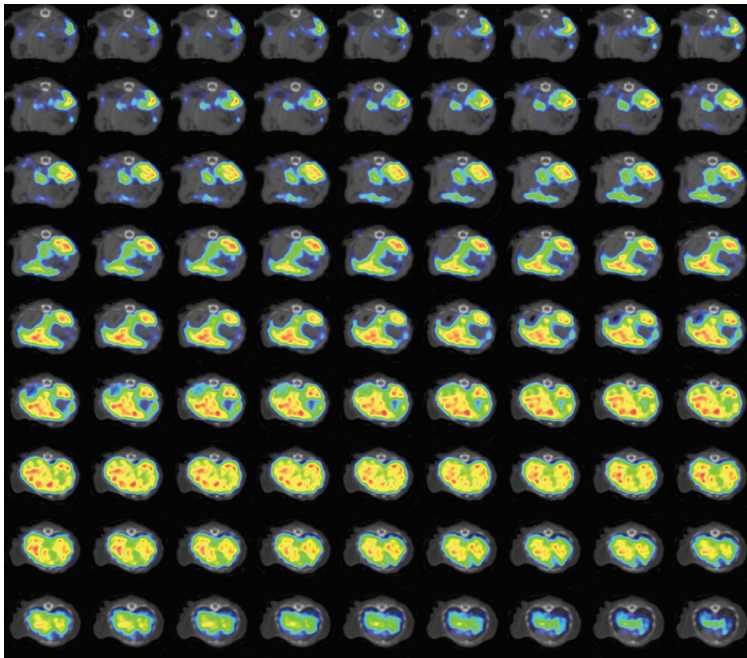


Figure S5 depicts axial slices (thickness 0.4 mm) of late-stage mouse P94-DTPA-¹¹¹In SPECT/CT scan with focusing on abdominal area of the animal.

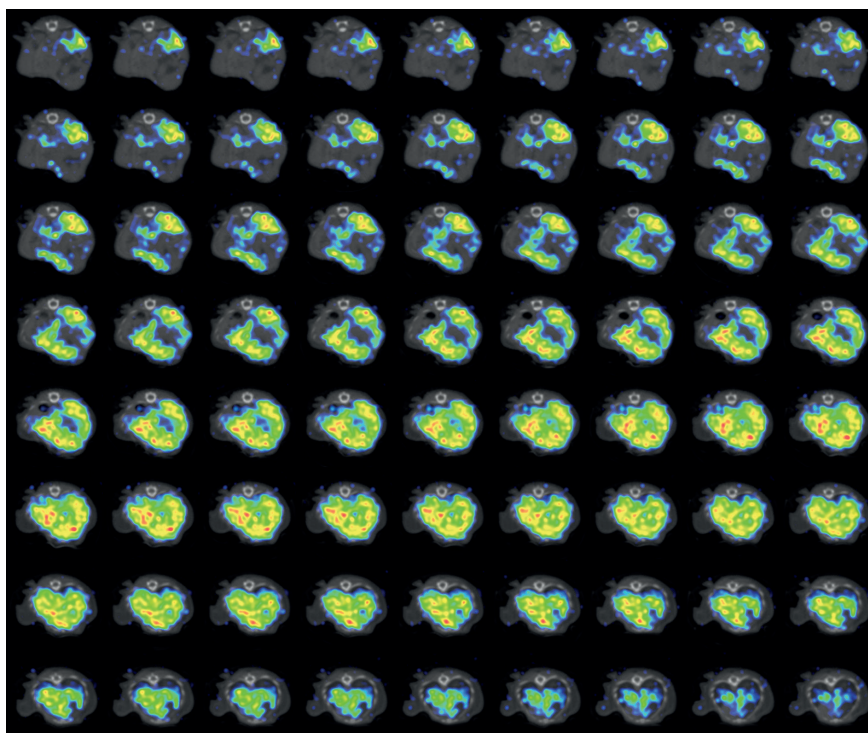


Figure S6 depicts axial slices (thickness 0.4 mm) of late-stage mouse SPM-P94-DTPA-¹¹¹In SPECT/CT scan with focusing on abdominal area of the animal.

Table S1. Hydrodynamic diameter (D_H) of Stabilized Polymeric Micelles (SPM-F127 and SPM-P94) as a function of solution temperature.

Compound	$D_{H,15^\circ\text{C}}$ (nm)	$D_{H,25^\circ\text{C}}$ (nm)	$D_{H,35^\circ\text{C}}$ (nm)
SPM-F127	32.4 ± 2.4	37.6 ± 1.4	35.8 ± 0.4
SPM-P94	29.2 ± 1.0	26.2 ± 1.8	27.6 ± 1.8

Table S2. Quantified uptake of Pluronic nanocarriers in the liver of the animals at 0, 24 and 48 hours p.i., expressed as %ID of the initially injected activity.

Uptake in the organ of interest (%ID/mL)				
Organ	Compound	30 min p.i.	24h p.i.	48h p.i.
Liver	F127-DTPA	11.2±1.7 ^a	38.3±1.5	30.2±2.4
	SPM-F127-DTPA	10.4±0.8	34.7±1.3	22.1±6.9
	P94-DTPA	6.9±0.7	11.6±1.5	10.3±0.7
	SPM-P94-DTPA	5.6±0.8	13.4±1.1	16.9±6.8

^a Standard deviation within one study group of the animals

Table S3. *In vivo* biodistribution of Pluronic nanocarriers in multiple organs of the animals, extracted from quantified total body SPECT/CT scans at 30 min, 24 and 48 hours p.i. and expressed as %ID/mL of tissue volume.

Uptake in the organ of interest (%ID/mL)				
Organ	Compound	30 min p.i.	24h p.i.	48h p.i.
Liver	F127-DTPA	10.0±1.6 ^a	19.3±0.6	18.8±0.4
	SPM-F127-DTPA	9.8±0.2	19.3±1.1	12.2±3.6
	P94-DTPA	4.9±0.5	6.6±1.0	6.2±1.9
	SPM-P94-DTPA	5.1±0.4	7.4±0.9	10.5±3.5
Spleen	F127-DTPA	6.0±0.3	3.5±0.2	2.9±0.2
	SPM-F127-DTPA	6.3±0.1	4.1±0.2	1.7±0.9
	P94-DTPA	3.6±0.1	1.9±0.5	2.3±0.4
	SPM-P94-DTPA	4.1±0.1	1.5±0.1	1.7±0.4
Heart	F127-DTPA	14.3±1.5	1.9±0.4	1.3±0.3
	SPM-F127-DTPA	18.5±1.1	4.7±0.4	1.7±1.0
	P94-DTPA	7.9±1.0	2.3±0.9	1.2±0.3
	SPM-P94-DTPA	8.6±0.3	1.2±0.1	1.6±0.6
Kidney	F127-DTPA	8.3±0.4	1.6±0.3	1.5±0.3
	SPM-F127-DTPA	9.0±1.6	2.2±0.4	1.7±0.1
	P94-DTPA	6.6±0.3	3.7±2.1	3.2±2.0
	SPM-P94-DTPA	8.5±4.1	1.5±0.5	1.4±0.1
Lungs	F127-DTPA	11.5±0.4	1.9±0.2	1.3±0.2
	SPM-F127-DTPA	12.6±0.1	3.5±0.6	1.6±0.7
	P94-DTPA	5.4±0.4	1.7±0.4	1.0±0.1
	SPM-P94-DTPA	6.0±0.7	2.2±1.4	1.2±0.7
Brain	F127-DTPA	2.0±0.4	0.3±0.1	0.2±0.1
	SPM-F127-DTPA	1.9±0.2	0.7±0.2	0.4±0.1
	P94-DTPA	0.9±0.2	0.3±0.2	0.3±0.1
	SPM-P94-DTPA	1.0±0.1	0.3±0.1	0.3±0.1

^a Standard deviation within one study group of the animals

Chapter 6

Effect of polymer micelle morphology on *in vivo* biodistribution probed by high-sensitivity SPECT

This chapter is based on the publication:

Jennings L*, **Ivashchenko O***, Marsman IJC, *et al.* *In vivo* Biodistribution of stable spherical and filamentous micelles probed by high-sensitivity SPECT. *Biomater Sci.* 2016; 4(8):1201-11.

**equal contribution*

-This publication has featured as the inside front cover of the journal (Biomater Sci.).

Abstract

Understanding how nanoparticle properties such as size, morphology and rigidity influence their circulation time and biodistribution is essential for the development of nanomedicine therapies. Herein we assess the influence of morphology on cellular internalization, *in vivo* biodistribution and circulation time of nanocarriers using polystyrene-b-poly(ethylene oxide) micelles of spherical or elongated morphology. The glassy nature of polystyrene guarantees the morphological stability of the carriers *in vivo* and by encapsulating Indium-111 in their core, an assessment of the longitudinal *in vivo* biodistribution of the particles in healthy mice is performed with single photon emission computed tomography imaging. Our results show prolonged blood circulation, longer than 24 hours, for all micelle morphologies studied. Dynamics of micelle accumulation in the liver and other organs of the reticuloendothelial system show a size-dependent nature and late stage liver clearance is observed for the elongated morphology. Apparent contradictions between recent similar studies can be resolved by considering the effects of flexibility and degradation of the elongated micelles on their circulation time and biodistribution.

Background

Properties such as polymeric architecture, surface charge or size are known to be some of the main factors determining the behavior of nanoparticles both *in vitro* and *in vivo*. This knowledge is derived from a plethora of studies that have been performed using particles of spherical morphology. This is partially due to the simplicity of preparation and characterization of spherical particles as opposed to elongated ones. Indeed, the latter include all the complexities of the former while adding extra physical properties such as length, aspect ratio and flexibility, resulting in an intrinsically more complex system to develop, characterize and interpret. Therefore, the influence of morphology on the *in vivo* behavior of nanocarriers is, comparably, unexplored.

Nonetheless, in recent years theoretical and experimental studies have suggested the advantages of using oblate or high aspect ratio particles both *in vitro* and *in vivo*. Decuzzi *et al.* 2006 have shown through simulation that there exist an optimal aspect ratio for particles that maximizes adhesive strength to membranes. Mitragotri *et al.* 2005 have shown that the morphology of polystyrene microparticles influences phagocytosis mechanisms and that elongated polystyrene nanoparticles target lungs and brain endothelium more efficiently than their spherical

counterparts [Champion *et al.* 2006, Kolhar *et al.* 2013].

The most remarkable results regarding the use of elongated carriers were shown by Geng *et al.* 2005 when exploiting the enhanced permeability and retention (EPR) effect. This effect consists in the passive extravasation and retention of nanoparticle through the highly defective blood vessels which are formed as a consequence of the oxygen depletion and release of cytokines in the core of solid tumors [Mustonen *et al.* 1995, Dvorak *et al.* 1999, Maeda *et al.* 2000, Maeda *et al.* 2001]. In their pioneering work the authors showed that elongated poly(ethylene glycol)-b-poly(ϵ -caprolactone) filomicelles display circulation half-life time of up to five days. This result is orders of magnitude larger than what is generally defined as “long circulating nanoparticles” and it is of paramount importance for passive targeting systems as longer circulation increases the probability of passive uptake in the “target” areas. Although these authors concluded to a definitive advantage in using nanocarriers with large aspect ratio, their PEO-PCL filomicelles undergo an elongated to spherical transition due to the hydrolytic degradation of the core forming block. Since the filomicelles are only accumulating after they have decayed to a spherical morphology, this system does not provide any insight on the biodistribution of elongated objects. This can indeed be seen from their results where the only differences between the spherical PEO-PCL micelles and the filomicelles are in the drug loading efficiency and circulation time [Christian *et al.* 2009].

Very recently Müllner *et al.* 2015 investigated the circulation time and biodistribution of high aspect ratio, non-degradable, cylindrical polymer brushes of different stiffness and length. They showed that increasing length and stiffness reduce the circulation time and the accumulation in the spleen. Their results are profoundly different from those of the PCL filomicelles, suggesting a strong importance of stiffness in the biodistribution and circulation time of elongated nanoparticles. However, their study did not provide longitudinal data which is necessary for understanding the accumulation and the elimination pathways involved in the clearance of the nanocarriers.

Here we used longitudinal single photon emission computed tomography (SPECT) imaging to investigate the circulation, the biodistribution and the clearance of rigid model nanocarriers with spherical and cylindrical morphology to obtain a more complete picture of the effects of size and rigidity on these parameters. In order to do this, we used a model system of polystyrene-b-poly(ethylene oxide) micelles and studied *in vitro* and *in vivo* the effect of micelle morphology on their cellular uptake and biokinetics. In the PS-PEO micelles used, the strong hydrophobicity

of the core forming block, polystyrene, and its high glass transition temperature eliminate the possibility of unimer exchange [Wang *et al.* 1995]. From the kinetic entrapment of the unimers within far from equilibrium supramolecular structures, the concept of non-ergodic micelles is derived [Jain *et al.* 2004]. These micelles do not evolve over time while in solution or during their circulation *in vivo*. This characteristic provides both stability and a higher degree of freedom on the possible morphologies that are obtainable with a certain copolymer [Allen *et al.* 1999, Zhu *et al.* 2008, Yu *et al.* 1996].

Subsequently, a fluorescent dye was incorporated and the fluorescently labeled micelles were used for *in vitro* cellular uptake experiments. Finally, ^{111}In was encapsulated and the radiolabeled micelles were used for *in vivo* biokinetics studies by SPECT in healthy mice.

Materials

Poly(styrene-*b*-ethylene oxide) block copolymers PS_{9,5k}-PEO_{18k} (Mn/Mw = 1.09) and PS_{9,5k}-PEO_{5k} (Mn/Mw = 1.04) were purchased from Polymer Source Inc. (Polymer Source Inc., Canada). Anhydrous Chloroform $\geq 99\%$, 0.5 – 1% ethanol as stabilizer, fluorescent dye 1,1'- Dioctadecyl-3,3,3',3'-tetramethylindocarbocyanine perchlorate (DiI), Sephadex® G-25 and Fetal Bovine Serum (FBS), were purchased from Sigma Aldrich (Sigma-aldrich Chemie B.V., The Netherlands). Sterile Phosphate Buffered Saline (PBS), 0.25% Trypsin-Ethylenediaminetetraacetic acid (EDTA) and Penicillin-Streptomycin were purchased from Gibco (Fischer Scientific, The Netherlands). BioWhittaker Dulbecco's Modified Eagle Medium (DMEM) and Ham's F10 were purchased from Lonza (Lonza Benelux B.V., The Netherlands). Vectashield- 4',6-diamidino-2-phenylindole (DAPI) was purchased from Vector Laboratories (Brunschwig Chemie, The Netherlands). Glass stirring bars, one cm long, were purchased from VWR (VWR International, France). Silicon substrates, 5x5 mm polished, were purchased from Siltronix (Siltronix B.V., France). The radioactive ^{111}In -chloride was provided by IDB Holland (IDB Holland B.V., The Netherlands). All the reagents were used as received unless stated otherwise.

Methods

Micelles formation

A stock solution was prepared by dissolving 10 mg/mL block copolymer in chloroform. A 100 μL aliquot of the stock solution was added to 2.3 mL of PBS. After this, an emulsion between

the two immiscible solvents was formed by stirring using a glass coated magnetic stirring bar. The emulsion was stirred until complete evaporation of the chloroform.

Three different micelles were prepared: two of spherical and one of elongated morphology. The spherical ones were formed using $PS_{9.5k}$ - PEO_{18k} . By controlling the evaporation rate of the chloroform phase in the emulsion spherical micelles of two different diameters were obtained. The large spherical micelles, sPSL, were formed by leaving the vial open during the evaporation stage. The small spherical micelles, sPSS, were formed by maintaining the vial closed during the whole evaporation stage. Elongated micelles, ePSS, were formed using $PS_{9.5k}$ - PEO_{5k} and by keeping the vial closed during the evaporation stage.

Fluorescently labeled micelles were prepared by including fluorescent dye DiI directly to the stock solution in 0.02 wt.% to copolymer weight.

Spherical micelle characterization

The intensity weighted particle size distribution and average hydrodynamic diameter of the spherical micelles were obtained by dynamic light scattering (DLS). Each micelle sample was diluted to a concentration of 0.1 mg/mL and measured using an ALV/DLS/SLS-5020F experimental setup (ALV Laser Vertriebsgesellschaft GmbH, Germany) with a He-Ne laser (14 mW, $\lambda_0 = 632.8$ nm), a compact ALV/CGS-8 Goniometer system, and an ALV-7002 autocorrelator at scattering angles from 20°C to 120°C. The CONTIN method was used for the analysis of the normalized autocorrelation functions of the scattered intensity.

Atomic force microscopy (AFM) was used to obtain topographic scans of the spherical micelles. Ten μ L of micelle solution were spin coated onto 5×5 silicon substrates and these were imaged using an NTegra microscope (NT-MDT Co., Russia) in semi contact mode with an NSG03 cantilever ($k = 1.7$ N m⁻¹).

Elongated micelle characterization

The diameter and length of the elongated micelles was determined by scanning electron microscopy (SEM). Droplets of 10 μ L of micelle solution were diluted to 0.1 mg/mL and spincoated onto 5×5 mm silicon substrates. These were imaged using a SU8000 UHR Cold-Emission FE-SEM Scanning Electron Microscope (Hitachi, Japan). The samples were imaged at 1kV acceleration voltage and without applying any conductive coating to the sample.

AFM was also used to evaluate the diameter of the elongated micelles using the same procedure and equipment as for the spherical micelles.

The length distribution of the elongated micelles was reduced using an Ultra Turrax IKA T10 basic homogenizer (IKA, Germany). Each sample of 2.3 mL was homogenized at 30k RPM for 30 seconds in total.

Radiolabeling

A solution of 2.3 mL PBS (pH 7.4) and 1 mM tropolone was prepared. The required amount of ^{111}In was added to this aqueous solution and stirred using a glass coated magnetic stirring bar for 5 minutes, allowing the formation of indium–tropolone complexes. After this, a 100 μL aliquot of polymer stock solution was added and an emulsion with water was formed by stirring the two immiscible solvents with a glass magnetic stirring bar. The emulsion was mixed until evaporation of chloroform.

Purification of the radiolabeled micelles from unencapsulated and uncomplexed tropolone and ^{111}In was performed by size exclusion chromatography using Sephadex[®] G-25 gel. Elution fractions were collected and the activity of each fraction was counted in a 2480 Wizard2 Automatic Gamma Counter (PerkinElmer Nederland BV, The Netherlands).

In vitro characterization of PS-PEO micelles

Details about *in vitro* model and cytotoxicity experiments setup are available in the supplementary materials.

In vivo characterization of PS-PEO micelles

Animal experiments were performed with C57Bl/6 mice according to protocols approved by the Animal Ethical Committee of the UMC Utrecht and in accordance with Dutch Law on Animal experimentation. SPECT/CT imaging was used as a noninvasive method to access circulation dynamics and tissue deposition of ^{111}In -labelled micelles.

Six mice were divided into three study groups of two animals and assigned for imaging with ^{111}In -sPSL, ^{111}In -sPSS or ^{111}In -ePSS micelles respectively. All animals were anesthetized with isoflurane and injected with activity via the tail vein. The average injected activities per study group were 1.45 MBq (1.5 mg) ^{111}In -sPSL, 0.26 MBq (1.8 mg) ^{111}In -sPSS and 0.42 MBq (1.5 mg) ^{111}In -ePSS, respectively. After this, total body SPECT/CT scans of 30 minutes were

acquired at 0 (just after the injection), 24 and 48 hours post-injection (p.i.). To obtain more detailed information on the late-stage biodistribution of the compound in the spleen and the liver of the animals, additional 30 minutes acquisitions focused on the abdominal area were performed immediately after the end of the 48 hours p.i. total body SPECT/CT scans.

SPECT/CT imaging and data analyzing

All animals were imaged in a U-SPECT⁺/CT scanner (MILabs B.V., The Netherlands) [van der Have *et al.* 2009]. The SPECT scans were acquired in a list-mode data format with an ultra-high-sensitivity mouse pinhole collimator [Ivashchenko *et al.* 2015]. After this, SPECT image reconstructions were carried out with a pixel-based order-subset expectation maximization (POSEM) [Branderhorst *et al.* 2010] algorithm that included resolution recovery and compensation for distance-dependent pinhole sensitivity [van der Have *et al.* 2008]. For the SPECT images in this paper, we used 4 subsets and 12 iterations image reconstruction with an isotropic 0.4-mm-voxel grid. Triple-energy-window based Compton scatter correction was performed according to King *et al.* 2004. A 20% ¹¹¹In photopeak window was centered at 171 keV. Two background windows were placed on both sides of the photopeak window with a width of 4% of the photopeak, i.e. 6.8 keV each. Hereafter, non-uniform attenuation correction and absolute quantification of SPECT images was performed according to Wu *et al.* 2010. For visual representation in the manuscript the reconstructed volumes of SPECT scans were post-filtered with three-dimensional Gaussian filter.

Corresponding CT scans were acquired with a tube setting of 55 kV and 615 μ A. In total, 2 frames of 182 projections over 360° were acquired in step and shoot rotation mode. The acquired projection data was reconstructed using SkyScan NRecon software to generate a 3D CT image on 0.1693x0.1693x0.1695 mm voxel grid.

To calculate the uptake of radiolabeled micelles in the organ of interest, the registered to CT and quantified SPECT images were analyzed using PMOD 3.6 biomedical image analyzing software (PMOD, Switzerland). A three-dimensional region-of-interest (ROI) was manually drawn to encompass the radioactivity uptake in the organ whose boundary was delineated in the three-dimensional CT images. Separate ROIs were drawn for the radioactivity uptakes in the heart, liver, spleen, brain, lungs, left and right kidneys, and the bladder. The uptake was expressed as % injected dose (%ID) per mL of tissue volume (%ID/mL).

All quantification data was reported as mean \pm standard deviation within one animal study

Table 1. List of the micelles used. The diameters of the two spherical micelles are hydrodynamic diameters obtained by DLS while the diameter and length of the elongated micelles were obtained by SEM measurements.

Micelle type	Copolymer	Diameter, nm			Length, nm
		DLS	AFM	SEM	SEM
sPSS	PS _{9.5k} -PEO _{18k}	170 ± 8	190 ± 32	/	/
sPSL	PS _{9.5k} -PEO _{18k}	106 ± 7	120 ± 21	/	/
ePSS	PS _{9.5k} -PEO _{5k}	/	92 ± 12	31 ± 3	600 ± 310

group. Comparison of statistical correlation between the biodistribution of different nanocarriers was conducted using Pearson's correlation coefficient.

Results

*Formation and Characterization of PS-*b*-PEO micelles*

The three types of micelles used in this work, with the forming copolymer and their size characterization performed by dynamic light scattering (DLS), atomic force microscopy (AFM) and scanning electron microscopy (SEM), are reported in Table 1.

The hydrodynamic diameter of the spherical micelles was measured by DLS. The two types of spherical micelles, sPSS and sPSL, were obtained by tuning the evaporation rate of the solvent during the emulsion process. The larger micelles, sPSL, were obtained through a fast evaporation rate (approximately 4 hours for 100 μL of chloroform in water), while the smaller ones, sPSS, were obtained by a slower more sustained evaporation rate (approximately 24 hours for 100 μL of chloroform in water). The size of the micelles was also verified using AFM (Figure 1).

Elongated Micelles Characterization and Length Distribution

Micelles of elongated morphology, ePSS, were characterized using AFM and SEM. As formed, the elongated micelles have a very broad length distribution that reaches hundreds of microns. In order to make them suitable for *in vivo* applications, the micelles were shortened using a high power homogenizer. The strong shear stress applied during mixing fractured the micelles and resulted in a more narrow length distribution with an average length of 0.6 μm (Figure 2). The diameter of the ePSS micelles was also obtained by SEM and AFM and is respectively: dSEM = 31 ± 3 and dAFM = 92 ± 11 nm.

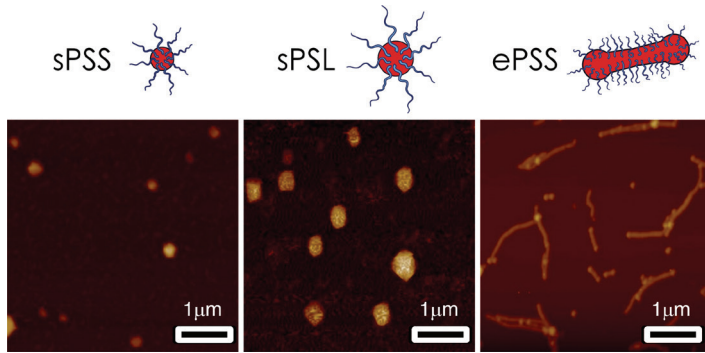


Figure 1. Atomic Force Microscopy semi-contact topography scan of the three micelles. From left to right are the sPSS, sPSL and ePSS micelles. The diameter of the micelles is obtained from the FWHM of the topography scans.

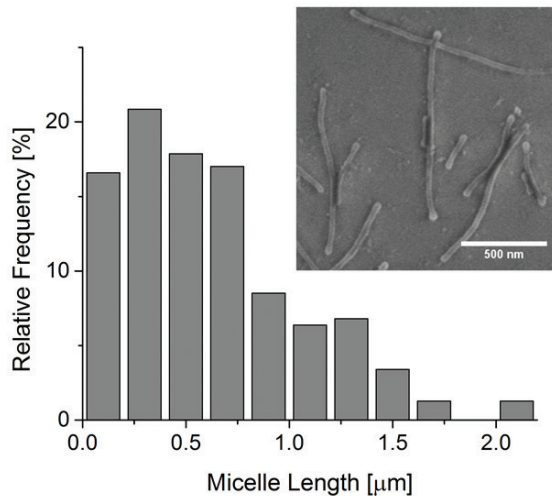


Figure 2. Length distribution of the micelles after homogenization. The longest micelles are fractured into many shorter ones. The lengths were measured from SEM micrographs like the one shown in the inset.

In vitro characterization of PS-*b*-PEO micelles

Cytotoxicity

The cytotoxicity of the micelles on human cervical (HeLa) cells was determined using the water soluble tetrazolium assay (WST-1) for four micelle concentrations, between ~0.005 mg/mL and ~5 mg/mL, and three incubation times: 24, 48 and 72 hours. The results are shown in Figure 3. At the concentrations used in this work, there is no visible effect of micelle morphology on their cytotoxicity.

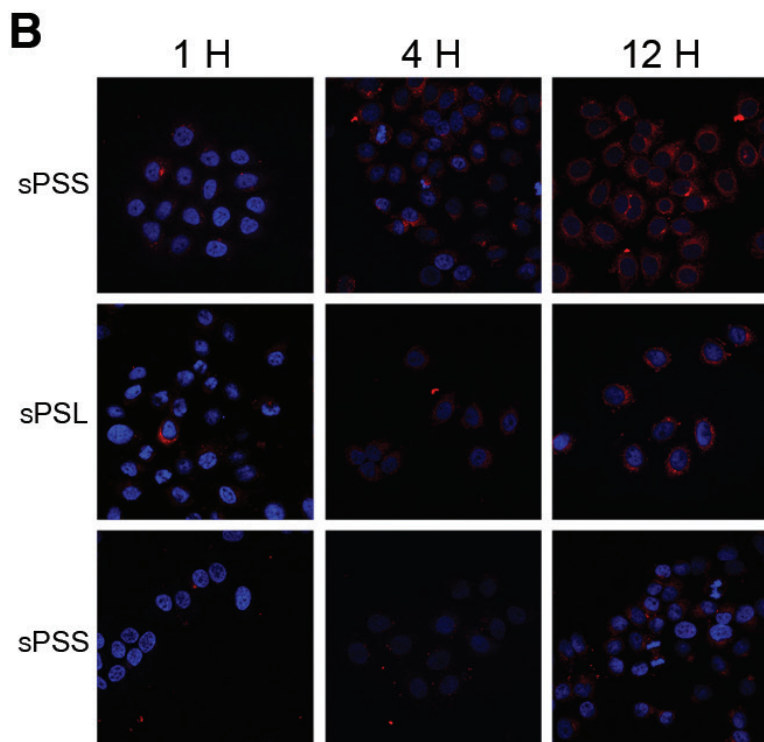
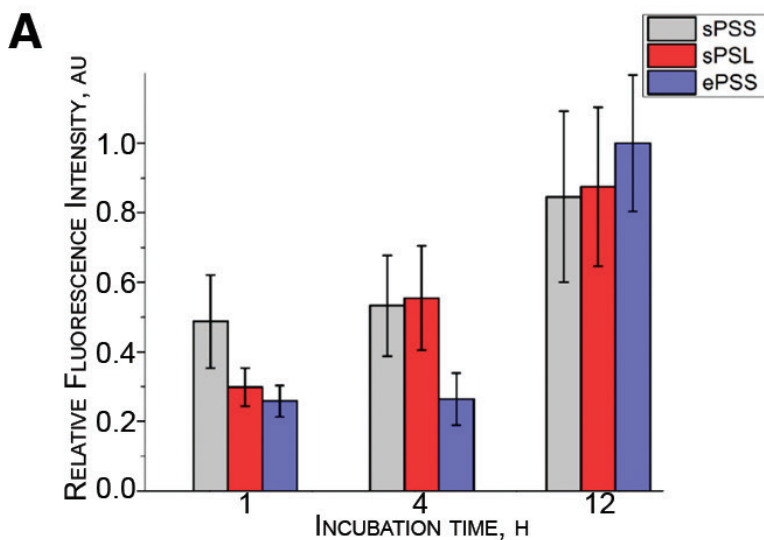


Figure 3. A, Internalization of spherical and elongated fluorescently micelles in HeLa cells. The fluorescence was measured from CLSM images, such as those in figure B, and averaged per cell. The results are normalized relatively to the maximum fluorescence measured. The elongated micelles, ePSS, appear to be internalized at two different rates. A faster rate, comparable with that of the larger spherical micelles, and a slower one, which however results in a larger delivery of fluorescent dye to the cells.

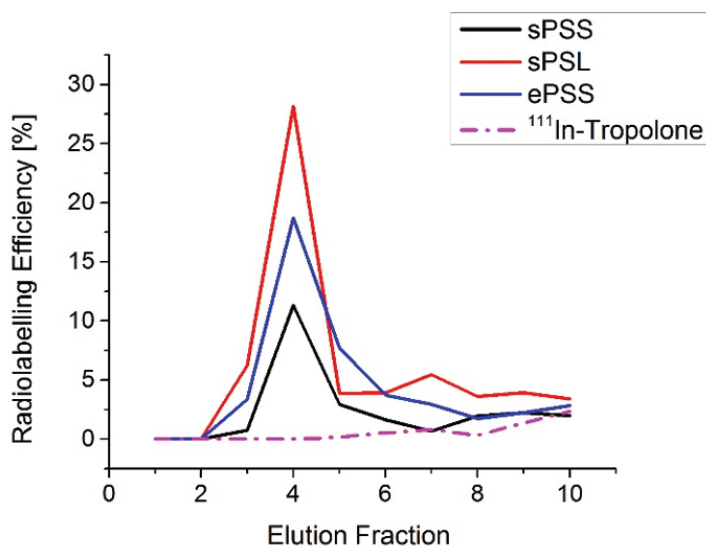


Figure 4. Elution profile of the ¹¹¹In labelled micelles. Free ¹¹¹In-Tropolone is used as a control. In the first five fractions the micelles are eluted while free ¹¹¹In-Tropolone is retained in the column.

Fluorescence internalization

Micelles were loaded with the fluorescent dye DiI to track their internalization in HeLa cells. The average fluorescence per cell was determined from confocal micrographs and is related to the total amount of fluorescent dye internalized by the cells. The results are shown in Figure 3.

In the initial hour of incubation the smaller spherical micelles are the ones most efficiently taken up by the cells. Within 4 hours of incubation the sPSL micelles reach uptake values equal to those of the sPSS. This indicates that the amount of internalized fluorescent dye is the same for both micelle types. The elongated micelles, ePSS, appear to be internalized at two different rates. A faster rate, comparable with that of the larger spherical micelles, and a slower one, which however results in a larger delivery of fluorescent dye to the cells.

Radiolabeling and purification of PS-*b*-PEO micelles

The method used to encapsulate the radioisotope ¹¹¹In in the core of the micelles is based on the method developed by Laan *et al.* 2016 where the isotope is complexed with the lipophilic chelator tropolone. Tropolone is a water soluble weakly negatively charged molecule which forms lipophilic complexes with the positively charged ¹¹¹In (oxidation state of 3+) in water solution at pH 7.4. These lipophilic complexes migrate to the chloroform phase during the evaporation of the emulsion that is required for the formation of the micelles. As the chloroform

evaporates, the complex will be entrapped in the hydrophobic core of the micelles.

The encapsulation efficiency depends on the partition of indium-tropolone complexes between the aqueous and organic phases of the emulsion. The unencapsulated ^{111}In is separated from the radiolabeled micelles using size exclusion chromatography. The elution profiles are shown in Figure 4. Free ^{111}In -tropolone is shown as a control. By selecting the elution fractions 3 to 5, all free ^{111}In is excluded from the micelle solution. The total radiolabelling efficiencies are shown in Table S1. No changes in size were found when characterizing the plain micelles and the radiolabeled ones.

In vivo biodistribution

In vivo SPECT studies were performed to assess the morphology-dependence of *in vivo* biokinetics and blood circulation of the micelles. Quantitative *in vivo* SPECT imaging has been chosen over blood sampling as a non-invasive evaluation of the circulation time. This has been done to not affect the animal's welfare [Holmberg *et al.* 2011, Tsai *et al.* 2015] and, additionally, to not influence the residual concentration of radiopharmaceutical compounds in the blood stream which may affect the biodistribution of long-circulating radiopharmaceutical compounds during longitudinal studies. Moreover, with respect to organ internalization, it has been shown that quantitative SPECT measurements only deviate by less than 2.8% from gamma-counter measurements for ^{111}In , therefore proving that SPECT is currently the ideal technique for non-invasive longitudinal studies [D'Addio *et al.* 2012, Wu *et al.* 2010, Finucane *et al.* 2011].

Figure 5, A and Video S1–S3 show the maximum intensity projections of follow-up total body SPECT/CT scans for three mice, depicting the longitudinal changes in the biodistribution of ^{111}In -sPSS (top), ^{111}In -sPSL (middle) and ^{111}In -ePSS (bottom) micelles. At the same time, quantified uptake of the compound in multiple organs of interest (Figure 5, B and Table S2 - S3) provides an absolute quantitative measure of the micelle distribution in the tissue.

Our results show (Figure 5) that all nanocarriers have a high blood activity concentration (17.6 ± 3.6 %ID/mL ^{111}In -sPSS, 17.4 ± 6 %ID/mL ^{111}In -sPSL, 15.0 ± 3.6 %ID/mL ^{111}In -ePSS, based on heart uptake values) and rapid spleen uptake (12.2 ± 4.3 %ID/mL ^{111}In -sPSS, 11.0 ± 1.3 %ID/mL ^{111}In -sPSL, 24.7 ± 0.4 %ID/mL ^{111}In -ePSS) during early stage of the experiment. At the same time, the presence of a renal shell image at 0 hours p.i. scans suggests fast renal clearance of the compounds. However, the near absence of bladder activity accumulation by

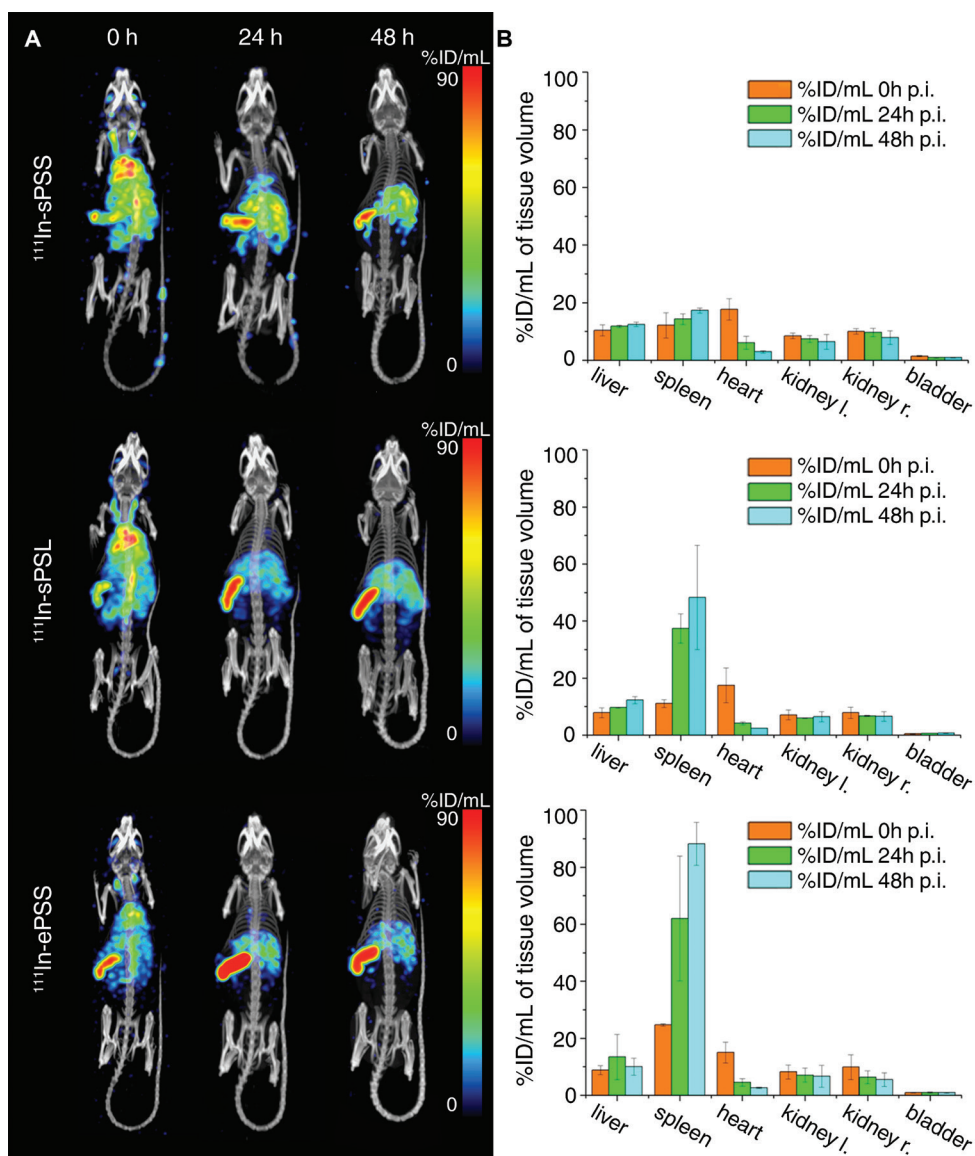


Figure 5. A - Maximum intensity projections of follow-up total body SPECT/CT scans of three mice at 0, 24 and 48 hours post injection of ^{111}In -sPSS (top), ^{111}In -sPSL (middle) or ^{111}In -ePSS (bottom) compound respectively. B - quantified uptake of the compounds in multiple organs of interest, calculated from corresponding SPECT/CT scans.

the end of 0 hours p.i. scans (i.e. 30 min p.i.) and the remaining renal cortex shell image on the later stage scans (24 and 48 hours p.i.) suggest an entrapment of the micelles in the renal cortex tissue. This interpretation is consistent with the value of kidney uptake on quantification plots (Figure 6, B) which remained almost constant during the two days of follow-up studies.

SPECT images at 24 hours p.i. show high level of activity elimination from the main vessels and the heart ($6.1 \pm 2.2\%ID/mL$ ^{111}In -sPSS, $4.2 \pm 0.6\%ID/mL$ ^{111}In -sPSL, $4.6 \pm 1.3\%ID/mL$ ^{111}In -ePSS) of the animals, that is later followed by total clearance of the compounds from the blood, to the level of background signal, prior 48 hours p.i. imaging ($r > 0.99$ for all compounds).

The liver and spleen uptake become more prominent with time: ^{111}In -sPSL and ^{111}In -ePSS show very similar dynamics of spleen uptake ($r > 0.99$), yet have different rates of indium decomposition. For the ^{111}In -sPSL there is an increase of 3.3 times in the spleen uptake, from 0 to 24 hours p.i., while for the ^{111}In -ePSS the increase is 2.6 times. Liver accumulation of ^{111}In -sPSS micelles remains almost constant during two days of imaging, while a small increase in spleen accumulation (12.2 ± 4.4 , 14.3 ± 1.8 and $17.3 \pm 0.9\%ID/mL$ at 0, 24 and 48 hours p.i.) is observed. Micelles of spherical morphology, ^{111}In -sPSS and ^{111}In -sPSL, showed similar dynamics of liver uptake ($r = 0.94$).

Fused SPECT/CT slices of 48 hours p.i. scans focused on the abdominal area of the animal (Figure 6) show, in detail, the late stage biodistribution of ^{111}In -sPSS (top), ^{111}In -sPSL (middle) and ^{111}In -ePSS (bottom) micelles. Closer examination of the activity distribution on the coronal slices (Figure S2–S4) reveals a relatively high level of ^{111}In uptake within the liver which appears to be distributed homogeneously for the ^{111}In -sPSS micelles and increasingly heterogeneously going from the ^{111}In -sPSL to the ^{111}In -ePSS which also showed some liver clearance.

It was previously reported that micelles of elongated morphology, when compared to their spherical analogues, can have high brain and/or lungs uptake [Kolhar *et al.* 2013]. However, the brain uptake of the elongated ^{111}In -ePSS micelles studied in this work ($1.9 \pm 0.3\%ID/mL$ ^{111}In -ePSS at 0 h p.i., Table S2) had no significant difference with the uptake of spherical micelles ($1.8 \pm 0.4\%ID/mL$ ^{111}In -sPSS, $1.7 \pm 0.1\%ID/mL$ sPSL at 0 h p.i.). Moreover, although we saw a high activity concentration in lungs ($13.6 \pm 2.1\%ID/mL$ ^{111}In -sPSS, $13.2 \pm 1.2\%ID/mL$ ^{111}In -sPSL and $10.6 \pm 3.0\%ID/mL$ ^{111}In -ePSS; Table S2) at the early stage of the experiment (0 h p.i.), this value significantly decreased over imaging days ($4.5 \pm 1.2\%ID/mL$ ^{111}In -sPSS, $3.1 \pm 0.3\%ID/mL$ ^{111}In -sPSL, $3.4 \pm 1.0\%ID/mL$ ^{111}In -ePSS at 24 h p.i.). In this case, the initial high activity concentration in the lungs, is probably associated with the relatively high perfusion of the lungs (~4.5 time higher than in liver), while the gradual decrease in lungs activity concentration indicates that none of the compounds is being trapped in the organ. For all compounds studied, negligible activity was accumulated in the skeleton of the animals (Figure 5). This indicates that minimal dissociation of ^{111}In in its ionic form from the carriers after i.v. administration [Hosain *et al.*

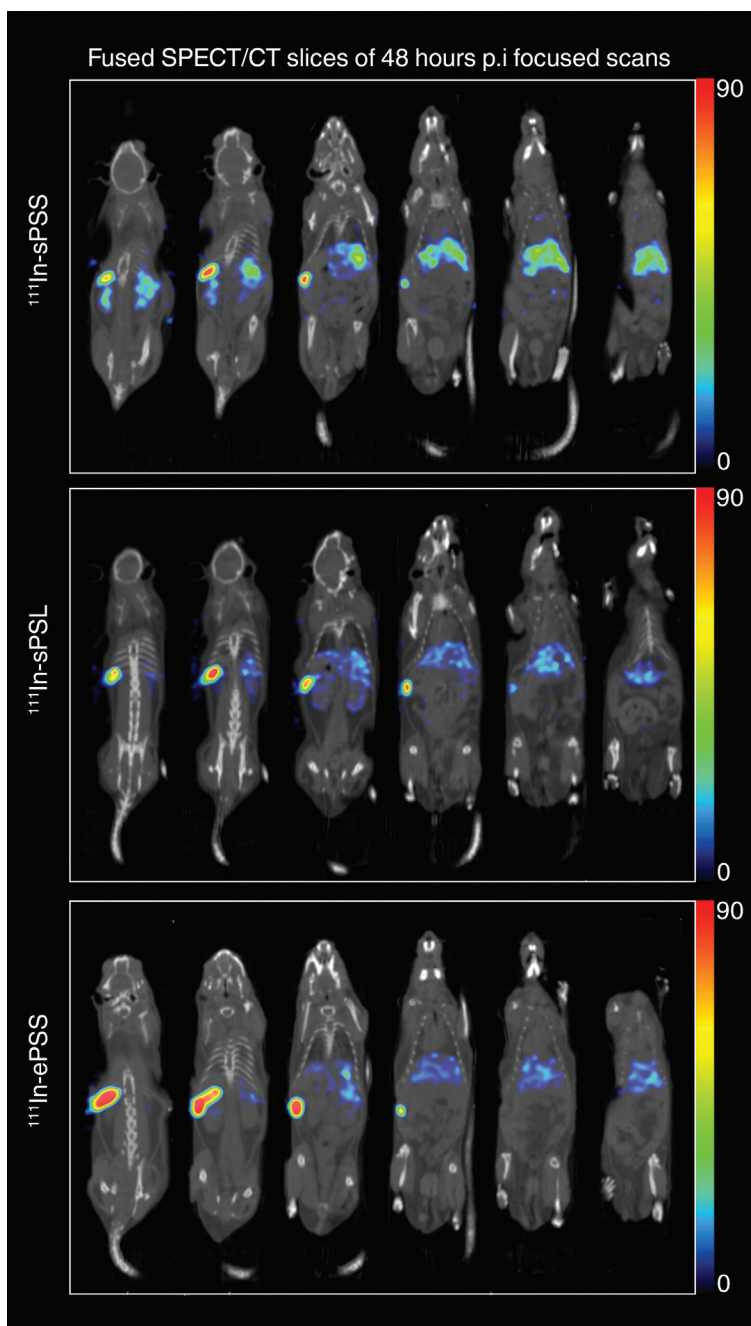


Figure 6. Fused SPECT/CT slices of focused abdominal area scans (right) at 48 hours post injection of $^{111}\text{In-sPSS}$ (top), $^{111}\text{In-sPSL}$ (middle) or $^{111}\text{In-ePSS}$ (bottom) compound respectively.

1969, Adatpe *et al.* 1971, Ohtake *et al.* 2008]. This statement is consistent with the previously reported mouse serum stability tests for ^{111}In -labelled micelles equivalent to the ones used in our

experiments [Laan *et al.* 2016].

Discussion

In this work we studied the effects of the shape, size and rigidity of PS-PEO micelles on their circulation time, general bio-distribution and clearance pathways in mice.

Spherical and elongated micelles of polystyrene-*b*-poly(ethylene oxide) were prepared using a co-solvent evaporation method which made it possible to physically encapsulate a hydrophobic fluorescent dye or complexed radioisotopes from the micelle formation stage without altering their surface properties.

From *in vitro* cellular internalization experiments with HeLa cells it was found that the internalization rate of the micelles depends on their morphology. In contrast to micelles of spherical morphology (sPSS d = 120 nm and sPSL d = 190 nm), that showed approximately constant rate of cellular internalization over 12 hours, the elongated micelles (ePSS 30× 600 nm) appear to be internalized at two different rates. The initial phase is characterized by slow rate of cellular internalization (up to 4 hours) and the late phase has a fast uptake. However, when compared to spherical micelles, both uptake rates of ePSS result in a larger delivery of fluorescent dye to the cells. In this case, the higher loading capacity of elongated micelles with respect to spherical ones illustrates one of their major advantages as drug carriers [Geng *et al.* 2005, Christian *et al.* 2009]. Moreover, no cytotoxic effects for the different micelle morphologies were found for concentrations up to 5 mg/mL which was more than double the concentration used for *in vivo* studies.

Next, the micelles were radiolabelled with ¹¹¹In and we studied their biodistribution in healthy mice. Overall, the major site of accumulation for all compounds studied was the spleen. Regarding the circulation time, our results demonstrated that the carrier with the fastest initial clearance is ¹¹¹In-ePSS. The carrier with the longest circulation time is ¹¹¹In-sPSS which showed the highest %ID/mL heart uptake value (Figure 5, B) in the 24 hours p.i. scan. This value represents an average activity concentration in the blood passing through the heart. ¹¹¹In-sPSL and ¹¹¹In-ePSS showed slightly lower heart uptake values at 24 hours p.i. (Figure 5, B and Table S2), but all three morphologies show no statistical difference in blood activity concentration at 48 hours p.i. Furthermore, a significant late stage increase in spleen uptake of ¹¹¹In-sPSL and ¹¹¹In-ePSS (Figure 5, B) suggests a circulation time of the compounds that is longer than 24

hours. These results correlate with previously reported long circulation times for PS-PEO micelles and suggest a good potential for EPR effect related investigation [D'Addio *et al.* 2012]. However, based on our results we can state that the high aspect ratio of PS-PEO elongated micelles does not provide an increased circulation time. This is especially different from the order of magnitude increase in circulation time that was previously reported by Geng *et al.* 2005 for the PEO-PCL filomicelles [Geng *et al.* 2005, Christian *et al.* 2009]. Our results are more closely related to those obtained by Müllner *et al.* 2015, who used high molecular weight brush copolymers to study their circulation time and biodistribution while varying the length and rigidity of the backbone [Müllner *et al.* 2015]. The authors showed that an increased length results in an increased splenic capture, while an increased rigidity results in a faster clearance. The aspect of rigidity was also confirmed recently by Anselmo *et al.* 2015 who showed using spherical hydrogel nanoparticles that the circulation time decreases with increasing rigidity of the particles [Anselmo *et al.* 2015]. From this we can conclude that for micelles with a stiff core, such as the polystyrene based ones used in this work, the circulation time is longer for spherical particles rather than elongated ones.

Finally, we can summarize the difference in longitudinal *in vivo* biodistribution of the three micelle types through their differences in size and morphology. The general trend observed is that the PS-PEO nanocarriers accumulate in the spleen, liver and renal cortex. The nanocarriers with larger characteristic dimensions accumulate preferentially in the spleen, while the smallest are divided equally between spleen and liver. Nanoparticles which are larger than 100 nm have been shown to preferentially accumulate in the spleen rather than the liver which is consistent with our results with the spherical micelles [Duan *et al.* 2013]. Moreover, stiffer carriers have also been reported to accumulate preferentially in the spleen rather than the liver [Bertrand *et al.* 2012]. As a result of the combination of their sizes and stiffness, given by the polystyrene core, the elongated micelles show a remarkably specific spleen uptake. As previously mentioned, the splenic accumulation of the larger micelles is consistent with the results shown for high molecular cylindrical polymer brushes [Müllner *et al.* 2015]. Since the spleen is the primary organ of the immune system this result could lead to interesting applications, for example in the field of vaccine delivery [Yang *et al.* 2013]. At the same time, it must be noted that our experiments were carried out on an animal model (C57Bl/6 mouse) with non-sinusoidal spleen, while both rat and human spleens have a sinusoidal structure. The sinusoidal sleeves provide an extra layer of filtration for carriers which have high rigidity, sizes larger than 200 nm and elongated shapes [Demoy *et al.* 1999, Liu *et al.* 2008]. Regarding the liver, the Kupffer cells are responsible for the internalization of nanoparticles. These are known to have a rough surface

which promotes phagocytosis of particles with a diameter between 1 and 3 μm [Champion *et al.* 2006, Doshi *et al.* 2010]. The carrier which mostly represents this range are the elongated micelles ePSS along their long axis. However, our results show that the small spherical particles are being preferentially uptaken in the liver. This is again likely due to the rigidity of the elongated micelles which promotes their spleen uptake and indirectly contributes to a reduction of the accumulation in the liver.

Conclusion

Spherical and elongated micelles of polystyrene-b-poly(ethylene oxide) were prepared using a co-solvent evaporation method which made it possible to physically encapsulate a hydrophobic dye and complexed radioisotopes from the micelle formation stage. This theranostic device shows great versatility for research purposes since markers, as long as hydrophobic, can potentially be encapsulated without costly formulation efforts and without influencing the surface properties of the carriers. From these experiments it was found that the internalization rate of the micelles depends on their morphology. Moreover, no cytotoxic effects for the different micelle morphologies were found for concentrations up to 5 mg/mL.

The micelles mainly distributed between liver and spleen for all the three samples tested. The size increase of spherical micelles influenced their rates of spleen accumulated without any obvious effect of general liver uptake. The elongated micelles showed a delayed liver clearance and a remarkably specific accumulation in the spleen which is explained by their morphology coupled with the stiffness of the core forming block. Finally, the shorter circulation time of the elongated micelles, caused by their rigid core, highlights the importance of describing elongated micelles not only as a function of their size, but also of their mechanical properties. Further studies using non degradable elongated micelles of different stiffness, and therefore persistence length, are necessary in order to further clarify the aspect of morphology related biodistribution and circulation time.

Supplementary Materials

In vitro characterization of PS-PEO micelles

In vitro model

The evaluation of the carriers' *in vitro* was carried out using HeLa cancer cells. These were cultured in full DMEM medium containing 10% FBS and 100 units/mL penicillin-streptomycin. The cells were kept at 37°C in humidified atmosphere (5% CO₂ in air). The cells were harvested by trypsinization with trypsin-EDTA.

Cytotoxicity

The cytotoxicity of the PS-b-PEO micelles was determined using the WST-1 ver. 16 (Roche Life Science, Switzerland) colorimetric assay. WST-1 contains the 2-(4-Iodophenyl)-3-(4-nitrophenyl)-5-(2,4-disulfophenyl)-2H-tetrazolium salts which are cleaved to formazan by cellular enzymes. Increase in the number of viable cells results in an increase of enzymatic activity, which translates to an increased amount of formazan dye. The amount of formazan dye was measured against blank samples in 96 well plates using a Powerwave XS multiwell spectrophotometer (Biotek, United States). The absorbance of the formazan product was measured at 440 nm. For each micelle sample four different concentrations, from 0.005 mg/mL to 5 mg/mL, were incubated for 24, 48 and 72 hours.

Fluorescence uptake

Cells were seeded in 6-well plates, each containing one borosilicate glass slide 20 x 20 mm, at a density of 5 x 10⁵ cells/well in 1.5 mL of medium. These were incubated at 37°C and 5% CO₂ for 24 hours. After this, 300 uL of micelle solution was added to each well to obtain a final concentration of 1.3 mg of micelles per well. The samples were left for different incubation times, after which the coverslips were rinsed with PBS to remove all non-uptaken micelles and sealed on a glass slide using transparent Roti® liquid barrier marker. Five uL of Vectashield-DAPI were added between the coverslip and the glass slide to stain the nuclei and preserve fluorescence in the sample. Confocal images of the samples were made using a LSM 710 confocal microscope with a Fluor 40x/1.30 Oil M27 objective (Carl Zeiss Microscopy GmbH, Germany). The DAPI signal was excited using a 405 nm diode (emission 460 nm), while the DiI using a 543 nm He-Ne laser (emission 563 nm). From confocal micrographs of the cells, the average DiI signal per cell was measured. Control samples with no added micelles were used for background correction.

Supporting Videos

Video S1 <http://www.rsc.org/suppdata/c6/bm/c6bm00297h/c6bm00297h2.avi>

Video S2 <http://www.rsc.org/suppdata/c6/bm/c6bm00297h/c6bm00297h3.avi>

Video S3 <http://www.rsc.org/suppdata/c6/bm/c6bm00297h/c6bm00297h4.avi>

Supporting Figures and Tables

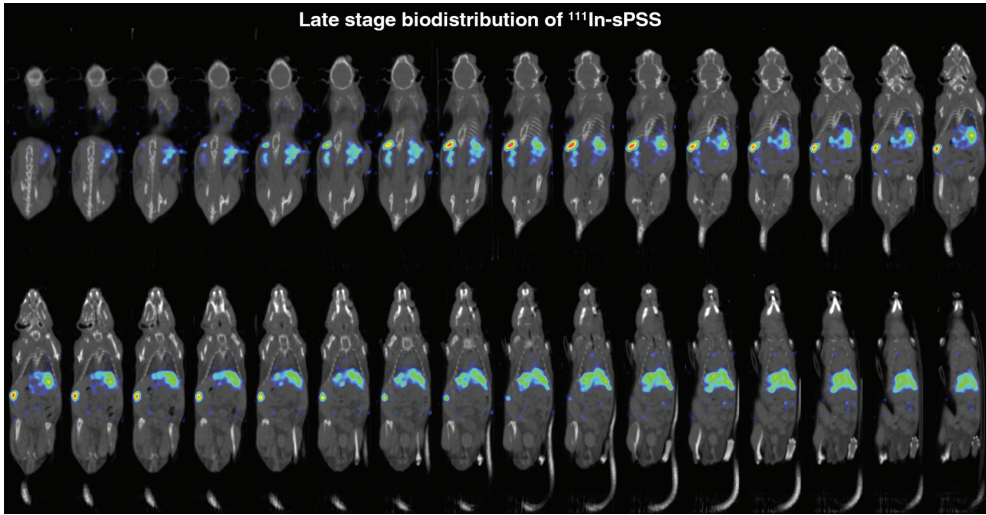


Figure S1. Fused SPECT/CT slices of late stage bioudistribution of ^{111}In -sPSS, obtained from 48 h p.i. SPECT scan with focusing on abdominal area of the animal.

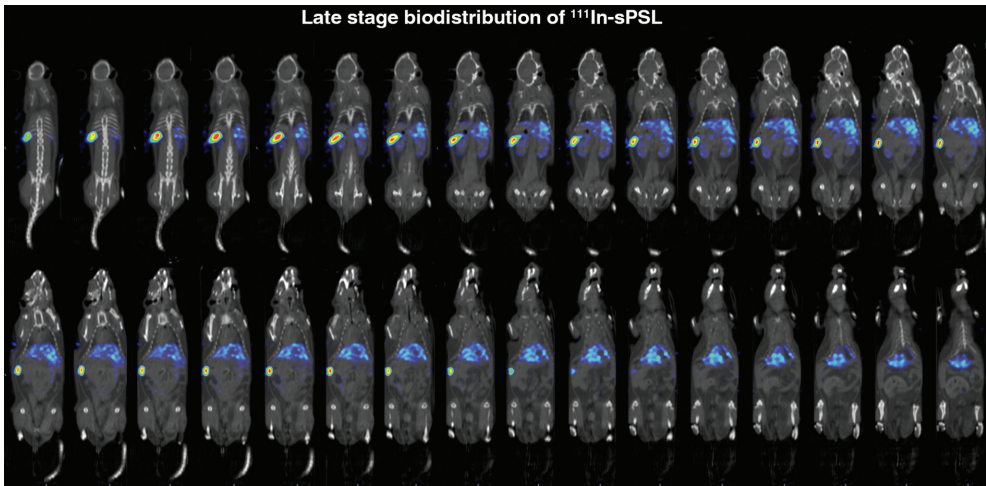


Figure S2. Fused SPECT/CT slices of late stage bioudistribution of ^{111}In -sPSL, obtained from 48 h p.i. SPECT scan with focusing on abdominal area of the animal.

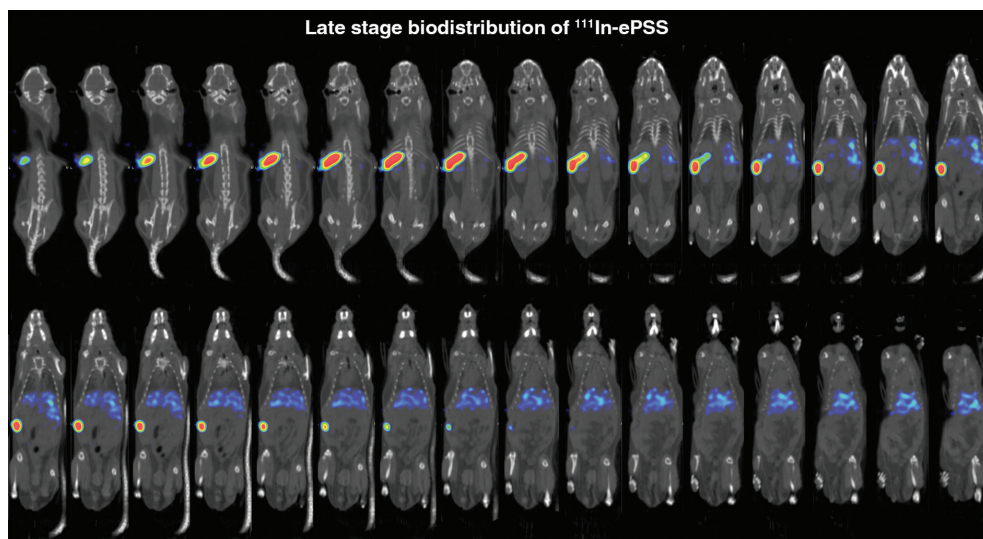


Figure S3. Fused SPECT/CT slices of late stage bioudistribution of ^{111}In -ePSS, obtained from 48 h p.i. SPECT scan with focusing on abdominal area of the animal.

Table S1. Radiolabeling efficiency of the different micelles.

Micelle type	Encapsulation efficiency
^{111}In -sPSS	13%
^{111}In -sPSL	30%
^{111}In -ePSS	22%

Table S2. Comparison of accumulation rates of ¹¹¹In-labelled sPSS, sPSL and ePSS micelles in the kidney, liver and spleen of the animals at 0, 24 and 48 h p.i..

Organ	Compound	Uptake [%ID/mL]		
		0 h	24 h	48 h
Heart	¹¹¹ In-sPSS	17.7±3.7 ^a	6.1±2.2	3.0±0.4
	¹¹¹ In-sPSL	17.4±6.1	4.2±0.6	2.4±0.1
	¹¹¹ In-ePSS	15.0±3.6	4.6±1.3	2.7±0.2
Liver	¹¹¹ In-sPSS	10.4±1.9	11.8±0.4	12.5±0.8
	¹¹¹ In-sPSL	7.9±1.7	9.6±0.2	12.3±1.3
	¹¹¹ In-ePSS	8.8±1.5	13.5±8.0	10.1±3.0
Spleen	¹¹¹ In-sPSS	12.2±4.4	14.3±1.8	17.3±0.9
	¹¹¹ In-sPSL	11.1±1.4	37.5±5.1	48.3±18.2
	¹¹¹ In-ePSS	24.7±0.4	62.0±21.9	88.2±7.5
Brain	¹¹¹ In-sPSS	1.8±0.4	1.1±0.2	0.9±0.1
	¹¹¹ In-sPSL	1.7±0.1	0.8±0.1	0.5±0.1
	¹¹¹ In-ePSS	1.9±0.3	1.0±0.4	0.8±0.1
Lungs	¹¹¹ In-sPSS	13.6±2.1	4.5±1.2	2.1±0.1
	¹¹¹ In-sPSL	13.2±1.2	3.1±0.3	1.6±0.1
	¹¹¹ In-ePSS	10.6±3.0	3.4±1.0	2.0±0.2

^a Standard deviation of the uptake within one study group of the animals

Chapter 7

Summary & Discussion



Summary of the thesis

Single Photon Emission Computed Tomography (SPECT) is a key imaging modality in preclinical research that has developed very rapidly over the past decade. Novel multi-pinhole collimator geometries, stationary system designs, advanced data acquisition modes, improved system calibration and system modeling, the development of accurate attenuation and scatter correction methods, as well as new image reconstruction algorithms have enabled routine high-resolution, dynamic and accurate quantitative *in vivo* SPECT of small-animals (e.g., rodents). This thesis describes the evaluation of some recent technical SPECT instrumentation developments, focusing on the improvement of spatial resolution, system sensitivity, and feasibility of imaging with high-energy γ -emitting isotopes, for existing and new imaging applications of preclinical SPECT.

The small size of animals used in preclinical research poses enormous challenges to the image resolution required to resolve tracer uptake at intratumoral or sub-organ levels. In **Chapter 2** of this thesis, we investigated the performance of the latest-generation of U-SPECT systems (U-SPECT⁺) with a collimator with 0.25-mm pinholes. Using phantom studies we showed that this collimator enables quantitative imaging of molecular uptake in structures down to a quarter of a millimeter, corresponding to approximately 0.015 μL volumetric resolution. This is significantly better than the smallest structures that could be resolved with earlier versions of U-SPECT (0.04 μL) or PET (VECTor: 0.4 μL). Additionally, the level of details that our results have shown in *in vivo* bone SPECT (e.g., visibility of the femur epicondyle sulcus) can enable new imaging applications in, for example, orthopedic research, and may allow for the replacement of *ex vivo* methods, like autoradiography, with high-resolution *in vivo* imaging.

The ability to perform high-resolution and quantitative SPECT imaging of the combined γ - and β -emitting isotope ^{131}I is crucial for the development of new therapies for cancer. However, preclinical imaging of this isotope is challenging. Due to the relatively high energy of ^{131}I gamma photons (364 keV), they can easily penetrate the collimator wall and pinhole edges. This severely degrades the resolution, compared to what is attained for conventional SPECT isotope $^{99\text{m}}\text{Tc}$, if standard collimators were to be used. To enable SPECT with high-energy isotopes, a dedicated clustered multi-pinhole (CMP) collimator was developed in our group which is subject to reduced edge penetration. Evaluation of this collimator for ^{131}I imaging is the topic of **Chapter 3**. To this end, we first improved modeling of photon transport during iterative image reconstruction for 364 keV. Next, quantification accuracy and resolution of ^{131}I

SPECT were evaluated using multiple phantoms, while *in vivo* imaging performance was illustrated with multiple static and dynamic ^{131}I -sodium iodide (NaI) SPECT/CT scans of mice. Our result showed good quantitative image accuracy and reconstructed image resolution below 0.6 mm. This provides an opportunity to perform quantitative analysis of ^{131}I uptake/biodistribution within small organs in mice and, based on this analysis, to calculate animal-specific *in vivo* 3D dose distributions. Both can be highly valuable for developing of targeted ^{131}I cancer therapies.

Choosing the optimal trade-off between collimator resolution and sensitivity for the task at hand can be challenging in preclinical SPECT. The small size of rodents has tended to put the main focus of SPECT development in the past decade on resolution improvements. As a result, the sensitivity of modern multi-pinhole collimator systems rarely exceeds 0.2%, while many SPECT imaging applications can benefit from higher sensitivity SPECT. In **Chapter 4** we describe a dedicated ultra-high-sensitivity pinhole SPECT collimator that we developed. It has 1.3% peak sensitivity and still can reach 0.85 mm reconstructed spatial resolution for $^{99\text{m}}\text{Tc}$. The animal scans presented in this chapter illustrate the possibility of either performing ultra-fast dynamic SPECT with 1s time-frames, or SPECT with sub-MBq amounts of activity. Based on its performance, the collimator can thus be used for reducing the animal dose during follow-up molecular imaging studies or for improving the frame rate during the imaging of fast biological processes. Additionally, it can increase the possible number of applications, e.g. for imaging of organs that have low specific uptake or imaging with tracers and nanocarriers that have low labeling efficiency.

The use of nanocarrier-based pharmaceuticals is particularly promising in oncology, where the leaky vasculature of tumors and impaired lymphatic drainage allows one to reach high drug accumulation and retention via the enhanced permeability and retention (EPR) effect. This effect strongly depends on the blood circulation time and general biodistribution of the carriers. Thus, longitudinal biodistribution studies play a major role during the preclinical evaluation of new nanocarriers (e.g., nanomedicines). Nevertheless, due to the high initial renal clearance and the long blood circulation times of the carriers, longitudinal imaging of their biodistribution poses a challenge to the sensitivity of SPECT systems. As a result, it is commonly replaced with *ex vivo* methods. In **Chapter 5** and **Chapter 6**, we show two applications of longitudinal low-dose SPECT imaging of polymeric nanocarriers that were enabled by the collimator developed in chapter 4.

In chapter 5, we studied the influence of different poly(ethylene oxide) (PEO) block lengths and aggregation states (unimers versus micelles) on the biodistribution of Pluronic nanocarriers. The *in vivo* biodistribution of ^{111}In -radiolabeled compounds was performed in healthy mice using longitudinal (up to 48 hours p.i.) SPECT/CT scans. This approach eliminates the recurrent limitation associated with the dynamic nature of copolymer micelles and allows us to use similar concentrations of both types of nanocarriers. Our results show that, through varying the PEO block lengths and aggregation states of the copolymers, different renal and liver clearances are obtained. The outcomes of this work can be beneficial for a more rational development of Pluronic-based nanocarriers and for the future of EPR-based cancer therapies.

In chapter 6, we used SPECT to investigate the circulation, biodistribution, and clearance of rigid model polystyrene-*b*-poly(ethylene oxide) nanocarriers with spherical and cylindrical morphology. This was done to obtain a more complete picture of the effects of size and rigidity on *in vivo* behavior of the carriers. The glassy nature of polystyrene guaranteed the morphological stability of the carriers *in vivo*, and through encapsulating ^{111}In in their cores, an assessment of the longitudinal *in vivo* biodistribution of the particles in healthy mice could be performed with low-dose SPECT imaging (down to 0.26 MBq/animal activity). Our results show prolonged blood circulation for all micelle morphologies studied, while the dynamics of micelle accumulation in the liver and other organs of the reticuloendothelial system show a size-dependency; late-stage liver clearance is observed for the elongated morphology. However, further studies using nondegradable elongated micelles of different stiffnesses, and therefore persistence lengths, are necessary for further clarifying the aspect of morphology related to biodistribution and circulation time.

Discussion

Preclinical molecular imaging, SPECT in particular, is among the most effective ways to investigate the function of organs or dynamics of physiological processes *in vivo*. Information obtained with this imaging modality can be used either to expand the knowledge about the physiology of bioprocesses/disease or as a “screening” tool during the development and optimization of new translational therapies. Thus, the list of possible imaging applications of preclinical SPECT includes a wide range of γ -emitting isotopes (e.g., ^{125}I – 27 keV, $^{99\text{m}}\text{Tc}$ – 140 keV, ^{111}In – 170/245 keV), study durations (seconds to weeks), and preferable tracer activity levels. Subsequently, it is beneficial to have a highly versatile SPECT system without sacrificing imaging performance for a specific task. In the following paragraphs, we will discuss current

challenges in preclinical SPECT and our view on future developments of this imaging modality.

Due to the small size of the laboratory animals, high resolution and sensitivity will likely always be at the top of the performance requirements list for preclinical SPECT. Resolution-sensitivity trade-off of multi-pinhole collimators can allow reaching a “moderate” resolution/sensitivity level simultaneously. However, either resolution or sensitivity must be prioritized to answer specific research questions that require either the highest level of detail (e.g., neuroscience) or the lowest tracer activity (e.g., development of radiopharmaceuticals).

For general imaging applications (e.g., screening), SPECT should be able to resolve effectively the same level of detail in animals as we see in humans. This sets the target spatial resolution at ~0.5 mm, a resolution that multiple preclinical systems reached nearly a decade ago. Thus, the current challenges in the general applications of SPECT are likely more related to the degradation of image quality and quantification accuracy during imaging with high-/low-energy isotopes rather than its resolution/sensitivity characteristics.

Nearly 90% of all SPECT scans are performed with the isotope ^{99m}Tc . Therefore, system modeling, image reconstruction and collimator geometries of scanners are predominantly optimized for imaging with 140 keV photons emitted by ^{99m}Tc . However, various fields of translational research use alternative SPECT isotopes (^{111}In –nanomedicine, $^{125}\text{I}/^{123}\text{I}/^{131}\text{I}$ –radioisotope therapy development) with γ -photon energies significantly different from 140 keV. These increase quantification errors and degrade image quality. Both effects can be corrected for with appropriate modeling of the depth of interaction (DOI) in the gamma detector and energy-specific models of pinhole edge penetration. In the case of high-energy isotopes, it is also necessarily to use dedicated high-energy collimators (e.g., CMP [Goorden *et al.* 2013] or rotating slat collimation [van Holen *et al.* 2009]). Optimized image quality of high-energy SPECT with combined CMP collimation and energy-specific photon transport modeling was illustrated in chapter 3 of this thesis (^{131}I) and in the work of de Swart *et al.* 2015 (^{213}Bi). Similar approaches can be applied in the imaging of other high-energy isotopes. In the case of low energy isotopes, flexible DOI correction on already-acquired projection data or isotope-specific photon-transport modeling in the system matrix can be used for image quality optimization. In this combination, a flexible DOI correction method (e.g., projection-image-based) will allow for the optimization of image quality to any γ -photon energies. However, such a method has not been developed yet. Additionally, it will likely not allow compensation for more complex γ -photon energy-related effects, such as variable pinhole edge penetration and variable PSF

responses on the gamma detector. In contrast, isotope-specific photon transport modeling in the system matrix accurately models both effects. However, it requires generation of a separate system matrix for each required γ -photon energy. Possibly, a combination of these methods will increase the versatility of SPECT scanners by expanding the energy range of γ -photons that can be imaged quantitatively and at high resolution.

Some areas of translational research always require the highest possible level of detail in SPECT images. These areas include but are not limited to neuroscience, orthopedics and oncology, in which SPECT is commonly used in combination with high-resolution *ex vivo* methods (e.g., autoradiography). The co-registration of *in vivo* SPECT and autoradiography images is troublesome due to the destructive nature of the *ex vivo* method. Following the technical evaluation of high-resolution SPECT (chapter 2), we showed that the volumetric resolution of *in vivo* imaging already reaches approximately 0.015 μL (0.25 mm in plane). This value is ~ 5 times lower than the ~ 50 μm in-slice (0.5 μL volumetric) resolution of autoradiography. However, the resolution of SPECT can be further improved with higher focusing of multi-pinhole collimators or with higher magnification of the pinholes' projections on gamma detectors. Due to the finite animal size and already high focusing power of existing SPECT collimators, this approach will not provide a significant resolution gain *in vivo*. However, it might be able to provide autoradiography-like images for smaller *ex vivo* samples (e.g., brain). If developed, high-resolution *ex vivo* SPECT will eliminate all tissue sectioning-related challenges of autoradiography. Additionally, it will provide a direct link between lower resolution *in vivo* and high-resolution *ex vivo* images of the same animal.

Finally, some research fields are mainly interested in general biodistribution and pharmacokinetics of tracers and are not as dependent on spatial resolution of the images. These include the early stages of radiopharmaceutical and translational therapy developments, also some longitudinal studies. Here, preclinical SPECT is commonly replaced with optical imaging (OI). Partially, this is done due to the relatively low sensitivity, compared to OI, of the molecular imaging modality. However, poor tissue penetration of optical signals (~ 2 -3 mm) also limits OI, thus providing very superficial low-resolution (~ 1 cm) images lacking information on the internal 3D distribution of the compound. These drawbacks can be eliminated with high-sensitivity SPECT. In chapter 4 of this thesis, we showed that dedicated high-sensitivity collimator designs can significantly increase the sensitivity of SPECT without serious resolution loss in image resolution. Our results showed that 1.3% sensitivity ($^{99\text{m}}\text{Tc}$) and sub-mm resolution can be achieved simultaneously. Further optimization of multi-pinhole geometries [Rentmeester *et al.*

2007] should allow reaching ~30% sensitivity at approximately 5-mm resolution. If achieved, such a performance of SPECT will nearly eliminate the sensitivity-related gap between molecular and optical imaging. Additionally, this will significantly decrease tracer-related costs.

Chapter 8

Samenvatting & Discussie



Samenvatting van het proefschrift

Single Photon Emission Computed Tomography (SPECT) is een belangrijke beeldvormingsmodaliteit in preklinische beeldvorming van kleine proefdieren (bijvoorbeeld knaagdieren). Preklinische SPECT heeft het afgelopen decennium een snelle ontwikkeling doorgemaakt: nieuwe multi-pinhole collimator geometrieën, stationaire systeemontwerpen, data-acquisitie vormen, verbeterde systeemkalibraties en systeemmodellerings-, dempings- en verstrooiingscorrectiemethoden, als ook nieuwe beeldreconstructie-algoritmen hebben routineuze hoge-resolutie, dynamische en accurate kwantitatieve *in vivo* SPECT-beeldvorming van knaagdieren mogelijk gemaakt. Dit proefschrift beschrijft de evaluatie van enkele recente technische SPECT-instrumentatie ontwikkelingen, en focust op de ontwikkeling van spatiale resolutie, systeemgevoeligheid en haalbaarheid van beeldvorming met isotopen die hoogenergetische gammafotonen uitzenden.

De kleine afmetingen van dieren gebruikt in preklinisch onderzoek brengt enorme uitdagingen met zich mee voor de afbeeldingsresolutie vereist om de traceropname op intra-tumor of op sub-orgaan niveau te kunnen onderscheiden. In **Hoofdstuk 2** van dit proefschrift, valideren we de verbetering van de prestatie van de laatste generatie van U-SPECT-systemen (U-SPECT⁺) met een collimator met 0.25 mm pinholes. Gebruikmakend van fantoomstudies, laten we zien dat deze collimator het mogelijk maakt kwantitatieve scans uit te voeren van moleculaire opname in structuren tot kleiner dan een kwart millimeter, corresponderend met ongeveer een 0.015 μL volume resolutie. Dit is significant beter dan kon worden bereikt met eerder versies van U-SPECT (0.04 μL) of PET (VECTor: 0.4 μL), dus dit zou partiele-volume-effect gerelateerde fouten in kwantificatie van SPECT moeten verminderen. Bovendien, het niveau van details dat onze resultaten hebben laten zien in *in vivo* bot-SPECT van gewrichten (bijvoorbeeld de zichtbaarheid van kleine structuren zoals het femur epicondyle sulcus), kan nieuwe beeldvormingstoepassingen mogelijk maken in bijvoorbeeld orthopedisch onderzoek, en in sommige gevallen, zou toestaan om *ex vivo* methoden, zoals autoradiografie, te vervangen door hoge resolutie *in vivo* beeldvorming.

De mogelijkheid tot het uitvoeren van hoge resolutie en kwantitatieve SPECT-beeldvorming van de gecombineerde γ - en β -uitzendende isotoop ^{131}I is cruciaal voor de ontwikkeling van nieuwe kankertherapieën. Echter, preklinische beeldvorming van dit isotoop is uitdagend door de relatief hoge energie van ^{131}I gamma-fotonen (364 keV), welke makkelijk de collimatorwand en pinholeranden penetreren. Dit degradeert de resolutie als standaard SPECT-collimators

gebruikt zouden worden. Een specifieke geclusterde multi-pinhole collimator, die in onze groep was ontwikkeld, heeft verminderde randpenetratie. Evaluatie van deze collimator voor ^{131}I beeldvorming is het onderwerp van **Hoofdstuk 3**. Hiervoor, hebben we eerst de modellering van fotontransport verbeterd voor de iteratieve beeldreconstructie van 364 keV fotonen. Vervolgens, is de kwantitatieve accuraatheid en resolutie van ^{131}I -SPECT geëvalueerd met meerdere fantomen, terwijl *in vivo* beeldvormingsprestaties werden geïllustreerd met meerder statische en dynamische ^{131}I -Natrium jodide (NaI) SPECT/CT-scans van muizen. Ons resultaat laat goede kwantitatieve beeldaccuraatheid zien en een gereconstrueerde beeldresolutie van minder dan 0.6 mm. Dit biedt een mogelijkheid om ^{131}I opname/bio-distributie binnenin kleine organen in muizen te kwantificeren, en de dier-specifieke *in vivo* 3D dosisdistributie te berekenen. Beiden kunnen erg waardevol zijn voor de ontwikkeling van gerichte ^{131}I kankertherapieën.

Het kiezen van de goede balans tussen resolutie en gevoeligheid voor de voorliggende taak kan een uitdaging zijn in preklinische SPECT. De kleine afmetingen van de dieren die afgebeeld worden met preklinische scanners heeft de focus van SPECT-ontwikkeling in het laatste decennium geplaatst op resolutie verbeteringen. Als gevolg, komt de gevoeligheid van moderne multi-pinholecollimator systemen zelden boven de 0.2% uit, terwijl veel SPECT-beeldvormingstoepassingen (bv. longitudinale beeldvorming, tracer ontwikkeling) zouden kunnen profiteren van hogere gevoeligheid in SPECT. In **Hoofdstuk 4** ontwikkelen we een specifieke ultra-hoge-gevoeligheid pinhole SPECT-collimator met een 1.3% piek gevoeligheid, die nog steeds een gereconstrueerde resolutie van 0.85 mm kan halen voor $^{99\text{m}}\text{Tc}$. De dierenscans die in dit hoofdstuk worden gepresenteerd illustreren de mogelijkheid om of ultrasnelle dynamische SPECT-scans met 1 s tijdsegmenten, of SPECT-scans met minuscule hoeveelheden activiteit (fracties van MBq) uit te voeren. Gebaseerd op zijn prestaties, kan de collimator ook gebruikt worden voor het reduceren van de dierendosis gedurende opvolgende moleculaire beeldvormingsstudies ofvoor het verbeteren van de beeldsnelheid gedurende de beeldvorming van biologische processen met snelle dynamiek. Bovendien kan het de mogelijke toepasbaarheid verhogen, bijvoorbeeld voor beeldvorming van organen met lage specifieke opname of beeldvorming met tracers en nanodragers met een lage labelingefficiëntie.

Het gebruik van op nanodrager gebaseerde farmaceutica, inclusief polymeren, micellen en nanodeeltjes, is in het bijzonder veel belovend in oncologie. De lekkende vaten van tumoren en de verzwakte lymfatische drainage staan toe een hoge medicijnaccumulatie en retentie te bereiken via het EPR-effect. Dit effect hangt sterk af van de bloedcirculatielijd en de algemene biodistributie van de dragers. Dus, longitudinale biodistributiestudies spelen een belangrijke

rol gedurende de preklinische evaluatie van nieuwe nanodragers (bv nanomedicijnen). Desalniettemin, door de hoge initiële nierzuivering en de lange bloedcirculatietijden van de dragers is de beeldvorming van hun longitudinale biodistributie een uitdaging voor de gevoeligheid van SPECT-systemen, en dus wordt het in het algemeen vervangen door *ex vivo* methoden. In **Hoofdstuk 5** en **Hoofdstuk 6**, laten we twee toepassingen zien, die mogelijk zijn gemaakt door de collimator ontwikkeld in hoofdstuk 4, van longitudinale lage-dosis SPECT-beeldvorming voor polymerische nanodragers.

In hoofdstuk 5, bestudeerden we de invloed van verschillende poly(ethyleenoxide) (PEO) bloklengtes en aggregatietoestanden (unimeren tegenover micellen) op de biodistributie van Pluronic-nanodragers. De *in vivo* biodistributie van ^{111}In -geradiolabelde nanodragers was uitgevoerd in gezonde muizen met longitudinale (tot 48 uren na injectie) SPECT/CT-scans. Deze aanpak elimineert de terugkerende beperking geassocieerd met de dynamische natuur van copolymeer-micellen en staat ons toe om eenzelfde concentratie te gebruiken van beiden typen nanodragers. Onze resultaten laten zien dat door variëren van de PEO-bloklengte en aggregatietoestanden van de copolymeren verschillende nier- en leverzuiveringen worden behaald. De uitkomsten van dit werk kunnen gunstig zijn voor een meer rationele ontwikkeling van Pluronic-gebaseerde nanodragers en voor de toekomst van EPR gebaseerde kankertherapieën.

In hoofdstuk 6, gebruikten we SPECT voor het onderzoeken van de circulatie, biodistributie en zuivering van rigide model polystyreen-b-poly(ethyleenoxide) nanodragers met sferische en cilindrische morfologie. Dit was gedaan om een completer beeld te verkrijgen van de effecten van grootte en rigiditeit op het *in vivo* gedrag van de dragers. De glasachtige natuur van polystyreen garandeert de morfologische stabiliteit van de dragers *in vivo*, en door inkapseling van ^{111}In in hun kernen, kan een beoordeling van de longitudinale *in vivo* biodistributie van de deeltjes in gezonde muizen uitgevoerd worden met lage-dosis SPECT-beeldvorming (tot minder dan 0.26 MBq/dier activiteit). Onze resultaten laten verlengde bloedcirculatie zien van meer dan 24 uur voor alle micel morfologiën die bestudeerd zijn, terwijl de dynamiek van micelaccumulatie in de lever en andere organen van het reticuloendotheelsysteem een grootte afhankelijkheid laten zien. Laat-stadium leverzuivering is geobserveerd voor de uitgerekte morfologie. Echter, verdere studies met niet-afbreekbare uitgerekte micellen van verschillende stijfheden, en daarmee blijvende lengtes, zijn nodig voor verdere verduidelijking van het aspect van morfologie gerelateerd aan biodistributie en circulatietijd.

Discussie

Preklinische moleculaire beeldvorming, en SPECT in het bijzonder, hoort bij de meest effectieve manieren om te onderzoeken wat de functies van organen of wat de dynamieken van fysiologische processen *in vivo* zijn. Informatie verkregen met deze beeldvormingsmodaliteit kan gebruikt worden voor het uitbreiden van de kennis over de fysiologie van bioprocessen/ziekten of als een “screening” gereedschap gedurende de ontwikkeling en optimalisatie van nieuwe translationele therapieën. Dus, de lijst van mogelijke beeldvormingstoepassingen van preklinische SPECT bevat een breed scala van γ -emitterende isotopen (bijvoorbeeld ^{125}I - 27 keV, $^{99\text{m}}\text{Tc}$ - 140 keV, ^{111}In - 170/245 keV), studie duren (seconden tot weken), en wenselijke traceractiviteitsniveaus. Vervolgens, is het nuttig om een erg veelzijdig SPECT-systeem te hebben, zonder hiervoor de beeldvormingsprestaties voor een specifieke taak op te offeren. In de volgende alinea's, willen we de huidige uitdagingen in preklinische SPECT en onze visie op toekomstige ontwikkelingen van deze beeldvormingsmodaliteit bediscussiëren.

Door de kleine afmetingen van proefdieren, zullen hoge resolutie en gevoeligheid waarschijnlijk altijd bovenaan de lijst van prestatie-eisen van preklinische SPECT staan. De resolutie-gevoeligheidsbalans van multi-pinhole collimators kan het mogelijk maken tegelijkertijd een “gematigd” resolutie/gevoeligheidsniveau te bereiken. Echter, of de resolutie of de gevoeligheid moet worden verkozen voor het beantwoorden van erg specifieke onderzoeksvragen die of de hoogste detailniveaus (bv. neurowetenschappen) of de laagste traceractiviteit (bv. ontwikkeling van radiofarmaceutica) vereisen.

Voor algemene beeldvormingstoepassingen (bv. screening), zou SPECT in staat moeten zijn om effectief hetzelfde detailniveau in dieren en in mensen te kunnen onderscheiden. Dit zet het doel voor de spatiale resolutie op ~ 0.5 mm, een resolutie die bijna een decennium geleden al was bereikt door meerdere preklinische systemen. Dus de huidige uitdagingen in algemene toepassingen van SPECT zijn waarschijnlijk meer gerelateerd aan de degradatie van beeldkwaliteit en kwantificatienauwkeurigheid gedurende beeldvorming van hoog-/laag-energetische isotopen, en niet aan zijn resolutie/gevoeligheid karakteristieken.

Bijna 90% van alle SPECT-scans worden uitgevoerd met de isotoop $^{99\text{m}}\text{Tc}$. Daarom worden systeemmodellering, beeldreconstructie en collimatorgeometrieën vooral geoptimaliseerd voor beeldvorming met 140 keV-fotonen uitgezonden door $^{99\text{m}}\text{Tc}$. Echter, verschillende vakgebieden in translationeel onderzoek gebruiken alternatieve SPECT-isotopen (^{111}In -nanomedicijn,

$^{125}\text{I}/^{123}\text{I}/^{131}\text{I}$ -radioisotoop therapie-ontwikkeling) met γ -fotonenergieën die significant afwijken van 140 keV. Deze vergroten kwantificatiefouten en degraderen de beeldkwaliteit. Beide effecten kunnen worden gecorrigeerd met passende modelering van de diepte-van-interactie (DOI) in de gammadetector en energie specifieke modellen van pinholerandpenetratie. In het geval van hoogenergetische isotopen, is het ook noodzakelijk om gebruik te maken van speciale hoge-energie collimators (bv. [Goorden *et al.* 2013] of draaiende lamel collimatie [van Holen *et al.* 2009]). Geoptimaliseerde beeldkwaliteit van hoge-energie SPECT met gecombineerde CMP collimatie en energie-specifieke fotontransportmodellering was geïllustreerd in hoofdstuk 3 van dit proefschrift (^{131}I) en in het werk van de Swart *et al.* 2015 (^{213}Bi). Vergelijkbare aanpakken kunnen worden toegepast op de beeldvorming van andere hoge-energie isotopen. In het geval van lage-energie isotopen, kan flexibele DOI-correctie op al verkregen projectie data of isotoop-specifieke fotontransportmodellering in de systeemmatrix gebruikt worden voor beeldkwaliteitsoptimalisatie. In deze combinatie, zullen flexibele DOI-correctiemethoden (bv. projectiebeeld gebaseerd) toestaan om de beeldkwaliteit te optimaliseren voor elke γ -fotonenergie. Echter, een dergelijk methode is nog niet ontwikkeld. Bovendien, zal het waarschijnlijk niet kunnen compenseren voor meer complexe γ -fotonenergie gerelateerde effecten, zoals de variabele pinholerandpenetratie en verschillende PSF-reactie op de gammadetector. Daarentegen modelleert isotoop-specifieke fotontransportmodellering in de systeemmatrix beide effecten accuraat. Echter, het vereist het generen van aparte systeemmatrices voor elke vereiste γ -fotonenergie. Een combinatie van deze methoden zal de veelzijdigheid van SPECT-scanners vergroten, door het uitbreiden van het energiebereik van de γ -fotonen die kwantitatief en met een hoge resolutie afgebeeld kunnen worden.

Sommige gebieden van translationeel onderzoek zullen altijd het hoogst mogelijke detailniveau eisen in SPECT-beelden. Deze gebieden zijn onder andere maar niet beperkt tot neurowetenschappen, orthopedie en oncologie, waar SPECT algemeen gebruikt wordt in combinatie met hoge-resolutie *ex vivo* methoden (bv. autoradiografie). Co-registratie van *in vivo* SPECT en autoradiografie beelden is moeizaam door de destructieve natuur van de *ex vivo* methode. Na technische evaluatie van hoge resolutie SPECT (hoofdstuk 2), lieten we zien dat de volumetrische resolutie van *in vivo* beeldvorming al ongeveer tot 0.015 μL (0.25 mm in het vlak) reikt. Deze waarde is ~ 5 keer lager dan de ~ 50 μm in-slice (0.5 μL volumetrisch) resolutie van autoradiografie. Echter, de resolutie van SPECT kan verder verbeterd worden met meer focussen van de multi-pinhole collimators of met hogere vergroting van de pinholeprojecties op de gammadetector. Door de eindige diergrootte en al hoge focus kracht van huidige SPECT-collimators, zal deze aanpak *in vivo* niet tot significante resolutie verbeteringen leiden. Echter,

het kan mogelijk zijn autoradiografisch-achtige beelden van kleine *ex vivo* monsters (bv. brein) te verschaffen. Indien ontwikkeld, zal hoge-resolutie *ex vivo* SPECT alle weefsel-snij gerelateerde uitdagingen van autoradiografie elimineren. Bovendien, zal het een directe link leggen tussen de lage resolutie *in vivo* en hoge resolutie *ex vivo* beelden van hetzelfde dier.

Ten slotte, zijn sommige onderzoeksgebieden vooral geïnteresseerd in de algemene biodistributie en farmokinetiek van tracers en niet zo afhankelijk van de spatiele resolutie van beelden. Deze gebieden omvatten zowel vroege stadia van radiofarmaceutica en translationele therapie ontwikkeling als longitudinale studies. Hier is preklinische SPECT vaak vervangen door optische beeldvorming (OI). Gedeeltelijk, is dit vanwege de relatief lage gevoeligheid, vergeleken met OI, van de moleculaire beeldvormingsmodaliteit. Echter, OI is ook beperkt door de slechte weefselpenetratie van optische signalen (~2-3 mm), wat erg oppervlakkige lage-resolutie (~1 cm) plaatjes oplevert zonder informatie over de interne 3D distributie van de verbinding. Deze nadelen kunnen worden geëlimineerd met hoge-gevoeligheid SPECT. In hoofdstuk 4 van dit proefschrift laten we zien dat specifieke hoge-gevoeligheid collimatorontwerpen de gevoeligheid van SPECT significant kunnen verhogen zonder serieus verlies van beeldresolutie. Onze resultaten laten zien dat 1.3% gevoeligheid (^{99m}Tc) en sub-mm resolutie tegelijk haalbaar zijn. Verdere optimalisatie van multi-pinhole geometrieën [Rentmeester *et al.* 2007] zou het mogelijk moeten maken om een gevoeligheid van ~30% te bereiken bij ongeveer 5 mm resolutie. Indien behaald, zou die prestatie van SPECT het gevoeligheid-gerelateerde gat tussen moleculaire en optische beeldvormingen bijna elimineren. Bovendien, zal dit de tracer gerelateerde kosten significant verlagen.

References

- Allen C, *et al.* Nano-engineering block copolymer aggregates for drug delivery. *Colloids Surfaces B Biointerfaces*. 1999; 16(3).
- Allen TM, *et al.* Drug delivery systems: entering the mainstream. *Science*. 2004; 303, 1818.
- Adatepe MH, *et al.* Red cell and plasma protein labeling with ^{113m}In . *Int J Appl Radiat Is*. 1971; 22(8):498-501.
- Alexandridis P, *et al.* Colloids Surf A Physicochem Eng Asp. 1995. 96; (1–2):1-46.
- Amundson SA, *et al.* Differential response of stress genes on low dose-rate γ -radiation. *Mol Cancer Res*. 2003; 1(3).
- Anger HO. Scintillation Camera. *Rev Sci Instrum*. 1958; 29:27.
- Anselmo AC, *et al.* Elasticity of nanoparticles influences their blood circulation, phagocytosis, endocytosis, and targeting. *ACS Nano*. 2015; 9:3169-3177.
- Arranja A, *et al.* Cytotoxicity and internalization of Pluronic micelles stabilized by core cross-linking. *J Control Release*. 2014; 13:87-95.
- Arvizo RR, *et al.* Modulating pharmacokinetics, tumor uptake and biodistribution by engineered nanoparticles. *PLoS One*. 2011; 6(3).
- Batrakova EV, *et al.* Distribution kinetics of a micelle-forming block copolymer Pluronic P85. *J Control Release*. 2004; 100(3):389-397.
- Beekman FJ, *et al.* Towards *in vivo* nuclear microscopy: iodine-125 imaging in mice using micro-pinholes. *Eur J Nucl Med Mol Imaging*. 2002; 29(7):933-8.
- Beekman FJ, *et al.* U-SPECT-I: a novel system for submillimeter-resolution tomography with radiolabeled molecules in mice. *J Nucl Med*. 2005; 46(7):1194-200.
- Beekman FJ, *et al.* The pinhole: gateway to ultra-high-resolution three-dimensional radionuclide imaging. *Eur J Nucl Med Mol Imaging*. 2007; 34(2):151-61.
- Befera NT, *et al.* Comparison of 4D-microSPECT and microCT for murine cardiac function. *Mol Imaging Biol*. 2014; 16(2):235-45.
- Bertrand N, *et al.* The journey of a drug-carrier in the body: an anatomo-physiological perspective. *J Control Release*. 2012; 161(2):152-163.
- Bhattacharjee J, *et al.* Microstructure, drug binding and cytotoxicity of Pluronic P123-aerosol OT mixed micelles. *RSC Adv*. 2013; 3(45):23080-23089.
- Branderhorst W, *et al.* Pixel-based subsets for rapid multi-pinhole SPECT reconstruction. *Phys Med Biol*. 2010; 55(7):2023-34.
- Branderhorst W, *et al.* Targeted multi-pinhole SPECT. *Eur J Nucl Med Mol Imaging*. 2011;

38(3):552-61.

Branderhorst W, *et al.* Three-dimensional histologic validation of high-resolution SPECT of antibody distributions within xenografts. *J Nucl Med.* 2014; 55(5):830-7.

Brandt MP, *et al.* Micro-single-photon emission computer tomography image acquisition and quantification of sodium-iodide symporter-mediated radionuclide accumulation in mouse thyroid and salivary glands. *Thyroid.* 2012; 22(6):617-624.

Brinkhuis RP, *et al.* Size dependent biodistribution and SPECT imaging of (111)In-labeled polymersomes. *Bioconjug Chem.* 2012; 23(5):958-65.

Brom M, *et al.* Improved labelling of DTPA- and DOTA-conjugated peptides and antibodies with ¹¹¹In in HEPES and MES buffer. *EJNMMI Res.* 2012; 2(4).

Buck AK, *et al.* SPECT/CT. *J Nucl Med.* 2008; 49(8):1305-1319.

Champion JA, *et al.* Role of target geometry in phagocytosis. *Proc Natl Acad Sci USA.* 2006; 103: 4930.

Chen ZN, *et al.* Targeting radioimmunotherapy of hepatocellular carcinoma with iodine (131I) metuximab injection: clinical phase I/II trials. *Int J Radiat Oncol Biol Phys.* 2006; 65(2):435-444.

Cherry SR. Multimodality *in vivo* imaging systems: twice the power or double the trouble. *Annu Rev Biomed Eng.* 2006; 8:35-62.

Cherry SR, *et al.* Physics in nuclear medicine 2e. 2012; Elsevier Inc., Philadelphia.

Cheson BD, *et al.* Monoclonal antibody therapy for B-Cell non-Hodgkin's lymphoma. *N Engl J Med.* 2008; 359:613-626.

Christian D, *et al.* Flexible filaments for *in vivo* imaging and delivery: persistent circulation of filomecelles opens the dosage window for sustained tumor shrinkage. *Mol Pharm.* 2009; 6(5):1343-52.

Copeland DE, *et al.* Pinhole camera for γ -ray sources. *Nucleonics.* 1949; 5(2):44-49.

Decuzzi P, *et al.* The adhesive strength of non-spherical particles mediated by specific interactions. *Biomaterials.* 2006; 27(30):5307-14.

Demoy M, *et al.* Spleen capture of nanoparticles: influence of animal species and surface characteristics. *Pharm Res.* 1999; 16(1):37-41.

D'Addio SM, *et al.* Effects of block copolymer properties on nanocarrier protection from *in vivo* clearance. *J Control Release.* 2012; 162(1):208-17.

Deleye S, *et al.* Performance evaluation of small-animal multipinhole μ SPECT scanners for mouse imaging. *Eur J Nucl Med Mol Imaging.* 2013; 40(5):744-58.

Demoy M, *et al.* Spleen capture of nanoparticles: influence of animal species and surface characteristics. *Pharm Res.* 1999; 16: 37-41.

- de Swart J, *et al.* Utilizing high-energy gamma photons for high-resolution ^{213}Bi SPECT in mice. *J Nucl Med.* 2015; 57(3):486-92.
- Dewaraja YK, *et al.* Characterization of Scatter and Penetration Using Monte Carlo Simulation ^{131}I Imaging. *J Nucl Med.* 2000; 41(1):123-130.
- Doshi N, *et al.* Macrophages recognize size and shape of their targets. *PLoS One.* 2010; 5(1).
- Dou S, *et al.* Intraperitoneal injection is not always suitable alternative for intravenous injection for radiotherapy. *Cancer Biother Radiopharm.* 2013; 28(3):335-42.
- Duan X, *et al.* Physicochemical characteristics of nanoparticles affect circulation, biodistribution, cellular internalization, and trafficking. *Small.* 2013; 9(9-10):1521-1532.
- Duncan R, *et al.* Nanomedicine(s) under the microscope. *Mol Pharm.* 2011; 8(6): 2101-2141.
- Dvorak HF, *et al.* Vascular permeability factor/vascular endothelial growth factor and the significance of microvascular hyperpermeability in angiogenesis. *Curr Top Microbiol Immunol.* 1999, 237, 97.
- Fan Q, *et al.* Biological Evaluation of ^{131}I - and CF750-Labeled Dmab(scFv)-Fc Antibodies for Xenograft Imaging of CD25-Positive Tumors. *BioMed Research International.* 2014.
- Finucane CM, *et al.* Quantitative accuracy of low-count SPECT imaging in phantom and *in vivo* mouse studies. *Int J Mol Imaging.* 2011; 2011:1-8.
- Franken PR, *et al.* Distribution and dynamics of $^{99\text{m}}\text{Tc}$ -Pertechnetate uptake in the thyroid and other organs assessed by single-photon emission computed tomography in living mice. *Thyroid.* 2010; 20(5):519-526.
- Furenlid LR, *et al.* FastSPECTII: A Second-Generation High-Resolution Dynamic SPECT Imager. *IEEE Trans Nucl Sci.* 2004; 51(3):631-635.
- Funk T, *et al.* Radiation dose estimation in small animal SPECT and PET. *Med Phys.* 2004; 31(9):2680-6.
- Geng Y, *et al.* Shape effects of filaments versus spherical particles in flow and drug delivery. *Nat Nanotechnol.* 2007; 2:249-255.
- Geng Y, *et al.* Hydrolytic degradation of poly(ethylene oxide)-block-polycaprolactone worm micelles. *J Am Chem Soc.* 2005; 127(37):12780-1.
- Goorden MC, *et al.* An efficient simulator for pinhole imaging of PET isotopes. *Phys Med Biol.* 2011; 56(6):1617-34.
- Goorden MC, *et al.* Optimizing modeling in iterative image reconstruction for preclinical pinhole PET. *Phys Med Biol.* 2016; 61(10):3712-3733.
- Goorden MC, *et al.* VECTor: a preclinical imaging system for simultaneous submillimeter SPECT and PET. *J Nucl Med.* 2013; 54(2):306-12.
- Gopal AK, *et al.* High-dose ^{131}I tositumomab (anti-CD20) radioimmunotherapy and

- autologous hematopoietic stem-cell transplantation for adults ≥ 60 years old with relapsed or refractory B-cell lymphoma. *J Clin Oncol*. 2007; 25(11):1396-1402.
- Grindel JM, *et al*. Distribution, metabolism, and excretion of a novel surface-active agent, purified poloxamer 188, in rats, dogs, and humans. *J Pharm Sci*. 2002; 91(9):1936-1947.
- Harrington KJ, *et al*. Biodistribution and pharmacokinetics of ^{111}In -DTPA-labelled pegylated liposomes in a human tumour xenograft model: implications for novel targeting strategies. *Br J Cancer*. 2000; 83(2):232-8.
- He C, *et al*. Effects of particle size and surface charge on cellular uptake and biodistribution of polymeric nanoparticles. *Biomaterials*. 2010; 31(13):3657-3666.
- Hnatowich DJ, *et al*. Label stability in serum of four radionuclides on DTPA-coupled antibodies—An evaluation. *Int J Rad Appl Instrum B*. 1986; 13(4):353-358.
- Hoang B, *et al*. Noninvasive monitoring of the fate of ^{111}In -Labeled block copolymer micelles by high resolution and high sensitivity microSPECT/CT Imaging. *Mol Pharm*. 2009; 6(2):581-592.
- Holmberg H, *et al*. Impact of blood sampling technique on blood quality and animal welfare in haemophilic mice. *Lab Anim*. 2011; 45:114-120.
- Hosain F, *et al*. Binding of trace amounts of ionic indium-113m to plasma transferrin. *Clin Chim Acta*. 1969; 24(1):69-75.
- Hudson HM, *et al*. Accelerated image-reconstruction using ordered subsets of projection data. *IEEE Trans Med Imag*. 1994; 13(4):601-609.
- Hwang AB, *et al*. Assessment of the sources of error affecting the quantitative accuracy of SPECT imaging in small animals. *Phys Med Biol*. 2008; 53(9):2233-2252.
- Ivashchenko O, *et al*. Quarter-millimeter-resolution molecular mouse imaging with U-SPECT⁺. *Mol Imaging*. 2014;13.
- Ivashchenko O, *et al*. Ultra-high-sensitivity submillimeter mouse SPECT. *J Nucl Med*. 2015; 56(3):470-475.
- Jain S, *et al*. Consequences of nenorgodicity in aqueous binary PEO-PB micellar dispersion. *Macromolecules*. 2004; 37:1511.
- Jaszczak RJ, *et al*. Pinhole collimation for ultra-high-resolution, small-field-of-view SPECT. *Phys Med Biol*. 1994; 39(3):425-37.
- Jennings L, *et al*. *In vivo* biodistribution of stable spherical and filamentous micelles probed by high-sensitivity SPECT. *Biomater Sci*. 2016; 4(8):1202-11.
- Jouret F, *et al*. Single photon emission-computer tomography (SPECT) for functional investigation of the proximal tubule in conscious mice. *Am J Physiol Renal Physiol*. 2010; 298(2):F454-60.

- Jia G, *et al.* Cytotoxicity of carbon nanomaterials: single-wall nanotube, multi-wall nanotube, and fullerene. *Environ Sci Technol.* 2005; 39(5): 1378-83.
- Kaminski MS, *et al.* Radioimmunotherapy with I-131 tositumomab for relapsed or refractory B-cell non-Hodgkin lymphoma: updated results and long-term follow-up of the University Michigan experiment. *Blood.* 2000; 96(4):1259-1266.
- Kaminski MS, *et al.* Pivotal study of iodine I-131 Tositumomab for chemotherapy-refractory low-grade or transformed low-grade B-cell non-Hodgkin's lymphomas. *J Clin Oncol.* 2001; 19(19):3918-3928.
- Kaminski MS, *et al.* I-131-tositumomab as initial treatment for follicular lymphoma. *N Engl J Med.* 2005; 352(5):441-449.
- King MA, *et al.* Emission tomography: the fundamentals of PET and SPECT. London: Elsevier Academic; 2004:473-498.
- Klibanov AL, *et al.* Amphiphathic polyethyleneglycols effectively prolong the circulation time of liposomes. *FEBS Lett.* 1990; 268(1):235-237.
- Kolhar P, *et al.* Using shape effects to target antibody-coated nanoparticles to lung and brain endothelium. *Proc Natl Acad Sci U S A.* 2013; 110:10753.
- Kowalsky RJ, *et al.* Radiopharmaceuticals in Nuclear Pharmacy and Nuclear Medicine (3rd edition). American Pharmacists Association. 2011.
- Kreyling WG, *et al.* *In vivo* integrity of polymer-coated gold nanoparticles. *Nat Nano.* 2015; 10(7): 619-623.
- Kummitha CM, *et al.* Relating tissue/organ energy expenditure to metabolic fluxes in mouse and human: experimental data integrated with mathematical modeling. *Physiol Rep.* 2014; 2(9):e12159.
- Kutscher HL, *et al.* Threshold size for optimal passive pulmonary targeting and retention of rigid microparticles in rats. *J Controlled Release.* 2010; 143(1):31-7.
- Kupinski MA, Barrett HH. Small-animal SPECT imaging. Springer. 2005.
- Laan AC, *et al.* Radiolabeling polymeric micelles for *in vivo* evaluation: a novel, fast, and facile method. *EJNMMI Res.* 2016; 6(12).
- Lammers T, *et al.* Tumour-targeted nanomedicines: principles and practice. *Br J Cancer.* 2008; 99(3): 392-397.
- Lange K, *et al.* EM reconstruction algorithms for emission and transmission tomography. *J Comput Assist Tomogr.* 1984; 8:306-316.
- Liu Z, *et al.* Circulation and long-term fate of functionalized biocompatible single-walled carbon nanotubes in mice probed by Raman spectroscopy. *Proc Nat Acad Sci USA.* 2008; 105:1410.
- Lu HF, *et al.* Galactosylated PVDF membrane promotes hepatocyte attachment and functional

- maintenance. *Biomaterials*. 2003; 24(27):4893-903.
- Lub-de Hooge MN, *et al.* Preclinical characterisation of (111)In-DTPA-trastuzumab. *Br J Pharmacol*. 2004; 143(1):99-106.
- Madsen MT. Recent advances in SPECT imaging. *J Nucl Med*. 2007; 48(4):661-673.
- Maeda H, *et al.* Tumor vascular permeability and the EPR effect in macromolecular therapeutics: a review. *J Control Release*. 2000; 65(1-2):271-84.
- Maeda H, *et al.* The enhanced permeability and retention (EPR) effect in tumor vasculature: the key role of tumor-selective macromolecular drug targeting. *Adv Enzyme Regul*. 2001; 41:189-207.
- Mahmud A, *et al.* The effect of block copolymer structure on the internalization of polymeric micelles by human breast cancer cells. *Colloids Surf B Biointerfaces*. 2005; 45(2):82-89.
- Mallard JR, Myers MJ. The performance of a gamma camera for visualization of radioactive isotopes *in vivo*. *Phys Med Biol*. 1963; 8(2):165-182.
- Marsee DK, *et al.* Imaging of metastatic pulmonary tumors following NIS gene transfer using single photon emission computer tomography. *Cancer Gene Ther*. 2004; 11(2):121-127.
- Matsushima H, *et al.* *In vivo* behavior of ¹¹¹In-DTPA in rat and mouse after intra-ventricular administration. *Radioisotopes*. 1977; 26(11):784-9.
- McFarlane AS. Labelling of plasma proteins with radioactive iodine. *Biochem J*. 1956; 62(1):135-143.
- Melis M, *et al.* Dynamic and static small-animal SPECT in rats for monitoring renal function after ¹⁷⁷Lu-labeled Tyr3-Octreotate radionuclide therapy. *J Nucl Med*. 2010; 51(12):1962-8.
- Miest TS, *et al.* Measles virus entry through the signalling lymphocyte activation molecule governs efficacy of mantle cell lymphoma radiovirotherapy. *Mol Ther*. 2013; 21(11):2019-31.
- Mikhail AS, *et al.* Image-based analysis of the size- and time-dependent penetration of polymeric micelles in multicellular tumor spheroids and tumor xenografts. *Int J Pharm*. 2014; 464(1-2):168-77.
- Mitchell GS, *et al.* A high-sensitivity small animal SPECT system. *Phys Med Biol*. 2009; 54(5):1291-305.
- Müllner M, *et al.* Size and rigidity of cylindrical polymer brushes dictate long circulating properties *in vivo*. *ACS Nano*. 2015; 9(2):1294-1304.
- Mitrofanova E, *et al.* Effective growth arrest of human colon cancer in mice using rat sodium iodine symporter and radioiodine therapy. *Hum Gene Ther*. 2005; 16(11):1333-7.
- Mok GS, *et al.* Quantification of the multiplexing effects in multi-pinhole small animal SPECT: a simulation study. *IEEE Trans Nucl Sci*. 2009; 56(5):2636-2643.
- Mok GS, *et al.* The effects of object activity distribution on multiplexing multi-pinhole SPECT.

Phys Med Biol. 2011; 56(8):2635-2650.

Mustonen T, *et al.* Endothelial receptor tyrosine kinases involved in angiogenesis. *J Cell Biol.* 1995; 129(4):895-8.

Nuyts J, *et al.* Small animal imaging with multi-pinhole SPECT. *Methods.* 2009; 48(2):83-91.

Ogawa K, *et al.* A practical method for positron-dependent Compton-scatter correction in single photon emission CT. *IEEE Trans Med Imaging.* 1991;10(3):408-12.

Ohtake Y, *et al.* The uptake of ^{111}In in the liver and bone marrow of partially hepatectomized and venesectioned rats. *Appl Radiat Isot.* 2008; 66(9): 1245-1249.

Patil RR, *et al.* Probing *in vivo* trafficking of polymer/DNA micellar nanoparticles using SPECT/CT imaging. *Mol Ther.* 2011; 19(9):1626-1635.

Penheiter AR, *et al.* Pinhole micro-SPECT/CT for noninvasive monitoring and quantitation of oncolytic virus dispersion and percent infection in solid tumors. *Gene Ther.* 2012; 19(3):279-87.

Penheiter AR, *et al.* The sodium iodide symporter (NIS) as an imaging reporter for gene, viral, and cell-based therapies. *Curr Gene Ther.* 2012, 12(1):33-47.

Powsner RA. Essential Nuclear Medicine Physics. 2nd ed. Blackwell Publishing. 2006. p. 163-6.

Qi J, *et al.* Iterative reconstruction techniques in emission computed tomography. *Phys Med Biol.* 2006; 51(15):R541-78.

Rault E, *et al.* Comparison of image quality of different iodine isotopes (I-123, I-124, and I-131). *Cancer Biother Radiopharm.* 2007; 22(3):423-30.

Rentmeester MC, *et al.* Optimizing multi-pinhole SPECT geometries using an analytical model. *Phys Med Biol.* 2007; 52(9):2567-81.

Rowe RK, *et al.* A stationary hemispherical SPECT imager for three-dimensional brain imaging. *J Nucl Med.* 1993; 34(3):474-80.

Sauer S, *et al.* Expression of oncofetal ED-B-containing fibronectin isoform in hematologic tumors enables ED-B-targeted ^{131}I -L19LIP radioimmunotherapy in Hodgkin lymphoma patients. *Blood.* 2009; 113(10):2265-2274.

Schramm NU, *et al.* High-resolution SPECT using multipinhole collimation. *IEEE Trans Nucl Sci.* 2003; 50(3).

Schipper ML, *et al.* Efficacy of $^{99\text{m}}\text{Tc}$ pertechnetate and ^{131}I radioisotope therapy in sodium/iodide symporter (NIS)-expressing neuroendocrine tumors expressing neuroendocrine tumors *in vivo*. *Eur J Nucl Med Mol Imaging.* 2007; 34:638-650.

Sgouros G, *et al.* Patient-specific dosimetry for ^{131}I thyroid cancer therapy using ^{124}I PET and 3-dimensional-internal dosimetry (3D-ID) software. *J Nucl Med.* 2004; 45(8):1366-1372.

Sfakianakis GN, *et al.* MAG3 SPECT: a rapid procedure to evaluate the renal parenchyma. *J*

Nucl Med. 1997; 38(3):478-83.

Shao A, *et al.* Far-Red and near-IR AIE-active fluorescent organic nanoprobe with enhanced tumor-targeting efficacy: shape-specific effect. *Angew Chem Int Ed.* 2015; 54:7275-7280.

Shepp LA, *et al.* Maximum likelihood reconstruction for emission tomography. *IEEE Trans Med Imag.* 1982; 1(2):113-22.

Smith MF, *et al.* Lead and tungsten pinhole inserts for I-131 SPECT tumor imaging: experimental measurements and photon transport simulations. *IEEE Trans Nucl Science.* 1997; 44(1):74-82.

Strand SE, *et al.* High resolution pinhole SPECT for tumor imaging. *Acta Oncologica.* 1993; 32(8):861-867.

Su M, *et al.* Temperature-sensitive nanoparticle-to-vesicle transition of ABC triblock copolymer corona-shell-core nanoparticles by seeded dispersion RAFT polymerization. *Macromolecules.* 2014; 47(4):1360-1370.

Sun X, *et al.* An assessment of the effects of shell cross-linked nanoparticle size, core composition, and surface PEGylation on *in vivo* biodistribution. *Biomacromolecules.* 2005; 6(5): 2541-54.

Talelli M, *et al.* Polymeric micelles for cancer therapy: 3 C's to enhance efficacy. *Curr Opin Solid State Mater Sci.* 2012; 16(6):302-309.

Tantawy MN, *et al.* Assessment of renal function in mice with unilateral ureteral obstruction using ^{99m}Tc-MAG3 dynamic scintigraphy. *BMC Neurol.* 2012; 13.

Tenney CR, *et al.* Uranium Pinhole Collimators for I-131 SPECT Imaging. *IEEE Trans Nucl Science.* 1999; 46(4):1165-1171.

Treuting PM, *et al.* Comparative anatomy and histology a mouse and a human atlas. Amsterdam: Elsevier; 2012:211-228.

Tsai P-P, *et al.* Effect of different blood collection methods on indicators of welfare in mice. *Lab Anim.* 2015; 44(8):301-310.

Tuy HK. An inversion formula for cone-beam reconstruction. *SIAM J Appl Math.* 1983; 43(3):546-552.

Vaissier PE, *et al.* Fast spiral SPECT with stationary γ -cameras and focusing pinholes. *J Nucl Med.* 2012; 53(8):1292-9.

Vaissier PEB, *et al.* Fast count-regulated OSEM reconstruction with adaptive resolution recovery. *IEEE Trans Med Imaging.* 2013; 32(12):2250-61.

van Audenhaege K, *et al.* The evaluation of data completeness and image quality in multiplexing multi-pinhole SPECT. *IEEE Trans Med Imag.* 2015; 34(2):474-86.

van der Have F, *et al.* Penetration, scatter and sensitivity in channel micro-pinholes for SPECT: a Monte Carlo investigation. *IEEE Trans Nucl Sci.* 2006; 53(5):2635-2645.

- van der Have F, *et al.* System calibration and statistical image reconstruction for ultra-high resolution stationary pinhole SPECT. *IEEE Trans Med Imaging.* 2008; 27(7):960-71.
- van der Have F, *et al.* U-SPECT-II: an ultra-high-resolution device for molecular small-animal imaging. *J Nucl Med.* 2009; 50(4):599-605.
- van Holen R, *et al.* SPECT imaging of high isotopes and isotopes with high energy contaminants with rotating slat collimators. *Med Phys.* 2009; 36(9):4257-67.
- van Zutphen LFM, *et al.* Principles of laboratory animal science, Revised edition. Amsterdam: Elsevier; 2001:317.
- Vastenhouw B, *et al.* Movies of dopamine transporter occupancy with ultra-high resolution focusing pinhole SPECT. *Mol Psychiatry.* 2007; 12(11):984-7.
- Vastenhouw B, *et al.* Submillimeter total-body murine imaging with U-SPECT-I. *J Nucl Med.* 2007; 48:487-493.
- Vunckx K, *et al.* Effect of overlapping projections on reconstruction image quality in multipinhole SPECT. *IEEE Trans Med Imag.* 2008; 27: 972-83.
- Wang ZY, *et al.* Disposition in rats of a polyoxypropylene-polyoxyethylene copolymer used in plasma fractionation. *Drug Metab Dispos.* 1975; 3(6):536-542.
- Wang YM, *et al.* Exchange of chains between micelles of labeled polystyrene-block-poly(oxyethylene) as monitored by nonradiative singlet energy transfer. *Macromolecules.* 1995; 28: 904.
- Weber DA, *et al.* Pinhole SPECT: an approach to *in vivo* high resolution SPECT imaging in small laboratory animals. *J Nucl Med.* 1994; 35(2):342-8.
- Weichert JP, *et al.* Alkylphosphocholine Analogs for Broad-Spectrum Cancer Imaging and Therapy. *Sci Transl Med.* 2014; 6(240):240ra75.
- Weissleder R, *et al.* Molecular Imaging: Principles and Practice. *PMPH.* 2010.
- Willcox ML, *et al.* A study of labeled pluronic F-68 after intravenous injection into the dog. *J Surg Res.* 1978; 25(4):349-356.
- Williams JP, *et al.* Animal models for medical countermeasures to radiation exposure. *Radiat Res.* 2010; 173(4):557-78.
- Wu C, *et al.* Absolute quantitative total-body small-animal SPECT with focusing pinholes. *Eur J Nucl Med Mol Imaging.* 2010; 37(11):2127-35.
- Wu C, *et al.* Quantitative multi-pinhole small-animal SPECT: uniform versus non-uniform Chang attenuation correction. *Phys Med Biol.* 2011; 56(18):N183-93.
- Xiao K, *et al.* The effect of surface charge on *in vivo* biodistribution of PEG-oligocholeic acid based micellar nanoparticles. *Biomaterials.* 2011; 32(13):3435-46.
- Yamaoka T, *et al.* Distribution and tissue uptake of poly(ethylene glycol) with different

molecular weights after intravenous administration to mice. *J Pharm Sci.* 1994; 83(4):601-606.

Yang Y, *et al.* The biodistribution of self-assembling protein nanoparticles shows they are promising vaccine platforms. *J Nanobiotechnology.* 2013; 11:36.

Ychou M, *et al.* Potential contribution of ¹³¹I-labelled monoclonal anti-CEA antibodies in the treatment of liver metastases from colorectal carcinomas: pretherapeutic study with dose recovery in resected tissues. *Eur J Cancer.* 1993; 29A(8):1105-1111.

Yu K, *et al.* Multiple morphologies in aqueous solutions of aggregates of polystyrene-block-poly(ethylene oxide) diblock copolymers. *Macromolecules.* 1996; 29(19):6359-61.

Zhang Y, *et al.* Effect of size, shape, and surface modification on cytotoxicity of gold nanoparticles to human HEp-2 and Canine MDCK cells. *J Nanomater.* 2012; 2012: 1-7.

Zhou Y, *et al.* Monitoring breast tumor lung metastasis by U-SPECT-II/CT with an Integrin $\alpha(v)\beta(3)$ -targeted radiotracer (99m)Tc-3P-RGD(2). *Theranostics.* 2012; 2(6):577-88.

Zhu J, *et al.* Spontaneous generation of amphiphilic block copolymer micelles with multiple morphologies through interfacial instabilities. *J Am Chem Soc.* 2008; 130(23):7496-502.

Ziessman HA, *et al.* Nuclear Medicine (Fourth Edition). Elsevier Saunders. 2014.

Zuckier LS, *et al.* Evaluation in a mouse model of a thyroid-blocking protocol for ¹³¹I antibody therapy. *Cancer Biother Radiopharm.* 1998; 13(6):457-60.

Zuckier LS, *et al.* Kinetics of Perrhenate Uptake and Comparative Biodistribution of Pertehenate, Pertechnetate, and Iodine by NaI Symporter-Expressing Tissues *In Vivo.* *J Nucl Med.* 2004; 45(3):500-507.

Publications list

Peer-reviewed international journal articles

Ivashchenko O, van der Have F, Villena JL, Groen HC, Ramakers RM, Weinans HH, Beekman FJ. Quarter–millimeter-resolution molecular mouse imaging with U-SPECT⁺. *Mol Imaging*. November 2014.

Ivashchenko O, van der Have F, Goorden MC, Ramakers RM, Beekman FJ. Ultra-high-sensitivity mouse SPECT. *J Nucl Med*. 2015; 56(3):470-475.

Arranja A*, **Ivashchenko O***, Denkova AG, Morawska K, van Vlierberghe S, Dubruel P, Waton G, Beekman FJ, Schosseler F, Mendes E. SPECT/CT imaging of Pluronic nanocarriers with varying PEO block length and aggregation state. *Mol Pharm*. 2016; 13(3):1158-65.

**equal contribution*

Jennings L*, **Ivashchenko O***, Marsman IJC, Laan AC, Denkova AG, Waton G, Beekman FJ, Schosseler F, Mendes E. *In vivo* Biodistribution of stable spherical and filamentous micelles probed by high-sensitivity SPECT. *Biomater Sci*. 2016; 4(8):1201-11.

**equal contribution*

van der Have F, **Ivashchenko O**, Goorden MC, Ramakers RM, Beekman FJ. High-resolution clustered-pinhole ¹³¹Iodine SPECT imaging in mice. *Nucl Med Biol*. 2016; 43(8):506-11.

Conference presentations

Ivashchenko O, van der Have F, Villena JL, Beekman FJ. Quarter-millimeter-resolution preclinical SPECT with quarter-mm pinholes. *EANM Annual Meeting 2013*, 19-23rd October 2013, Lyon, France.

Ivashchenko O, van der Have F, Beekman FJ. Ultra-low-dose mouse SPECT with a focusing conical pinhole collimator. *J Nucl Med annual meeting abstracts*, May 2014, vol 55(1): 492.

Ivashchenko O, van der Have F, Groen HC, Villena JL, Ramakers RM, Weinans HH, Beekman FJ. Quarter-mm molecular bone imaging with a stationary high-resolution SPECT system. *J Nucl Med annual meeting abstracts*, May 2014, vol 55(1): 2141.

van der Have F, **Ivashchenko O**, Groen HC, Ramakers RM, Durring H, Beekman FJ. High-resolution medium-sized animal multi-pinhole SPECT with stationary detectors. *EANM Annual Meeting 2014*, 18-22rd October 2014, Gothenburg, Sweden.

Ivashchenko O, van der Have F, Beekman FJ. Model-based depth-of-interaction compensation for small-animal pinhole SPECT. *J Nucl Med annual meeting abstracts*, May 2015, vol 56(3):44.

Ivashchenko O, Jennigs L, Schosseler F, van der Have F, Beekman FJ, Mendes E. High-sensitivity SPECT as a tool for preclinical evaluation of radiolabeled nanoparticles. *Molecular and Supramolecular Carriers for Imaging and Therapy*, July 2015, Lisbon, Portugal.

Jennings L, **Ivashchenko O**, Laan AC, Waton G, van der Have F, Beekman FJ, Schosseler F, Mendes E. Spherical and elongated micellar carriers as versatile theranostic devices. *23rd International Conference on Bioencapsulation*, September 2015.

van der Have F, **Ivashchenko O**, Goorden MC, Ramakers RM, Beekman FJ. High-resolution Iodine-131 SPECT imaging in Mice. *IEEE Nuclear Science and Medical Imaging Conference*, M3CP-77, 2015.

Curriculum vitae

Oleksandra Volodymyrivna Ivashchenko

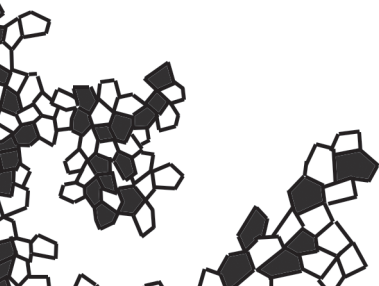
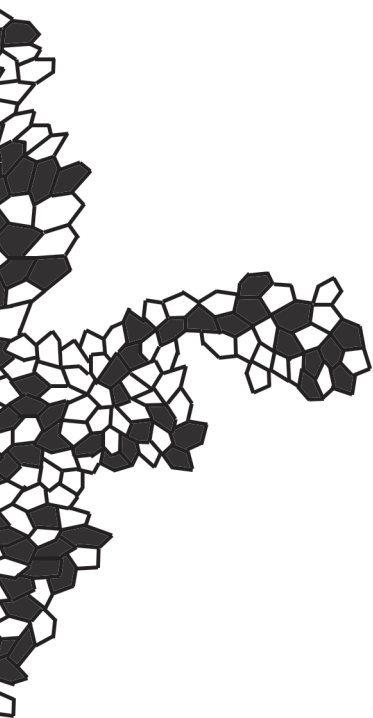
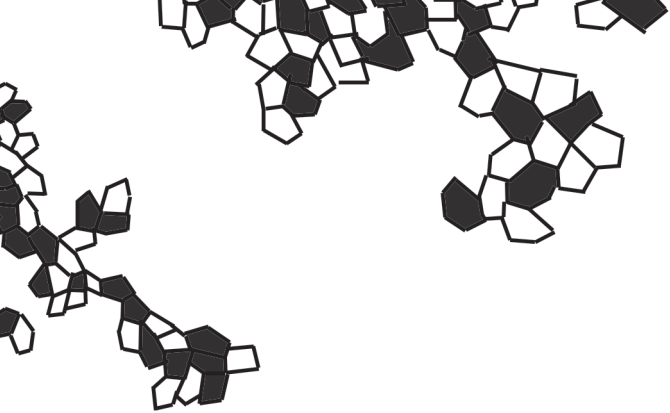
born on January 21st, 1989 in Zolotonosha, Ukrainian SSR

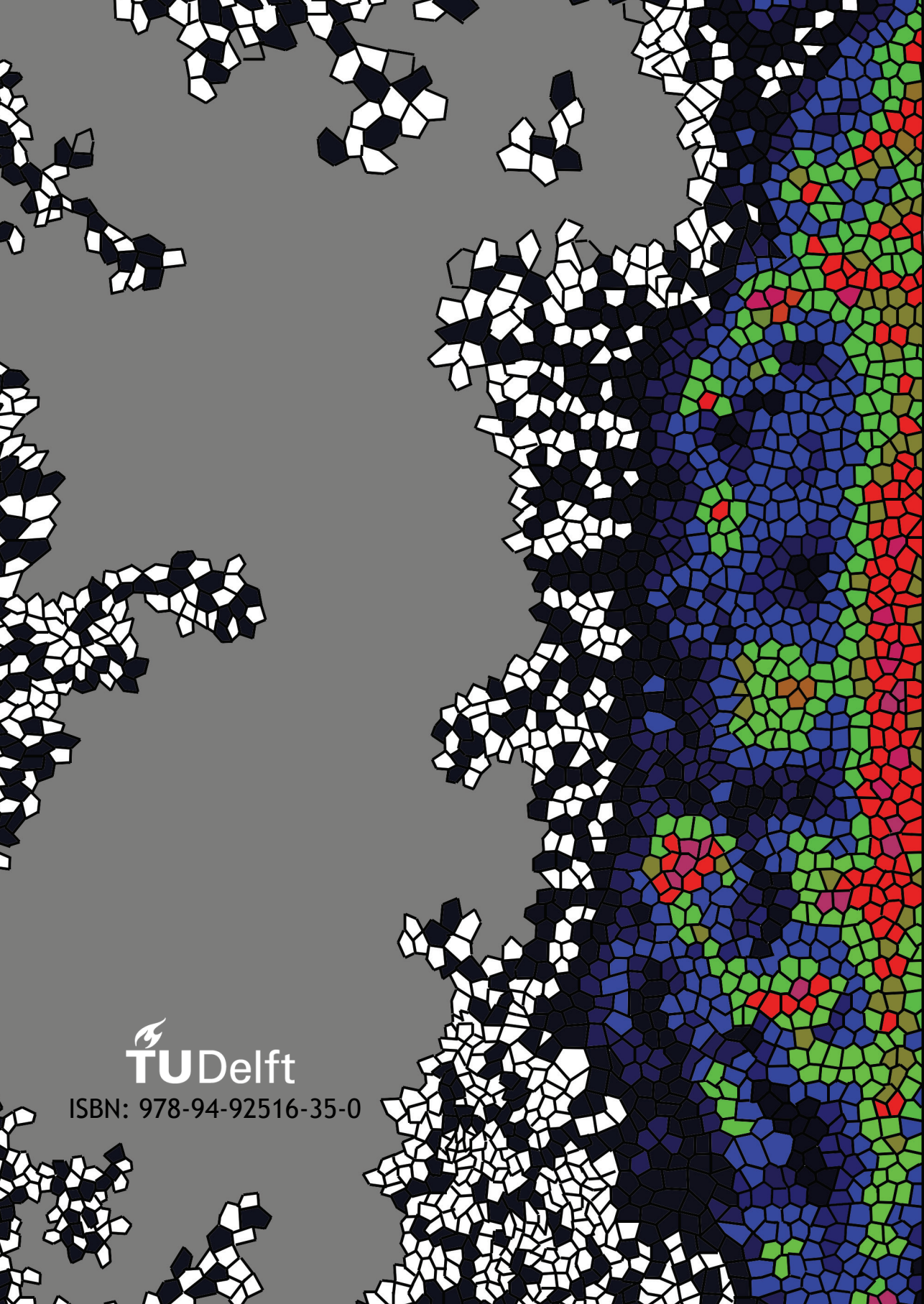
- 2013-2016 Early-Stage Researcher of Marie Curie ITN/PhD in Applied Physics
MILabs B.V./Delft University of Technology, The Netherlands
Thesis title: “Development and applications of high-performance small-animal SPECT”
- May 2015 Visiting Researcher
Johannes Gutenberg Universität Mainz, Germany
- 2011-2013 Medical Engineer
Materialise NV, Ukraine
- 2010-2012 MSc in Radiophysics and Electronics (Cum Laude)
Taras Shevchenko National University of Kyiv, Ukraine
Major: Medical Physics
Graduation project: “Interaction of dynorphins with cellular membrane of neurons”
- 2006-2010 BSc in Applied Physics
Taras Shevchenko National University of Kyiv, Ukraine
Major: Medical Physics
Graduation project: “Non-opioid influence of big dynorphin on cell membrane conductivity”

Подяка

Ця дисертація ніколи не була б неможливою без безмежного терпіння, розуміння та підтримки моїх колег, мого наукового керівника та сім'ї.

Моя щира і безмежна вдячність кожному з вас.





**TU Delft**

ISBN: 978-94-92516-35-0